Development of Lattice Boltzmann CO$_2$ dissolution model

Wei Wei

Submitted for the degree of *Doctor of Philosophy*

Heriot Watt University

School of Engineering and Physical Sciences

May 2014

Abstract

In this study, a novel lattice Boltzmann model (LBM) of CO_2 dissolution at porous scale is proposed and developed to predict the CO_2 dispersion and dissolution in geo-formations. The developed LBM dissolution model consists of an interfacial momentum interaction model, a mass transfer model and a convection (advection) model.

Shen-Chen's pseudopotential model using Equation of State (EOS) of real fluids is tested for momentum interaction model. It is found that a sharp interface can be maintained by optimizing the interaction strengths of two fluids with minimum numerical diffusion in the interfacial momentum interaction model. This makes it possible to model physical diffusion and interfacial tension individually.

A new diffusion force, describing the particle diffusion driving by chemical potential at given solubility, is proposed for mass transfer model by applying the interparticle interaction pseudopotential concept. The dissolution is governed by coupling mechanism of diffusion and convection. The interface between the solute of CO_2 and solvent water is monitored by the solubility, which changes and indicates the moving of interface as CO_2 dissolving. The solution is considered as the mixture of dissolved CO_2 and water. Instead of using an additional Lattice that is requested by the existed LBM, the further dispersion of dissolved solutes is attached to the Lattice of water, by which the cost of computing memory size and time is significantly reduced.

The developed LBM dissolution model is calibrated by the data from Lab experiment of dissolution of CO_2 droplet in water at a state of CO_2 geological storage about 1000m depth. The calibration is made by comparison of simulation results with the data, in terms of the shrinking rate of CO_2 droplet and the concentration distribution of dissolved CO_2 in the solution layer. As the whole, the numerical predictions are well agreement with those of lab experiment.

The developed model is then applied to investigate the mechanism of dispersion and dissolution of CO_2 droplet in channels at pore scale, in terms of the effects of the *Eo* number,

channel width and channel tilt angle. It is found under the state at 1000m depth that it is difficult for a dissolving CO_2 droplet, unlike that of an immiscible droplet, to reach to a 'terminal velocity'. Because of the shrinking, dissolving CO_2 droplets accelerate from a quiescent state to a maximum velocity and then decelerate in the channels. The ratio of droplet diameter (D_o) to channel width (L_x), $M=D_o/L_x$, and the inclination are the parameters that significantly affect the dynamics of dissolving CO_2 droplets. The smaller the channel width or the tilt angle of the pores of the geoformation, the slower of stored CO_2 can penetrate vertically and dissolve out. While, as the channel width increases to provide enough space, $M<1$, the shrinking rate is independent of the channel width and wobbling of droplets is observed at the region with the *Re* number of 300-600 and the *Eo* number of 20-43.

The interactions of droplets in the channels ($M=1$ and $M=0.3$) are investigated by simulating of a pair of droplets dispersion and dissolution, with an initial distance of 4.5 times of droplet diameter. Comparison is made to that of single droplet in terms of the rising velocity and shrinking rate. It is found that the shrinking rate of the upper droplet is larger than that of the following droplet when the following droplet moves into the solution field of the upper droplet. The following droplet rises, when $M=1$ and $M=0.3$, faster than that of the upper droplet and also than that of the single droplet under the same conditions. The coalescence of two droplets is observed in the channel at $M=0.3$, which is due to the action of tail vortex of the upper droplet on the following droplet. The following droplet accelerates at a different wobbling frequency with that of the upper droplet.

As the implication in model development, in term of numerical stability, the so called 'non-linear implicit trapezoidal lattice Boltzmann scheme', proposed by Nourgaliev et al. [1], is re-examined in order to simulate the large density ratio of two-fluid flows. It is found from the re-derivation that the scheme is a linear scheme in nature. Therefore, the re-derived scheme is more efficient and the CPU time can be reduced. The test cases of the simulation of a steady state droplet using SC EOS show that re-derived scheme improves the numerical stability by reducing the spurious velocity about 21.7% and extending the density ratio 53.4% as relaxation time of the improved scheme is 0.25, in comparison to those from the traditional explicit scheme. Meanwhile, in the multicomponent simulation, with the same density distribution at steady state, the improved scheme reduces both the

magnitude and spreading region of the spurious velocity. The spurious velocity of the improved method reduces approximate 4 times than that of the explicit scheme.

Acknowledgements

I offer my first and foremost sincerest gratitude to my supervisor, Dr. Baixin Chen, who had supported me throughout my PhD work with his patience and knowledge over these past years. Thanks to his constructive advice on the project. I attribute the level of my PhD degree to his encouragement and effort.

I also would like to express my great appreciation to my colleague, Marius Dewar, for collaboration in the CO_2 droplet leakage study. I would like to thank another colleague Sorush Khajepor, for his discussion on Lattice Boltzmann modelling. Also thanks to my colleagues, Tariq N. Chaudhary and Onne A. Okpu, for their suggestions and questions during the group meeting.

Finally, I would like to thank my parents Wei Rongsen and Wei Shuqin for there continued encouragement and care. Also, I would like to thank my husband Bin Li, for his support during the most difficult time of thesis writing. Without his love and support, none of this could have happened. In particular, I would like to thank my loverly daughter, Audery Tianyao Li, for her sweet smile and understanding. Her arrival offered me courage to finish my thesis. I want to thank to my soon to be born baby, for accompanying me to finish the thesis.

Contents

CONTENTS

Figures and Tables

Figures

FIGURES AND TABLES

FIGURES AND TABLES

Tables

Nomenclature

BGK   Bhatnagar-Gross-Krook

CCS   carbon dioxide capture and storage

CLR CO_2 leakage risk

EOR   enhanced oil recovery

EOS   equation of state

LB   lattice Boltzmann

LBM   lattice Boltzmann method

LGA   lattice gas automata

MPMC multiple phase multiple component

PR   Peng and Robinson

SC   Shan-Chen pseudopotential model

TRT   two relaxation time

Bo   Bond number

Ca   Capillary number

Da   Damk*ö*hler number

Eo   E*ö* tv*ö*s number

Gr   Gravity number

Mo   Morton number

Pe   P*é*clet number

Ra   Rayleigh number

Re   Reynolds number

Sh   Sherwood number

St   Stefan number

C   solute concentration

C_s saturated concentration/solubility

FIGURES AND TABLES

D_f diffusivity

D_o initial droplet diameter

F external force

F^f interparticle interaction force

F^g gravity force

F^d diffusion force

$G_{\sigma\bar{\sigma}}$ interaction strength between σ and $\bar{\sigma}$ fluid

G_{ads} interaction strength between solid and fluid

G_d diffusion potential strength

L characteristic length

L_x channel width

M diameter ratio D_o/L_x

P_C capillary pressure

ΔP pressure difference

S_w the normalized water saturation

T temperature

U characteristic velocity

c_s speed of sound for perfect gas

e_i velocity vector on i direction

f distribution function

f^{eq} equilibrium distribution function

g gravitational acceleration

t time

u velocity

w_i weight of the numerical integration on i direction

κ_{ri} relative permeability

κ_i permeability of phase i

κ absolute permeability of the porous media with a single phase

μ dynamic viscosity

υ kinetic viscosity

ϕ porosity

FIGURES AND TABLES

$\psi(\rho)$ interaction potential as a function of density

ρ density

σ surface tension

τ relaxation time

τ^I relaxation time of implicit scheme

τ^E relaxation time of explicit scheme

θ angle

$\psi(\rho)$ interaction potential as a function of density

ρ density

List of Publications

Marius Dewar, Wei Wei, David McNeil, Baixin Chen. Small-scale modelling of the physiochemical impacts of CO_2 leaked from sub-seabed reservoirs or pipelines within the North Sea and surrounding waters. *Marine Pollution Bulletin*, August 30, 2013

Marius Dewar, Wei Wei, David McNeil, Baixin Chen. Simulation of the Near Field Physiochemical Impact of CO_2 Leakage into Shallow Water in the North Sea, *Energy Procedia*, 37: 3413-3423, 2013

Chapter 1

Introduction

1.1 Perspective

Global warming is widely regarded as a serious environmental issue to be addressed. The average Earth surface temperature correlates well with the amount of CO_2 in the atmosphere. Until a clean and abundant source of energy is developed, a solution must be found to mitigate the effects of such emissions.

Carbon Dioxide Capture and Storage (CCS) has been widely accepted as one of means to mitigate global warming. With regard to the potential biological impact of direct injection into the ocean, carbon dioxide geological storage is considered to be more suitable in an engineering scale. The main risk of CO_2 geological storage is leakage. A series of field observation, laboratory experiments and numerical simulations in different spatial and temporal scales have been undertaken to predict the possibilities of leakage and assess their risk. The conclusions from the studies indicated that it is essential to understand the full physical and chemical mechanisms of interactions between fluids (brine, CO_2, natural gas, and oil) and the interactions between fluids and geoformations.

In order to investigate the mechanisms of CO_2 geological storage, the mechanism at pore scale will provide the fundamental knowledge for prediction model developments. One of the mechanism models to be developed is the CO_2 mass transfer model. The Lattice Boltzmann method (LBM), as an effective algorithm with which to simulate the single phase or multiple phase/component fluid flows in complex geometries, is applied in the development of the novel Lattice Boltzmann multicomponent multiphase mass transfer model at pore scale.

From the literature reviews of the existing Lattice Boltzmann mass transfer models, it has

been recognized that none of the existing models have been found to be suitable to describe the CO_2 dissolution in water. Therefore, construction of a novel Lattice Boltzmann multicomponent multiphase CO_2 dissolution model is necessary.

1.2 Research Hypothesis

A LBM CO_2 dissolution model at porous scale can be constructed by joining an interfacial momentum interaction model, a mass transfer model and a convection (advection) model. The interfacial momentum interaction model is based on Shan-Chen's pseudopotential model incorporated with an Equation of state of real fluid. The mass transfer of CO_2 into water is due to CO_2 dissolution, which is governed by the coupling mechanisms of diffusion and convection. The CO_2 diffusion, driven by the gradient of the chemical potential, is described by the interparticle interaction pseudopotential. Once the CO_2 is dissolved into water, the solution is considered as a mixture of dissolved CO_2 and water. The further dispersion of dissolved CO_2 solutes is attached to the Lattice of water. For such a proposed model, no additional Lattice is required for the CO_2 solution; consequently, the cost will be reduced regarding both the memory and CPU time.

1.3 Research Objectives

The objectives of this research are, in LBM theory, to challenge simulation of the mass transfer by adopting pseudopotential concepts for a LB mass transfer model. In practice, this would address the lack of appropriate LBM CO_2 dissolution model at pore scale based on the mechanism and physical model of CO_2 dissolution in water.

The availability of the developed model should be tested or calibrated by the published lab experiment data at CO_2 geological storage condition, in terms of the shrinking rate of the droplet and the concentration distribution of the dissolved CO_2. The effects of numerical diffusion on the dissolution, taking into account the system of static CO_2 droplet in water, must be examined in order to identify the schemes which distinguish it from physical diffusion.

To investigate the characteristics of CO_2 dispersion and dissolution in pores, a set of pore-scale channels with variance of sizes and tilt angles was used; these are assumed to be the geo-units of formation, and are regarded as an artificial geoformation for storage of CO_2. The shrinking rate, rising velocity, and deformation of CO_2 droplet are the key parameters used to describe the CO_2 dynamics in the artificial geoformation. They are to be predicted by simulations using model developed in this study.

In order to identify the role of droplet interaction, simulations of the dissolution of multiple droplets is designed using the developed model to enable comparison with that of a single droplet in the channels. The mechanisms of the break-up of a droplet and coalescence of two droplets are to be studied.

With regard to the numerical stability of the LBM model, one of the objectives of the study is to improve the LBM scheme. The 'non-linear implicit trapezoidal lattice Boltzmann method' proposed by Nourgaliev et al. [1] is to be re-examined and a simple linear scheme will be derived from it. The aim of the improved model is to preserve the trapezoidal rule central approximation and to avoid the iteration calculation. The improved model is to be tested by simulation of multiple phases and multiple components in terms of high density ratios and spurious velocity comparison.

1.4   Contributions to the development of Lattice Boltzmann method

The main contributions of this study to the development of Lattice Boltzmann method include:

1). A novel multicomponent Lattice Boltzmann dissolution model for simulating mass transfer at pore scale is developed, which can be used to study the mechanism of CO_2 dissolution and dispersion in geo-formation.

2). A diffusion force driven by the chemical potential is proposed in LBM mass transfer model. The physical diffusion is separated from the interfacial tension. The relationship

between diffusion potential strength in LBM dissolution model and physical diffusivity is obtained .

3). The mechanisms of CO_2 dissolution and dispersion in geoformation are investigated, in terms of the pore structure, and the interaction of CO_2 droplets in a pore-scale channel.

4). A linear LBM numerical scheme is derived from no linear implicit trapezoidal LBM scheme and applied in simulations of multiple fluid flow.

1.5   Organization of the Dissertations

This dissertation is organized into seven chapters. The literature review of carbon capture and storage is described in Chapter 2, including the briefly description of global warming and CCS, the experimental investigations and numerical simulations of CO_2 geological storage. In Chapter 3, the evolution and the governing equation of LBM are introduced, along with the reviews of LBM multicomponent multiphase models and mass transfer models. The challenges of LBM are reviewed and discussed. In Chapter 4, a new LBM multicomponent mass transfer model is developed and calibrated by the lab experiment of static droplet dissolution with natural convections. In Chapter 5, the developed model is applied to investigate the mechanisms of dispersion and dissolution of CO_2 droplet in channels with different sizes and tilt angles at pore scale under CO_2 geological storage state. In Chapter 6, the examination on an implicit LBM numerical scheme and the details of the derivation of a linear LBM scheme are provided with test and validation examples. Finally, Chapter 7 is the summarization of the main conclusions from this study and the suggestions for the future research.

Chapter 2

Background

2.1 Introduction

Carbon geological storage, which has been considered as a potential option to mitigate the emission of carbon dioxide in the atmosphere, is outlined and discussed in this chapter. Firstly, the background related to carbon geological storage is presented in Section 2.2. The technologies of carbon dioxide geological sequestration are summarized in Section 2.3, which is followed by a review of the experimental mechanisms studies of carbon geological storage in Section 2.4, in terms of the experiment studies in the field and in the laboratory. In Section 2.5, the studies of numerical simulation of carbon geological storage are reviewed and discussed in terms of modelling and modelling applications in different spatial scales. Finally, Section 2.6 summarizes the studies of carbon geological storage and highlights the objectives of the dissertation.

2.2 Global warming and CCS

Global warming is regarded as a serious environmental problem which human beings have to face today. It has been estimated that global warming could produce a number of effects, including rising sea levels, extinction of various species, and expansion of deserts [24].

The average temperature of the Earths' near-surface air and oceans has been increasing continuously since the mid-twentieth century. For example, the earth surface temperature increased by $0.74\pm0.18\,^{\circ}$C during the last century, based on surface air measurement at meteorological stations and satellite measurements of sea surface temperature [25], as
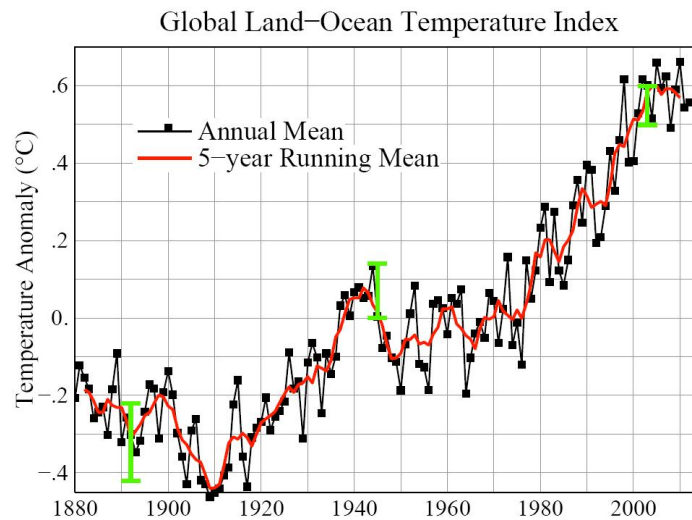
Figure 2.1: Global annual mean temperature changes with time from surface air measurement at meteorological stations and satellite measurements of sea surface temperature, which is relative to the mean temperature $(0.54\,^{\circ}\text{C})$ during 1951-1980 [2].

shown in Figure 2.1. The linear warming rate between 1950 and 2000 of $0.13\,^{\circ}\text{C}$ per decade is nearly twice the rate observed from 1900 to 1950. Consequently, the global average sea level rose approximately 1.8 mm per year from 1961 to 2003; it should be noted that the rate increased to 3.1 mm per year from 1993 to 2003 [25].

According to the Intergovernmental Panel on Climate Change (IPCC), anthropogenic greenhouse gases are responsible for the most of the observed temperature increase through the use of the fossil fuels oil, natural gas, coal and land clearance [25]. Model experiments suggest that further warming will continue at a rate of approximately $0.1\,^{\circ}\text{C}$ per decade, even if the concentration of greenhouse gases were kept at the level found in the year 2000 level [25].

The main greenhouse gases include water vapor, carbon dioxide (CO_2), methane (CH_4) and nitrous oxide (N_2O) [25]. With the exception of water vapor, carbon dioxide as part of greenhouse gases contributes most to the greenhouse effect, contributing 9-26% [26].

The observation results appear to confirm this, showing that the concentration of carbon dioxide in the atmosphere correlates with the variations in Earth surface temperature since 400000 years before 2007 [4], as shown in Figure 2.2. It should be noted that the concentration of carbon dioxide significantly increased in the past thirty years at the rate

2.2. Global warming and CCS
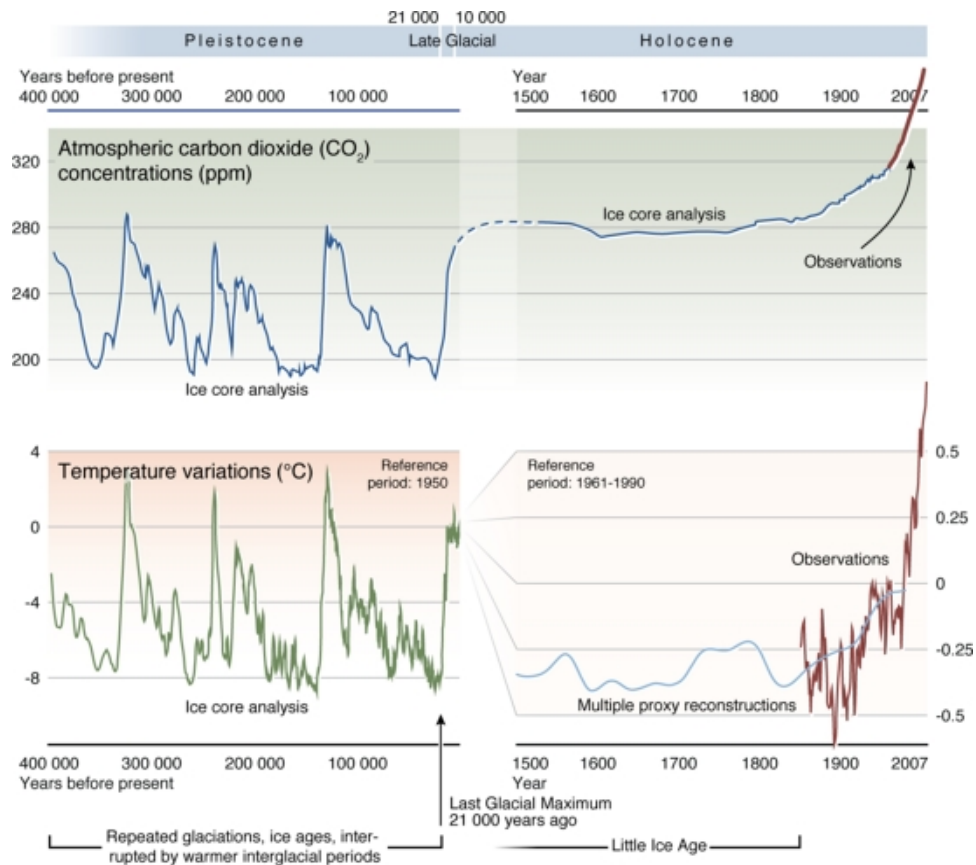
Figure 2.2: Historical trends in the change of carbon dioxide concentration and temperature [3].

of approximately 1.6 ppm per year, as shown in the observation data at the right side of Figure 2.2 (the enlarged part). Meanwhile, the observed temperature has risen rapidly during the same period. In 2013, the earth system research laboratory reported that the concentration of carbon dioxide in the atmosphere had increased to 395.09 ppm in January 2013, which is approximately 0.4 times more than that of the pre-Industrial Revolution in the 1800s, which was 280ppm [27]. The total CO_2 emissions from industrial activities worldwide are approximately 13,466 million tonnes per year, of which 10,539 million tonnes per year are emissions from power plants [4]. The consumption of fossil energy sources is a primary factor (>80%) related to the increase of CO_2 concentration [25].

In order to restrict the concentration of carbon dioxide below 500ppm, the EU countries planned to reduce the greenhouse gas emissions by 30% in 2020 and by 50% in 2050, in comparison with the figure in 1990 [28]. However, the latest data from the U.S. Energy Information Administration (IEA) indicates that global energy-related CO_2 emissions in

2.2. Global warming and CCS
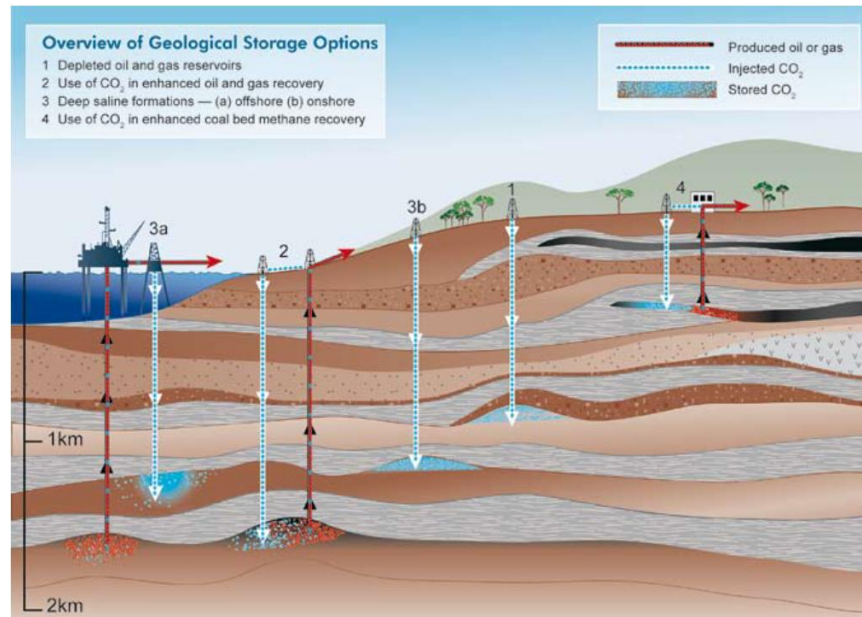
Figure 2.3: Overview of CO_2 geological storage [4]

2013 are 2% higher than the 2012 level.

Faced with such a challenge, several mitigation technologies have been proposed to minimize carbon dioxide emissions, such as improvements in energy efficiency, increasing the use of renewable energies, switching to nuclear energy, biological sinking and carbon capture and storage [29].

Energy Efficiency Improvement consists of a series of technologies used to improve energy efficiency in industry. World Energy Council (WEC) investigated the potential of Energy Efficiency Improvement in a series of scenarios. The studies assume that the equipment is replaced by the current most efficient technologies; the industrial energy requirement is 173 EJ in 2020 and the energy efficient technologies are applied in all major countries. Finally, the studies suggest that the use of Energy Efficiency Improvement technology can successfully reduce the industrial energy consumption about 70EJ per year, in comparison with that using the baseline technology, which is equivalent to approximately 1100 MtC per year [30].

Renewable energy is derived from the intermittent sources such as wind, solar, tidal, wave, biofuels and geothermal heat energy [30]. In recent years, the development of renewable energy has increased rapidly [31]. In 2008, renewable energy supplied 12.9% of the total global primary energy, including Biomass 10.2%, Solar energy 0.1%, ocean energy

2.2. Global warming and CCS

Figure 2.4: Carbon Dioxide Capture and Storage worldwide projects. Yellow Mark: Power Plant CCS projects; Blue Mark: Pilot CCS projects; Red Mark: Commercial EOR projects; Green Mark: Non-Power CCS projects; White Mark: Canceled or Dormant CCS projects

0.002%, wind energy 0.2%, hydropower 2.3% and geothermal energy 0.1% [31]. From 2008 to 2009, the global electricity generating capacity increased by approximately 300 GW; renewable energy contributed 46.67%. However, most of these renewable sources are restricted by the intermittent sources, cost, and environmental impacts [30].

Nuclear energy is one of the non-carbon energy sources which use exothermic nuclear processes to generate electricity and heat [30]. Nuclear energy capacity increased significantly from 1 GW in 1960 to 300 GW in the 1980s. After that, the increase in nuclear energy capacity has been slow as most of the nuclear projects were cancelled. This change occurred at the time of the Chernobyl disaster in 1986, regarded as the worst nuclear power plant accident in history [32]. In 2012, nuclear energy contributed 5.7% of the total global primary energy and 13% of the global electricity [33]. Due to operation safety and waste issues, nuclear energy expansion is restricted [34] [35].

Biological sinks are natural sinks that store CO_2 from the atmosphere for an uncertain period by plants, ocean and soils through the global carbon cycle [36]. A large quantity of CO_2 has been stored by biological sinks. The amount of carbon stored in the ocean by biological sink is approximately 20 times the amount of carbon in soils and plants [4]. From 1980 to 2000, the average amount of CO_2 sunk into the ocean from the atmosphere was 7 Gt CO_2 per year [37]. However, the sinking rate of biological sinks is slow and cannot meet the need to mitigate CO_2 at a level of 500 ppm in 2100 [38]. As shown in case

2.2. Global warming and CCS
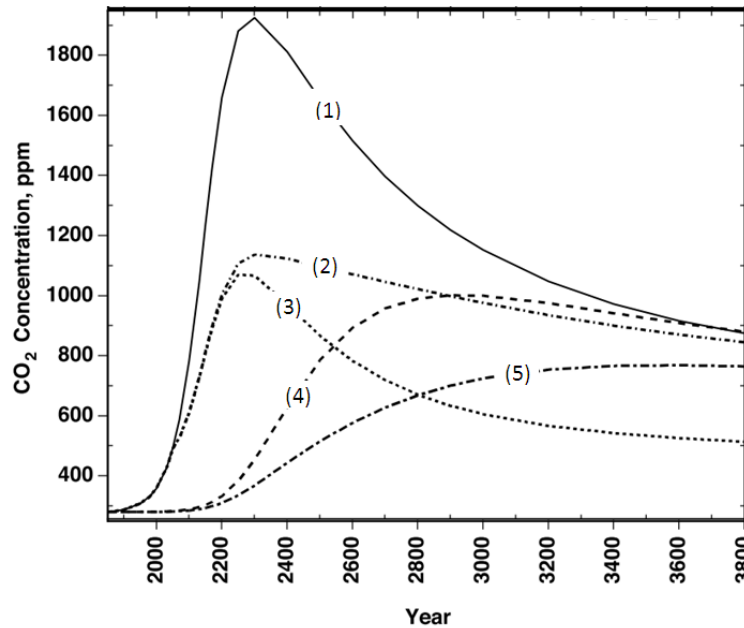
Figure 2.5: The simulation results of the atmospheric CO_2 concentration varying with time in five cases with cumulative emissions of 18,000 $GtCO_2$. (1)100% release to the atmosphere; (2)after 2050, 50% emissions to atmosphere and 50% injected to ocean; (3)after 2050, 50% emissions to atmosphere and 50% by other permanent sequestration method; (4)100% injected into Pacific; (5)100% injected into atlantic [5].

(1) of Figure 2.5, the simulation results using a nonlinear convolution model indicated that if 100% of CO_2 emissions are released into the atmosphere and sunk by means of global carbon cycle, the CO_2 concentration will reach a peak of 1925 ppm by the year 2300. Moreover, it takes approximately 1000 years to decrease to less than 1000 ppm. When the global carbon cycle is combined with the ocean injection or the permanent sequestration method, as shown in case (2) and (3) of Figure 2.5, the peak in CO_2 concentration will reduce to approximately 1100 ppm. Finally, The results of case (4) and (5) show that when CO_2 is injected into the Atlantic and the Pacific, respectively, the CO_2 concentration will not be over 1000 ppm and 800 ppm, respectively. Thus, use of the biological sink is insufficient to reduce atmospheric CO_2 concentration. The permanent sequestration method is a more effective method of reducing the atmospheric CO_2 concentration.

Carbon dioxide Capture and Storage (CCS), as a CO_2 mitigation option, has the potential to enable continuing use of fossil fuels. Model studies show that CCS could reduce the mitigation cost and would increase flexibility in reducing CO_2 emissions, in comparison with other mitigation technologies [4]. Up to the end of 2013, 57 CCS projects had been

undertaken worldwide such as the Sleipner gas project in Norway, enhanced oil recovery in Canada and USA and enhanced recovery of coal bed methane in Canada and New Mexico [39]. The project distribution is shown in Figure 2.4.

Coal is still the primary fuel used to generate electricity. In 2000, 38% of electricity globally was generated by coal, 17.5% by hydro power, 17.3% by natural gas, 16.8% by nuclear, 9% by oil and 1.6% by non-hydro renewable energy. Coal is projected to be the dominant fuel in 2020 [4]. Thus, one aspect of the competitiveness of CCS is that it achieves the continued use of coal as fuel. Another aspect is that CCS is compatible with most energy infrastructures [4]. MiniCAM model studies, in other words an alternative integrated assessment model of CO_2 mitigation analysis, indicate that the CCS contribution to CO_2 emissions reduction will increase to 32.6% in 2095. The contributions of CO_2 emissions reduction by coal to gas substitution, Renewable Energy, Nuclear and Conservation and Energy Efficiency technologies will be 23.9%, 13.04%, 8.7%, and 21.7% respectively, in 2095 [4].

2.3 Carbon Capture and Storage

In general, CCS is a technology designed to perform in three stages, including capture, transport and storage. It performs by directly capturing CO_2 from CO_2 emission sources, such as electricity generation from burning fossil fuels; it sequentially transports the captured and compressed CO_2 via pipelines to the storage site and finally permanently stores the captured CO_2 in suitable sites, such as old oil fields, gas fields, deep saline formations or unmineable coal beds as shown in Figure 2.3 for long-term storage, which were occupied originally by saline water or oil/gases. Injected CO_2 will either replace the original formation fluids or be dissolved into them.

The captured CO_2 is separated from the gas steam; finally the concentrated CO_2 obtained at high pressure can be transported to the storage sites [4]. Based on the process, three basic systems are used in capturing CO_2. Post-combustion capture systems capture CO_2 from the flue gases produced by the combustion. The concentration of CO_2 is about 3-15% by volume in the flue gas. CO_2 can be captured by the liquid solvent. Oxy-fuel combustion

capture systems use oxygen for combustion to produce the flue gas, which is composed only of water vapour and CO_2. The concentration of CO_2 is more than 80% by volume in the flue gas; CO_2 can be separated by cooling. Pre-combustion capture systems separate CO_2 before combustion by causing fuel to react with air or oxygen to produce a "synthesis gas" consisting of carbon monoxide and hydrogen. The carbon monoxide reacts with steam in the shift converter to obtain CO_2 and hydrogen. The concentration of CO_2 is approximately 15-60% by volume. Finally, the CO_2 is separated by means of chemical or physical absorption [4]. All of these systems require the CO_2 separation technologies by the means of sorbents, separation with membranes and refrigerated separation [4]. Those capture techniques were developed 60 years ago; the challenge of successful application to engineering scale is the reduction of costs [4].

The captured CO_2 is transported by tanks, pipelines and ships to the storage sites in supercritical, liquid and even solid states. The pipelines which have been used for oil and natural gas transport are not new [4]. With regard to safe operation, corrosion resistant pipelines are desirable [4].

The geological formations for CO_2 storage need to have sufficient porosity to satisfy the storage capacity, with permeability required by injection and with a low-permeability barrier or cap-rock to avoid the CO_2 leakage. There are three main geological formation options in which to store the CO_2. These are active and depleted hydrocarbons reservoirs, namely oil or gas reservoirs; deep saline aquifers and the unmineable coal beds. The worldwide capacities of these three options are estimated to be 100-1000 Gt, 100-10,000 Gt and 10-1000 Gt, respectively [4]. CO_2 has been injected into active and depleted hydrocarbons reservoirs to enhance oil or gas recovery in the petroleum industry; this is a mature technology [4]. A deep saline aquifer is an underground rock formation, which is composed of saline fluids and permeable materials [4]. In comparison with the other two options, the deep saline aquifer has the largest potential capacity [6]. Injection of CO_2 into the unmineable coal beds has been developed to enhance coal bed methane recovery [40]. CO_2 can be absorbed by the coal in the pore formation [40].

Carbon dioxide can be stored in the geo-formation by relying on various trapping mechanisms related to its properties at various pressures and temperature conditions. The critical

2.3. Carbon Capture and Storage
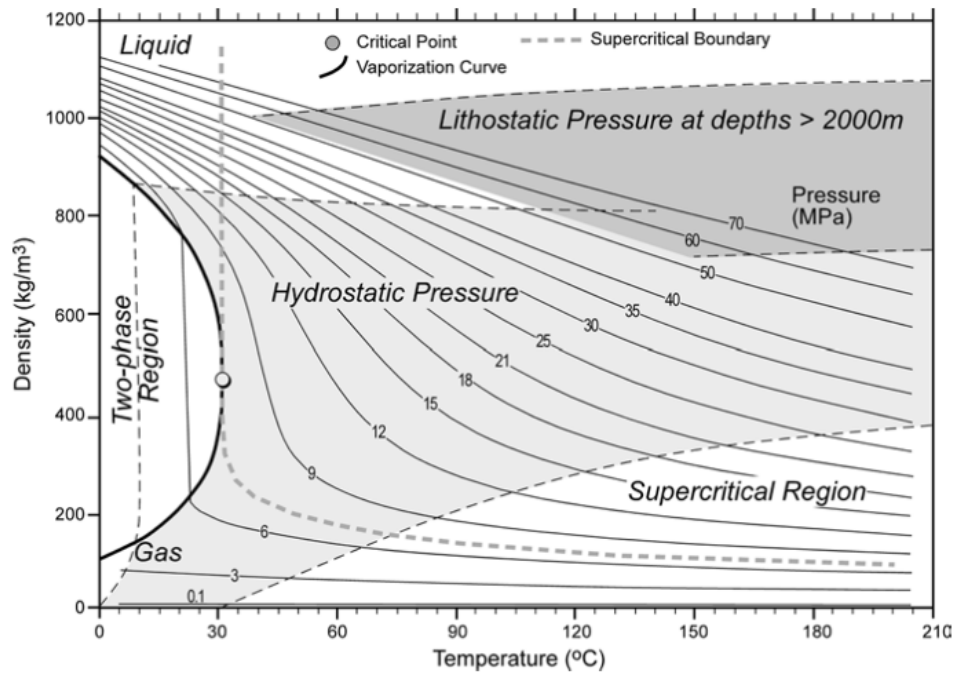
Figure 2.6: Carbon Dioxide density varies with pressure and temperature [6].

point of CO_2 is T_c=304 K and P_c=7.38 MPa. When both the temperature and pressure are at or above the critical point, the CO_2 is in a supercritical state. In the supercritical condition, CO_2 behaves like a gas that can expand to fill the container, and a liquid with a large density. The brine density depends on the salinity, temperature and pressure, which is in the range of 1020-1050 kg/m^3. CO_2 is generally stored in a supercritical state in reservoirs or deep saline at depths below 800 m [4]. The supercritical CO_2 is lighter than the brine, and the buoyancy force then becomes dominant to drive the CO_2 upwards. As shown in Figure 2.6, only in the case of lithostatic pressure conditions in which the depth is greater than 2000 m, CO_2 density is larger than that of the water [6].

When CO_2 is injected in the storage sites, the fraction and retained CO_2 depend on the primary and secondary trapping mechanisms. The primary trapping, is hydrodynamic and stratigraphic or structural trapping beneath seals of low permeability rocks, known as cap rock, in oil or gas reservoirs and absorption in coal beds, which occurs immediately after injection to prevent leakage near the surface zone. In the coal beds, the gaseous CO_2 can be adsorbed, as coal contains a number of micropores [4]. For example, Tiffany coal can absorb 16 m^3/tonne CO_2 at 55°C and 140 bar [41]. In the storage sites of oil or gas reservoirs, the permeability and thickness of the rock above the storage formation

2.3. Carbon Capture and Storage
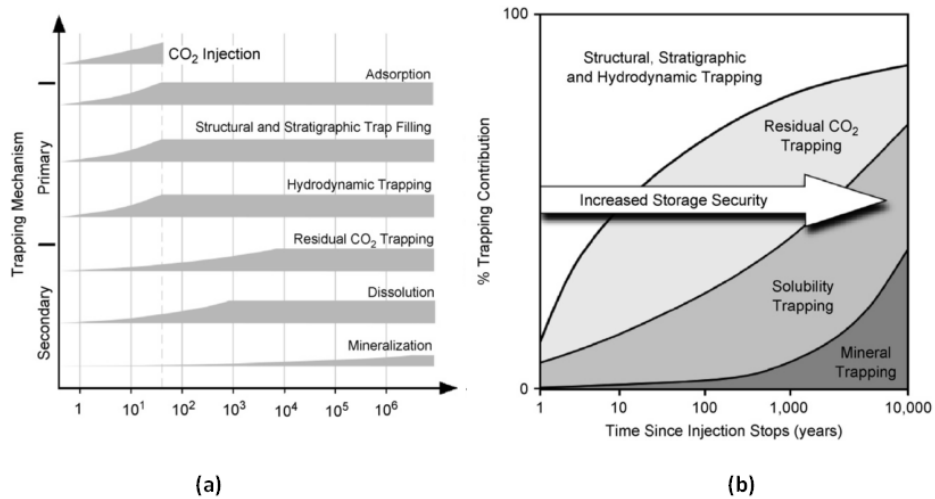
Figure 2.7: The comparison between various trapping mechanisms (a)timeframe for operating; (b)contribution for storage security [6].

are regarded as the important characteristics regarding selection of suitable reservoirs for CO_2 storage. The permeability for single fluid, is defined by its ability to allow fluid to pass through porous material, as a factor in Darcy's law

$$\kappa = v\frac{\mu \Delta x}{\Delta P} \tag{2.1}$$

where v is the fluid flow velocity through the material (m/s), κ is the permeability of the material (m^2), μ is the dynamic viscosity of the fluid (Pa·s), ΔP is the pressure difference (Pa), and Δx is the thickness of the porous material (m). Darcy's law is only suitable for steady and slow viscous flow. A low-permeability layer, such as shale, acts as a the barrier to prevent the upward migration of CO_2 and causes lateral migration [42].

The secondary trapping, known as geochemical trapping, occurs when the narrow pore spaces in reservoir rock restrict CO_2 mitigation to the surface. Geochemical trapping, which consists of residual or capillary trapping, solubility trapping and mineralization, is a much slower process than the primary trapping; however, it takes place over a longer operating timeframe (Figure 2.7(a)) and makes an important contribution to the long-term storage of carbon dioxide (Figure 2.7(b)) [43].

Residual trapping retains CO_2 in pore spaces in the form of disconnected blobs by capillary force. This occurs as a result of intermolecular forces between liquid and solid

2.3. Carbon Capture and Storage
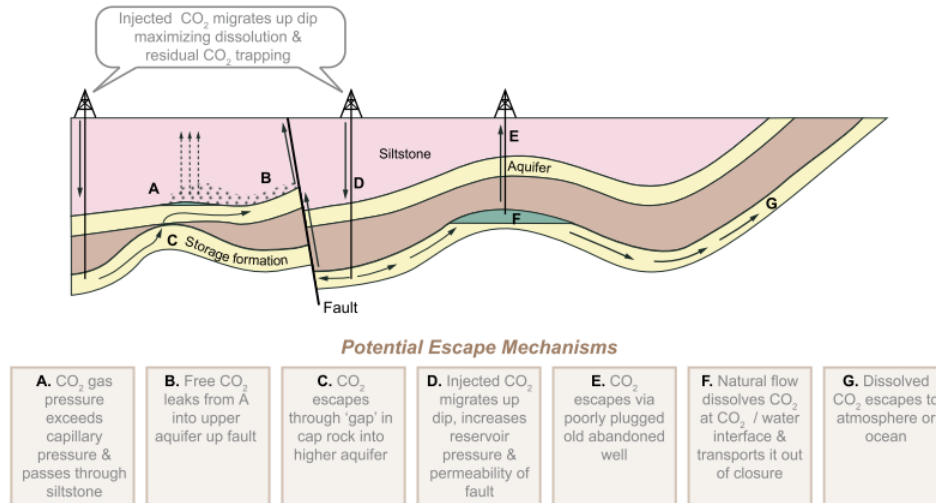
Figure 2.8: Potential CO_2 leakage pathway [4] .

surfaces in small pores, reacting against gravity [44] [45] [46]. This trapping begins after injection has ceased and is important for a storage site without closure [44]. It has been suggested that capillary trapping can immobilize almost all of the injected CO_2 [45] [47].

Solubility trapping occurs as CO_2 dissolves in formation water due to the chemical reaction ($CO_2(g) + H_2O \leftrightarrow H_2CO_3 \leftrightarrow HCO_3^- + H^+ \leftrightarrow CO_3^{2-} + 2H^+$), which results in the decrease of the PH of geo-fluid. Once the CO2 is dissolved in brine, less CO2 migrates upwards, since the density of the CO2 solution is greater than that of the brine.

Mineral trapping occurs as dissolved CO_2 reacts with reservoir minerals ($H^+ + CaCO_3 \Leftrightarrow Ca^{2+} + HCO_3^-$ and $2H^+ + MgCa(CO_3)_2 \Leftrightarrow Mg^{2+} + Ca^{2+} + 2HCO_3^-$) to produce bicarbonate ions (HCO_3^-). Finally, a carbonate mineral is formed by the reaction of the bicarbonate ions with calcium, magnesium and iron over millions of years [48].

Although the trapping mechanisms contribute to storage security, there are still some risks of CCS. The main risk of CO_2 geological storage is leakage, which is also the major concern regarding application of CCS in engineering scales. There are a number of potential pathways for CO_2 migration, which may result in the leakage of CO_2 to the surface. They include poorly plugged wells, caprock seal failure, fractures, or CO_2 injection well, as shown in Figure 2.8. Poorly plugged old abandoned wells have been recognized as the most probable leakage pathways [47]. Apart from that, natural seepage has also occurred in the past few decades [49]. For example, in Poggio dell'Ulivo, central

Italy, CO$_2$ is emitted from vents of CO$_2$ rich groundwater in quantities ranging from less than 100 to more than 430 tCO$_2$/day, which have resulted in the asphyxiation of animal and plants [4]. In Mammoth Mountain, California, USA, high CO$_2$ flux, induced by a resurgence of volcanic activity, leads to ecosystem damage [4]. A high concentration of CO$_2$ generated by a total in the affected areas of approximately 530 t/day in 1996 killed the trees in that location [50] [51]. Thus, natural CO$_2$ seepage in volcanic regions provides examples of CO$_2$ leakage from the storage sites, although natural seepages are not conclusive evidence that leakages would occur from CO$_2$ storage sites in sedimentary basins.

From the above discussion of the trapping and leakage of CO$_2$ in storage sites, it is clear that understanding the mechanisms of interaction of CO$_2$/brine and geoformation is obviously important and necessary in order to reduce assessment uncertainties and to enable assessment the associated risks. In principle, the dynamics of interaction in CO$_2$ geological storage can be described by theories of multi-component fluid flow with mass and energy transfer in a porous media, in other words geoformation. The details of the study will be discussed in the next section.

In order to assess the risk of CO$_2$ geological storage, field observation, laboratory experiments and simulations in different spatial and temporal scales are required. These are reviewed in the following sections.

2.4 Reviews of the experimental investigation of CO$_2$ geological storage

Several options are available regarding storage of CO$_2$, including geological storage, ocean storage and mineral carbonates storage. Due to serious concerns and uncertainties regarding the potential biological impact of direct injection into the ocean, geological storage is currently considered as the most widely available sequestration sites and has been undertaken worldwide.

Carbon dioxide geological sequestration was first proposed in the 1970s and a boom in development were seen until the 1990s because of worldwide research in terms of

2.4. Reviews of the experimental investigation of CO_2 geological storage
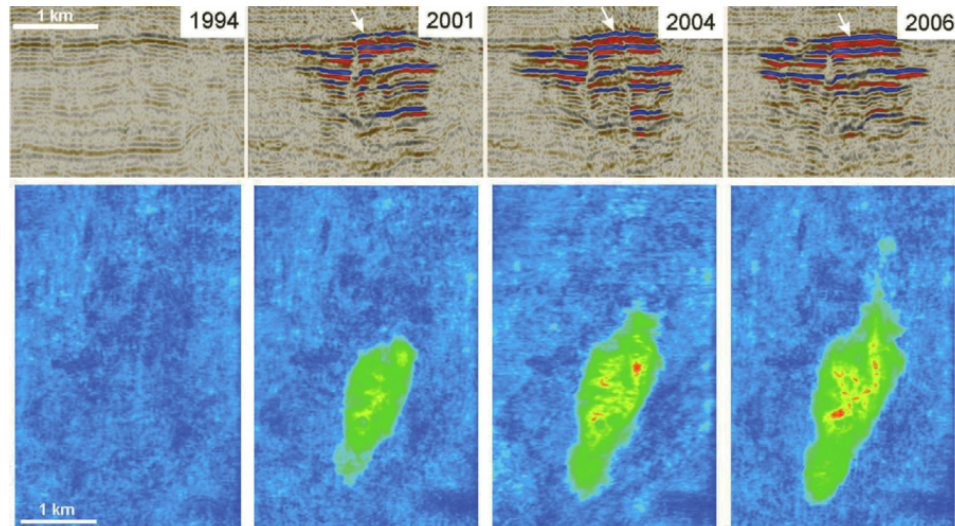
Figure 2.9: Seismic results of CO_2 plume at Sleipner from 1994 to 2006. Top layer shows the vertical seismic sections. Bottom layer shows the development of CO_2 plume by the horizontal seismic sections [7]

investigation of the mechanisms and other industrial projects [52] [53] [54] [55] [56] [57]. The geological sites can be deep saline aquifers, coal beds, and depleted oil or gas reservoirs [58] [55] [59] [60] [61]. In order to investigate CO_2 fluid flow in reservoirs, a number of studies have been carried out both in the field and in the laboratory scales, involving the field observation, laboratory experiments, theoretical studies and numerical simulation.

In the field scale, several projects of CO_2 geological storage have been undertaken worldwide [4]. The major objectives of these projects are to demonstrate and to monitor the migration of the injected CO_2 [62]. Currently, at least three field experimental projects have been designed and carried out for CCS; these are the Sleipner [7], In Salah [63] and Weyburn [64] Projects.

The first commercial scale geological storage project has been operated at Sleipner in the North Sea since 1996. Storage is achieved by injecting 1.0Mt/yr CO_2 into an underground saline aquifer at a depth of 800 m below the seabed. The migration of injected CO_2 has been successfully monitored by 3D time-lapse seismic surveys as shown in Figure 2.9. The CO_2 plume horizontal extent had reached 3.6 km by 2006 [7]. It can be confirmed from those long-term monitored images of the CO_2 plume that: (1) As shown in Figure 2.9(a), in the vertical cross-section, the migration of the plume goes upward and spreads
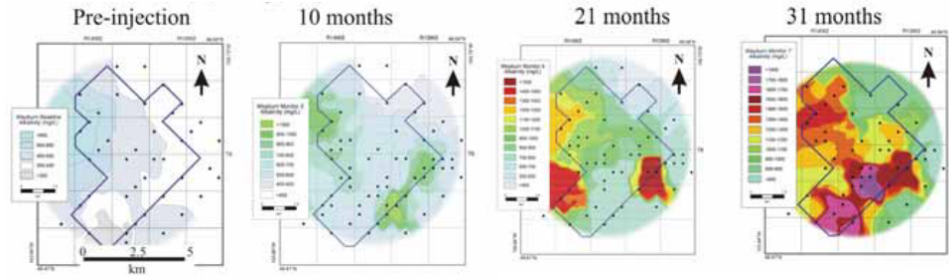
Figure 2.10: $\delta^{13}C_{HCO_3^-}$ in produced fluids at each stage in Weyburn field project. The black dots are the location of the sample wells [8].
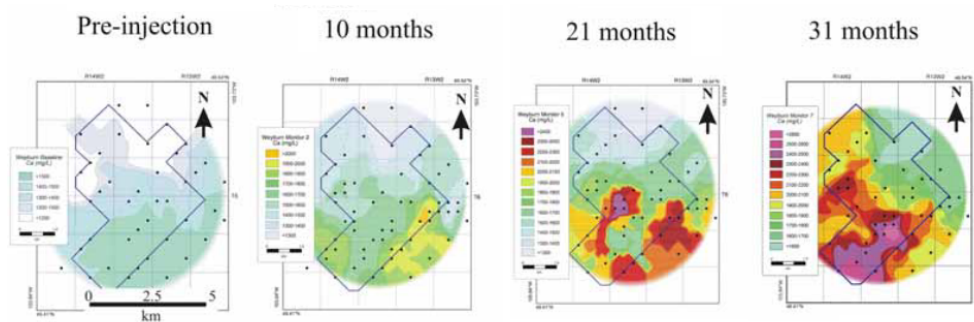
Figure 2.11: Ca^{2+} in produced fluids at each stage in Weyburn field project. The black dots are the location of the sample wells [8].

out in horizontal direction, driven by the buoyancy force; the CO_2 plume forms as multi-tier distribution, because of the structure of the geoformation. The layers already existed before the formation of the CO_2 plume; In the upper layers, the CO_2 continues to migrate laterally, while in the lower layers, the lateral spreading is limited and becomes fainter. (2) As shown in Figure 2.9(b), the CO_2 in the topmost layer has continued to expand since it developed in 1999 [65]. The CO_2 migration along the north direction is significant, and occurs because of the north-trending topographic ridge. Apart from this, the survey suggests that permeability of the Utsira sand of the strata plays an important role in inducing the plume motion [7]. In 2003, surveys of the Sleipner project showed that the CO_2-saturated brine eventually becomes denser and sinks, which avoids the potential for long-term leakage [66]. In 2009, the monitoring results indicated that CO_2 is being restrained by the low-permeability mudstone (4×10^{-19} m^2) in the reservoir site [7]. Thus, the reservoir structure and permeability of the rock are two important factors regarding the migration of CO_2. These observed results have been used to help design the modelling to investigate the fate of the injected CO_2 [67] [68] [7].

2.4. Reviews of the experimental investigation of CO_2 geological storage

The Weyburn CO_2 Enhanced Oil Recovery (EOR) project operated in Saskatchewan, Canada, has injected 6500 t/day CO_2 since 2000. By June 2010, 16.1 Mt CO_2 had been stored. As a practice transition of CO_2 EOR to CO_2 long-term storage, the project investigates the site characterization and wellbore integrity, monitors the motion of the injected CO_2 and conducts performance assessment of the risk of migration from the injection zone at a depth of 1500 m depth to the surface [69]. The behavior of the CO_2 in the Weyburn field is monitored by using the techniques of surface seismic, vertical seismic and cross-well seismic profiles, together with tracer injection monitoring [70]. The survey detected carbon isotopes $\delta^{13}C_{HCO_3^-}$ produced by supercritical CO_2 dissolution in short term and mineral dissolution in long term, and Ca^{2+} produced by the mineral dissolution $(CaCO_3 + H_2O + CO_2 \rightarrow Ca^{2+} + 2HCO_3^-)$. The monitoring results identified that CO_2 dissolution and mineral reactions did occur. Figure 2.10 shows that $\delta^{13}C_{HCO_3^-}$ values decrease from -1 - -7 per mil to -4 - -11 per mil after 10 months, due to the dissolution of the injected CO2. The mineral dissolution is also realized by the continued increase of the concentration of Ca^{2+} in the produced fluids, as shown in Figure 2.11. The monitoring results from this project provide important information for assessment of the dissolution and mineral reactions during the underground CO_2 storage. Based on more than 10 years of experience, the monitoring results indicate that the Weyburn reservoir is a suitable place in which to store CO_2 and there do not appear to be any changes in chemistry of the shallow groundwater [69].

In Salah field project, CO_2 has been injected at the rate of approximately 1Mt/yr through three horizontal wells into the lower permeability zone at the base of the gas reservoir, a Carboniferous sandstone reservoir in Algeria since 2004. By 2013, it had stored 3.8 Mt of CO_2 at a depth of 1.9 km with a thickness of 20-25 m below the Earth's surface [71]. In this project, the change of the sub-surface pressure induced by CO_2 injection has been measured by Interferometric Synthetic Aperture Radar (InSAR) [71]. The vertical leakage has been monitored by the technologies of 3D/4D seismic imaging, microseismic imaging, shallow aquifer monitoring and soil gas sampling [71]. In addition, monitoring of the wellbore leakage has been carried out by the technologies of annulus monitoring, casing logging and soil gas sampling [71]. The monitoring results indicate that surface uplift occurred as a result of the injection of CO_2, which is useful to understand the

behavior of the subsurface CO_2 in the aquifer [71]. Short-term modelling has been used to predict the movement of CO_2. The results suggest that approximately 25% of the injected CO_2 migrated to the lower caprock before well injection ceased in July 2007. These studies reveal that in the early injection stage, it is important to understand the structural geological and rock mechanical aspects of the storage system. Moreover, during long-term storage stage of 100-1000 years, the distribution of CO2 is related to the fracture network and the fracture flow [72]. Since In Salah project is relatively new, only a limited amount of data have been published. More insights will be gained in the following years [71].

In the laboratory scale, studies are focused on investigating the mechanism of multi-phase flow in porous media, including physical-chemical and transport properties or parameters, such as relative permeability [73] [74], capillary pressure [9] [75] [76], heterogeneities [77], CO_2 solubility [78] [79] [80], CO_2 dispersion [28], and interfacial tension [81] [82], which are primary factors to evaluate the storage integrity of the reservoir [4].

Among these characteristics, the relative permeability and capillary pressure are regarded as the crucial impacts on the processes of injection, migration and storage of CO_2 in porous media [73] [83]. A series of simulations studies found that these two parameters are important to predict the fate of the injected CO_2, because the distribution of CO_2 is sensitive to these parameters [84] [85].

Capillary pressure in porous media is defined by the force required to push the droplet through the porous media, which is against the interfacial tension between two phases [86]. It increases with the decrease of the diameter of the pores. The capillary pressure is related to the normalized water saturation and given by

$$P_c = cS_w^{-a} \tag{2.2}$$

where P_c and c are the capillary pressure and entry capillary pressure, respectively. S_w is the normalized water saturation, and a is the pore-size distribution index.

Relative permeability, as a dimensionless parameter, is given as the ratio of the effective
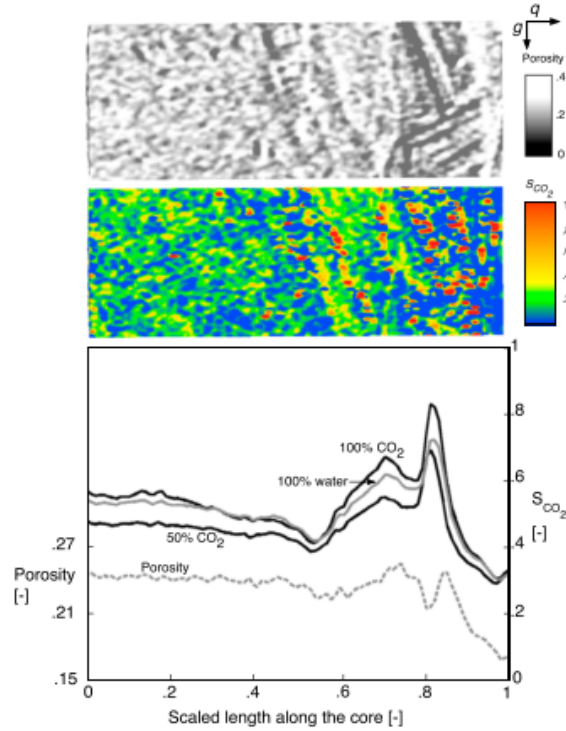
Figure 2.12: Top: A porosity mapping along the center of the core. Middle: CO_2 saturation mapping in the case of 100% water flooding following 100% CO_2 flooding. Bottom: averaged porosity and the CO_2 saturation alone the core in three different condition, 50% CO_2 flooding, 100% CO_2 flooding and 100% water flooding, respectively [9].

permeability to the absolute permeability [87]. It is defined by

$$\kappa_{ri} = \kappa_i / \kappa \tag{2.3}$$

where κ_{ri} is the relative permeability, κ_i is the permeability of phase i, and κ is the absolute permeability of the porous media with a single phase. The relative permeability is a function of water saturation. It is often described by the relative permeability-saturation curve, which is determined by the experimental measurement of the drainage and imbibition. Drainage is a process in which a non-wetting fluid is injected into a media saturated with the wetting fluid. Imbibition occurs when a non-wetting fluid is displaced by a wetting fluid.

A series of experiments on the capillary force have been carried out in the Laboratory of Dr. Sally Benson to investigate CO_2 residual trapping in Reservoir rocks by 3D mapping [77] [74] [76] [9] [83]. Krevor et al. investigated the residual trapping by injecting CO_2
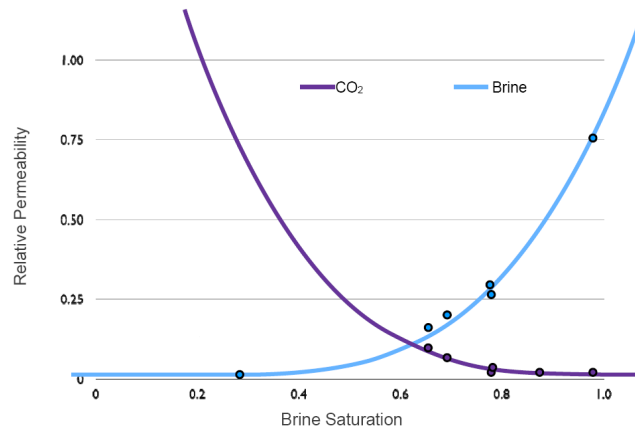
Figure 2.13: Relative permeability curves by the laboratory experiment [10].

into four rocks samples (Berea, Paaratte, Mt. Simon and Tuscaloosa); the experimental results show that capillary pressure restricts maximum CO_2 saturation [83]. Krevor et al. carried out another laboratory observation to monitor the effect of capillary force and heterogeneities on the trapping mechanisms, by injecting CO_2 through the Mt. Simon sandstone core at P=9 MPa and T=323 K [9]. The core sample is comprised of two parts, upstream homogeneous sand (10cm) with high porosity (0.23-0.26) and downstream sand (3 cm) with low porosity (0.17). The cross-bedding can be clearly seen in the top figure of Figure 2.12. The experimental results of CO_2 saturation, as shown in the middle and bottom of Figure 2.12, indicate that capillary barriers can immobilize the CO_2 plume, since the higher CO_2 saturation appears before the capillary barriers. The comparative test suggested that the CO_2 saturation without the capillary barriers is 1/4-1/7 of that with capillary barriers [9]. Based on a number of laboratory studies the relationship between the capillary pressure and brine saturation in three sample cores under 5 types CO_2 injection are obtained [10], as shown in Figure 2.13 and Figure 2.14. The capillary pressure reduces with the increase of the brine saturation. In addition, the relationship between capillary pressure and brine saturation depends on the porosity or permeability and the type of CO_2 injection [10].

Studies of the heterogeneity effect on the migration of CO_2 found that the volume of residual trapping depends on the heterogeneity [88] [28]. Aggelopoulos et al. [28] investigated the CO_2 dissolution in water-saturated porous media by measuring the gas pressure in the laboratory scale. The experiment results indicated that CO_2 dissolution is related
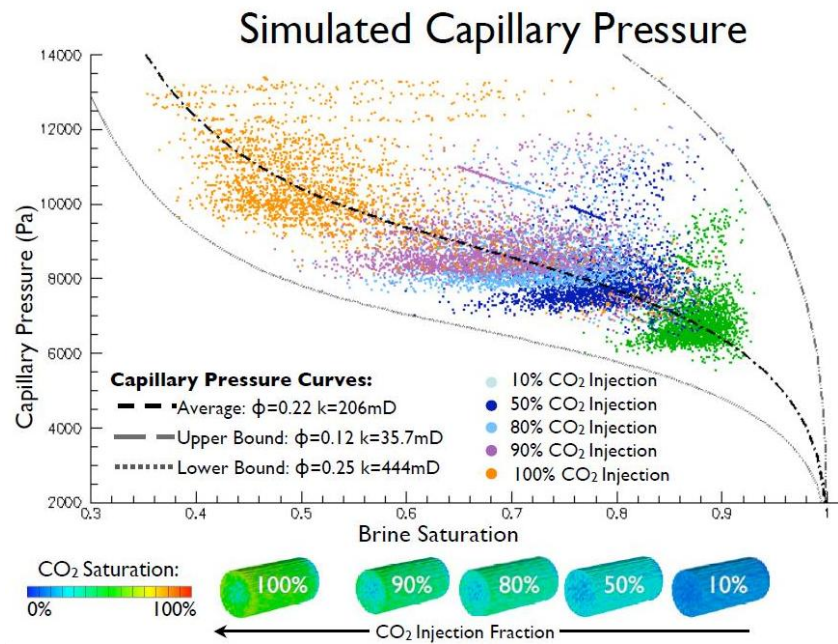
Figure 2.14: Capillary pressure varies with brine saturation [10].

to micro-heterogeneity. The same conclusion was found in a study by Zuo et al. [74]. The CO_2 dissolution rate in coarse-grained sorted sand appears to be higher than that in uniform beads [28]. The heterogeneity effect has been investigated in laboratory studies, which have not yet established how to upscale to the reservoir scale. One apparent fact is that the heterogeneity of the sample core cannot fully represent the heterogeneity of the reservoir [89].

2.5 Numerical Simulations for CO_2 geological storage

Numerical simulation is an effective method with which to understand the long-term fate of CO_2 in geological storage. According to the spatial scale, modelling of CO_2 geological storage can be classified into four scales: Pore scale (10nm-10cm), Reservoir Scale (10cm-100m), Site scale (100m-10km) and Regional scale (10km-1,000km) [13].

Researches on different scales have focused on specific problems of the CO_2 geological storage. In general, the investigation in regional and site scales focus on cost and decision-making, while in pore and reservoir scales the models tend to be concerned with physics. The focus of this study is on reviews of CO_2 geological storage in pore and reservoir

2.5. Numerical Simulations for CO_2 geological storage
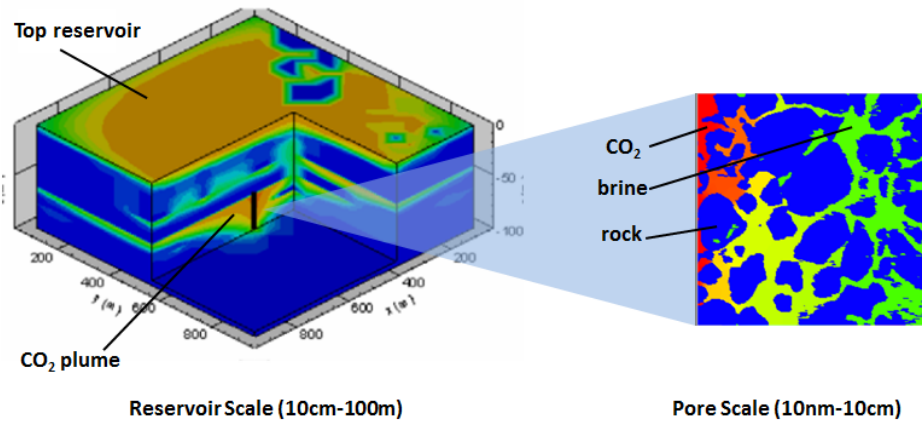
Figure 2.15: Illustration of CO_2 storage modelling at reservoir and pore scales.

scales, as shown in Figure 2.15.

In region scale, the investigation aims to optimize the infrastructure for CO_2 geological storage. A number of simulation models have been proposed to optimize the distribution of sources and the pipeline connection, in order to reduce the total cost [90] [91].

In the Site scale, the investigation is applied to select the CO_2 storage site and assess the safety and effectiveness of the storage site. A number of models have been developed [92]; these are the Features, Events, and Processes (FEP) scenario approach [93], Probabilistic Risk Assessment (PRA) method [94], Predicting Engineered Natural Systems (CO_2-PENS) [95] and Certification Framework (CF) model [96].

Among these models developed in the site scale, the CO_2-PENS and CF models are the system model, which take into account the entire system. Viswanathan et al. developed the system model CO_2-PENS, which incorporates the modules of CO_2 capture, pipelines transportation, subsurface injection, wellbore release, plume extent, atmospheric dispersion and economic considerations in different time-scales [97] [95]. The model operates under the assumption of a homogeneous and isotropic reservoir. The governing equations include the CO_2 mass balance, flow rate and cost [95]. Based on Darcy's law, this model can be used to calculate the injection capacity of wells by $Q = \frac{(P_w - P_{inf})4\pi kB}{[ln(t_d) + 0.80907]\mu_c}$, P_w and P_{inf} are the pressure at the wellbore and reservoir pressure, respectively; k is the averaged reservoir permeability; μ_c and B are the viscosity of CO_2 and thickness of the formation, respectively. The dimensionless time $t_d = \frac{kt}{\phi \mu_c c r_w^2}$, ϕ and r_w represent porosity and the

radius of well bore, respectively; t is time. In addition, the number of wells used at each time step is updated according to the capacity, and consequently affects the economic module. In the plume extent module, the plume thickness can be obtained by an analytical expression [98], and the plume radius is restricted by the reservoir radius. The drawback of this model is that broad and complex data is needed to reduce uncertainty [96].

In order to develop a simple model to assess the CO_2 geological storage, Oldenburg proposed another system module, called the CF model [96]. The CF model focuses on CO_2 storage, without considering capture, compression and transportation [96]. It is assumed that the capture, compression and transportation have been well evaluated by other risk framework models, and that the well and faults are the only potential leakage pathways in CF [96]. CO_2 leakage risk(CLR) is defined by [99]

$$CLR = Impact \times Probability_a \times Probability_b \times Probability_c \qquad (2.4)$$

where Impact is the CO_2 concentration or flux into the compartment, and $Probability_a$, $Probability_b$ and $Probability_c$ are the probability of leakage from wells and faults, the probability of CO_2 coming into contact with the leakage pathways and the probability of the fault and well being sealed, respectively. The CO_2 plume movement is simulated by the reservoir simulation software using the multiphase flow simulator. Reservoir properties such as injection rate, porosity, permeability, thickness and dip are the input parameters. If the CLR is less than the threshold, the potential site is viewed as an the effective trapping site. Otherwise, the input parameters are adjusted to find a new site [96].

In the Reservoir scale, physical modelling is used to understand the evolution of the CO_2 plume after injection, the storage capacity and CO_2 leakage rates. The CO_2 geological storage is descried by the multi-phase multi-component fluids flow. The modellings is based on empirical Darcy's law for momentum transport and conservation equations of mass and energy. A number of commercial numerical simulators are used to investigate the multi-phase multi-component fluids flow; these are listed in Figure 2.16 [11]. The different finite forms are used in these simulators to solve the governing equations, including finite element such as CODE-BRIGHT [100], FEFLOW [101], FEHM [102], IPARS-CO_2

2.5. Numerical Simulations for CO_2 geological storage

Simulators	Main applications	Numerical features (methods for discretisation/integration)
CHILLER (companion to SOLVEQ)	Multi-component multi-phase equilibrium geochemical calculation software based on minimum free-energy	Newton–Raphson method for solving a system of mass balance and mass action equations
CODE-BRIGHT	Solution of the flow, heat and geo-mechanical model equations	Finite element method for spatial discretisation; implicit finite-difference for temporal discretisation
COORES	Multi-component three-phase and 3D fluid flow in heterogeneous porous media	Finite volume method for spatial discretisation; implicit temporal discretisation
DUMUX	Multi-scale multi-physics toolbox for the simulation of flow and transport processes in porous media	Vertex-centred finite volume method for spatial discretisation; implicit temporal discretisation
ECLIPSE	Three-phase and 3D fluid flow in porous media with cubic EOS, pressure dependent permeability values, etc.	Integrated finite difference method (IFDM) with irregular spatial discretisation; implicit temporal discretisation
ELSA	Semi-analytical tool to estimate fluid distributions and leakage rates involving vertically integrated sharp-interface equations and local 3D well models	Spatial discretisation is essentially grid free; several schemes for temporal discretisation including implicit pressure explicit saturation, etc.
FEFLOW	Solving the groundwater flow equation with mass and heat transfer, including multi-component chemical kinetics	Finite element method for spatial discretisation; implicit/explicit/Crank–Nicolson temporal discretisation
FEHM	Fully coupled heat, mass and stress balance equations for 3D, non-isothermal, multi-phase fluid flow in porous media	Control volume finite element method for spatial discretisation; implicit temporal discretisation
GEM	EOS compositional reservoir simulator	IFDM for spatial discretisation; implicit temporal discretisation
Geochemist's workbench	Interactive aqueous geochemistry tools	Equilibrium modelling, reaction path modelling calculations, etc.
IPARS-CO_2	Parallel multi-block, multi-physics approach for multi-phase flow in porous media	Mixed finite element method for space discretisation; implicit pressure, explicit concentration sequential algorithm for temporal discretisation
MIN3P	Multi-component reactive transport modelling in variably saturated porous media	Finite volume method for spatial discretisation; implicit temporal discretisation
MODFLOW	Solving the groundwater flow equation to simulate the flow through aquifers	Finite difference method for spatial discretisation; implicit or Crank–Nicolson for temporal discretisation
MT3DMS	Modular 3D transport model simulating convection, dispersion, and chemical reactions of dissolved constituents	Finite difference/particle-tracking based Eulerian–Lagrangian/finite-volume method for spatial discretisation; implicit/explicit temporal discretisation
MUFTE	Isothermal and non-isothermal multi-phase flow problems including compositional effects	Vertex-centred finite volume method for spatial discretisation; implicit temporal discretisation
PFLOTRAN	Parallel 3D reservoir simulator for subsurface multi-phase, multi-component reactive flow and transport based on continuum scale mass and energy conservation	Finite element method for spatial discretisation; implicit/semi-implicit time integration
PHAST	Simulating groundwater flow, solute transport, and multi-component geochemical reactions	Finite difference method for spatial discretisation; implicit or Crank–Nicholson for temporal discretisation
PHREEQC	Low-temperature aqueous geochemical simulator	Based on an ion-association aqueous model; chemical equilibrium, kinetic, transport, and inverse-modelling calculations
RETRASO	Reactive transport of dissolved and gaseous species in non-isothermal saturated or unsaturated problems	Direct substitution approach for solving the reactive transport equations
ROCKFLOW	Multi-phase flow and solute transport processes in porous and fractured media	Finite element method for spatial discretisation; implicit temporal discretisation
RTAFF2	2D/3D non-isothermal multi-phase and multi-component flow	Finite element method for spatial discretisation; implicit temporal discretisation
SUTRA	Fluid movement and transport of either energy or dissolved substances in a subsurface environment	Hybrid finite element and integrated finite difference method for spatial discretisation; implicit temporal discretisation
TOUGHREACT	Chemically reactive multi-component, multi-phase, non-isothermal flows in porous and fractured media	IFDM for spatial discretisation; implicit temporal discretisation

Figure 2.16: Overview of the numerical simulator for geological storage [11].

[103], ROCKFLPW [104], RTAFF2 [104] and SUTRA [105], finite difference including ECLIPSE [106], MODFLOW [107], PHAST [108], SUTRA [109] and TOUGHREACT [110], and finite volume methods such as COORES [104], DUMUX [111], MIN3P [112], MT3DMS [113] and MUFTE [114] for spatial discretization. The finite element method is a mathematical method using simple element equations in sub-domains to approximate a complex partial differential equation in a large domain, based on the idea that the larger circle can be discretized by a number of connecting tiny straight lines. The finite difference method uses finite difference equations to approximate the solution, for example a Taylor series expansion, by discretizing the domain into a uniform grid. The finite volume method uses the volume integral form of the governing equations to approximate the solution, by discretizing the domain into uniform control volumes. A comparison study

2.5. Numerical Simulations for CO$_2$ geological storage
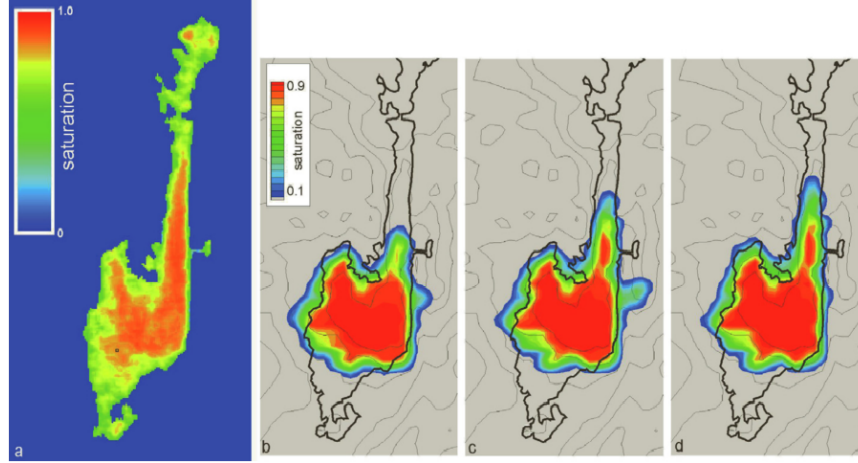
Figure 2.17: Modeling results of topmost layer comparison in horizontal scale. a) Observation results of the topmost CO$_2$ layer in 2006; b) TOUGH2 simulation assuming with 3 Darcy permeability; c) with 3/10 Darcy. Note 1 Darcy=9.869233×10^{-13} m^2.

using twelve different commercial simulators was applied to investigate the benchmark cases in CO$_2$ geological storage [104]. The CO$_2$ leakage rates under different models was obtained with the curve trend, while the differentiation was apparent in the results from the different models, even using the same code by the different modellers [104]. A similar conclusion was reached by Jiang et. al. [11]. This suggests that the simulator successfully analysed the impacts of the CO$_2$ plume in saline storage; meanwhile, the differences between the numerical simulation and experimental results are difficult to ignore, and this may be the result of the uncertain parameters and mechanisms. It has been found that the accuracy of the simulator relies on the experimental data; however, this is not available in the published paper [11].

The TOUGH family of codes such as TOUGH2 and TOUGHREACT have been widely used as one common simulator to investigate the behaviors of CO$_2$ in saline formation storage, which is a multicomponent multiphase flow simulator in one, two, or three dimensions for water, CO$_2$ and salt (NaCl) [59]. TOUGH2 has been developed since 1991. It uses an extension of Darcy's law to describe fluid advection. It also includes diffusive mass transport, conduction and convection. The basic mass or energy equation conservation is defined by

$$\frac{d}{dt}\int_{V_n} M^k dV_n = \int_{\Gamma_n} F^n \cdot n d\Gamma_n + \int_{V_n} q^k dV_n \tag{2.5}$$

2.5. Numerical Simulations for CO_2 geological storage
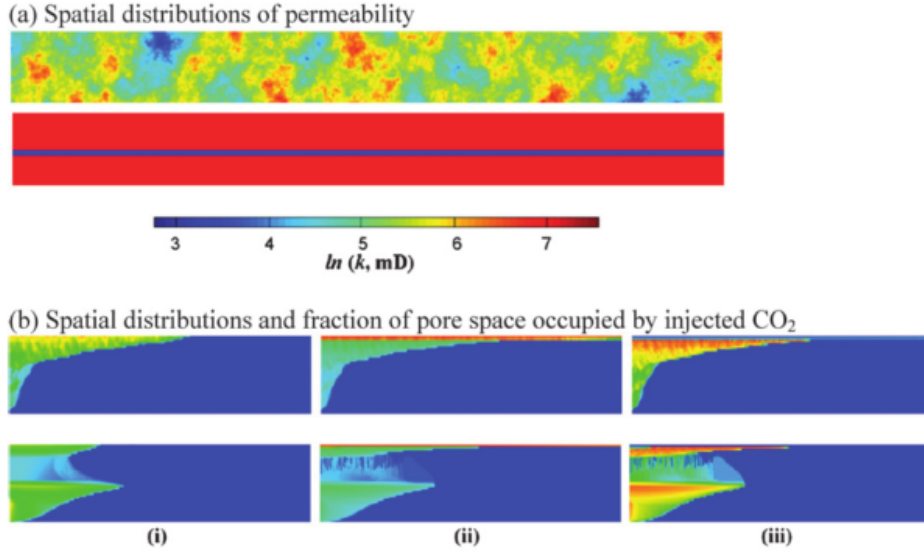
Figure 2.18: The simulation results of permeability effect on deep saline formations storage.(a)top one is heterogeneous sample with random permeability and the bottom one is a sample with two higher permeability layers separated by a low permeability layer. (b)the distribution of CO_2 saturation on three periods. S_g is the CO_2 saturation. [12]

where V_n and Γ_n are the arbitrary sub-domain and the closed surface, respectively. M represents mass or energy per volume. The superscript k indicates the mass components such as water, CO_2, air and H_2, k=1,...NK, and k=NK+1 presents the heat component. F is the mass or heat flux. q is the sources term. n demotes the normal vector on $d\Gamma_n$. Continuous space and time are discretized by the integral finite difference method(IFDM) [115] [116] and the fully implicitly first-order backward finite difference method, respectively. In comparison with the conventional finite difference, IFDM is suitable for regular and irregular discretizations in 1D, 2D and 3D, without any reference to the global coordinates [110]. The simulation results using TOUGH2 were compared with an experiment investigating the CO_2-driven convection in CO_2 saline storage [117]. It was concluded that similarities were found in the finger formation, while differences in the finger distribution and convection were apparent [117]. The application of TOUGH2 in capillary heterogeneity trapping of CO_2 suggested that capillary barriers prevent CO_2 plume migration; while these results are similar to the findings of the experiment, there are also difference [9].

Some studies also implement TOUGH2 to investigate capillary pressure, permeability, storage capacity and mass transfer [118] [58] [42] [117] [119] [9]. TOUGH2 has been

2.5. Numerical Simulations for CO_2 geological storage
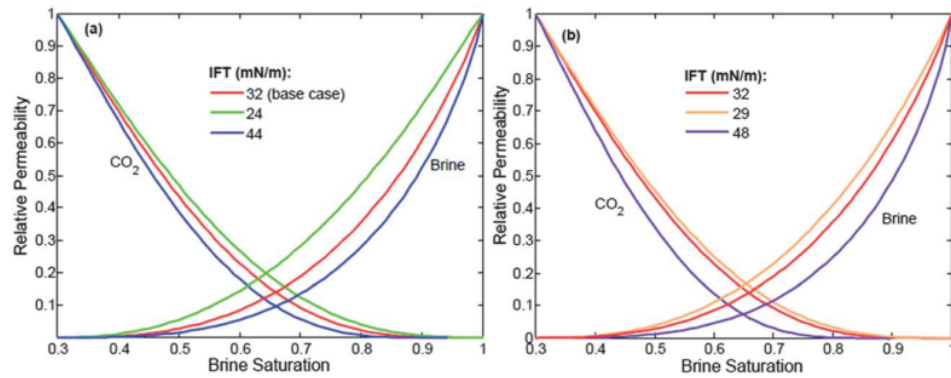
Figure 2.19: Effect of IFT on the CO_2 relative permeability - brine saturation curve [13].

used to study the migration of CO_2 in the Sleipner project. However, a discrepancy was found in the modelling results. Figure 2.17 illustrates the simulation results obtained by TOUGH2 [110]. The simulation results have not been successfully matched with the observation, especially in the lateral direction. The factors of the mismatch were estimated to be the modelling assumptions, such as reservoir permeability and anisotropy, CO_2 properties and topseal topography [7]. Orr et al. [12] investigated the impact of permeability and CO_2 saturation on large-scale storage using TOUGH2, using two samples; one was a heterogeneous sample with random permeability, while the other was a sample with two higher permeability layers separated by a low permeability, as shown in Figure 2.18(a). The CO_2 is injected on the left hand side. The simulation results of spatial distribution by injected CO2 at some time steps are shown in Figure 2.18(b). It can be seen that in the heterogeneous sample with random permeability, the lateral migration of the injected CO_2 in the upper layer is greater than that in the lower layer, which is related to the buoyancy force. On the other hand, the results of the three layer permeability sample show that the distribution of the CO_2 plume is discontinued in the vertical direction. The distribution is layered by the middle low permeability zone. All of the results indicate that the distributions of the CO_2 plume in each sample are different and are sensitive to the permeability. The simulation results produced the same conclusion that of the experimental observation. Therefore, the investigation of detailed modelling constraint restricts the accuracy of CO_2 plume prediction [7].

Apart from the commercial simulator, some researchers have developed codes to study CO_2 geological storage. Qi et al. extended the 3D field scale streamline simulator [120],

which is widely used in the oil industry, to investigate CO$_2$ migration in aquifer and oil reservoirs, including the thermodynamic model of mutual dissolution between CO$_2$ and water [121]. The traditional streamline simulator is a grid-based model with two phases, aqueous and hydrocarbon, and two components, water and oil, which is used to simulate advective transport in a heterogeneous system [120]. Qi et al. extended the model to four components, CO$_2$, water, oil and salt, and three phases, namely aqueous, hydrocarbon, and solid. CO$_2$ exists in the hydrocarbon, aqueous and solid phases. Salt exists in both aqueous and solid phases. Water is in both the hydrocarbon and aqueous phases. Oil only exists in the hydrocarbon phase. The saturation and concentration of each phase are obtained by the phase equilibrium, based on mass conservation. The velocity is calculated by Darcy's law. The streamlines are applied to track the grid at each time step by used of the Pollock method [122]. The modelling results proposed that in order to increase storage efficiency, simultaneously injecting CO$_2$ and water, followed by the injection of brine, is more effective than injecting only CO$_2$ [121]. It also suggested that capillary trapping is an effective mechanism for long-term CO$_2$ storage. Middleton et al. investigated the interfacial tension (IFT) effect on the CO$_2$ relative permeability-brine saturation curve at an offshore storage site using the Finite Element Heat and Mass transfer code [13]. As the IFT is related to the pressure, temperature and salinity, the IFT varies according to the different storage depth. The simulations were carried out in two site samples. Sample one is a relatively shallow regime at 800 m - 1360 m depth, corresponding to IFT in the range of 19-49$\times 10^{-9}$ N/m. Sample two is a deeper regime at 1360 m - 3000 m depth, corresponding to IFT in the range of 29-48$\times 10^{-9}$ N/m. The simulation results, shown in Figure 2.19, show that the CO$_2$ relative permeability-brine saturation curve is related to the IFT in both samples. The lower IFT obtained the higher relative permeability.

A growing number of investigations are being conducted in the reservoir scale. However, because of the inaccuracies from Darcy's law induced by the physical process in the reservoir scale, investigations at pore scale are crucial in order to understand CO$_2$ geological storage [123]. Furthermore, the results obtained at pore scale can be used to improve modelling in the reservoir scale.

At pore scale, the main purpose is to investigate the key parameters and physical-chemical process in multiphase multicomponent flow, which are not achieved in the larger scale

simulations. For example, the effect of capillary number, viscous fingering in the displacement fronts, gravity number and CO_2 dissolution and dispersion on the fluid flow can be investigated at pore scale, while not captured in larger scale model. Another purpose of the simulation modelling at pore scale is to determine the constitutive parameters used in upscaled modelling, such as relative permeability and CO_2 solubility [13].

The capillary number is defined by the ratio of viscous force to interfacial tension,

$$Ca = \frac{\mu U}{\sigma} \tag{2.6}$$

where μ and σ are the dynamic viscosity and interfacial tension, respectively. U is the characteristic velocity. The capillary number is related to the behavior of a two-phase flow at pore scale. The gravity number is the ratio of gravitational force to the viscous forces. It is defined by $Gr = \frac{\Delta \rho g k}{\mu U}$, where $\Delta \rho$ is the density difference, g is the gravitational acceleration, k is the permeability, U is the characteristic velocity and μ is the dynamic viscosity. Viscous fingering occurs between two fluids, and is the result of the different viscous or density of two fluids in porous media. In CO_2 geological storage, unstable fingering in the displacement fronts reduces the capacity for sequestration and it is still not well understood [123].

Published pore-scale modelling studies of CO_2 geological storage are rare [16] [123] [89] [124] [125] [126] [127]. The research at pore scale tends to focus on CO_2 dissolution and dispersion into water [128] [125] [129], capillary trapping [89], relative permeability [130] and solid dissolution [124].

The aims of modellings at pore scale are to simulate multi-phase or multi-component flows with moving and deformable interfaces deriving from the interactions among fluid molecules. The conventional computational fluid dynamic (CFD) method cannot be used to model CO_2 geological storage, because the grid needs to be fine enough to simulate the CO_2/brine multiple phase flow [11]. The simulation methods, applied in CO_2 geological storage at the pore scale, include the pore-throat method [16], Smoothed Particle Hydrodynamics model [89], pore-network modelling [126] and the Lattice Boltzmann method [124] [125]. Most of the simulations at the pore-scale apply the Lattice Boltzmann method, considering gravity, viscous force and capillary force [89]. The Lattice
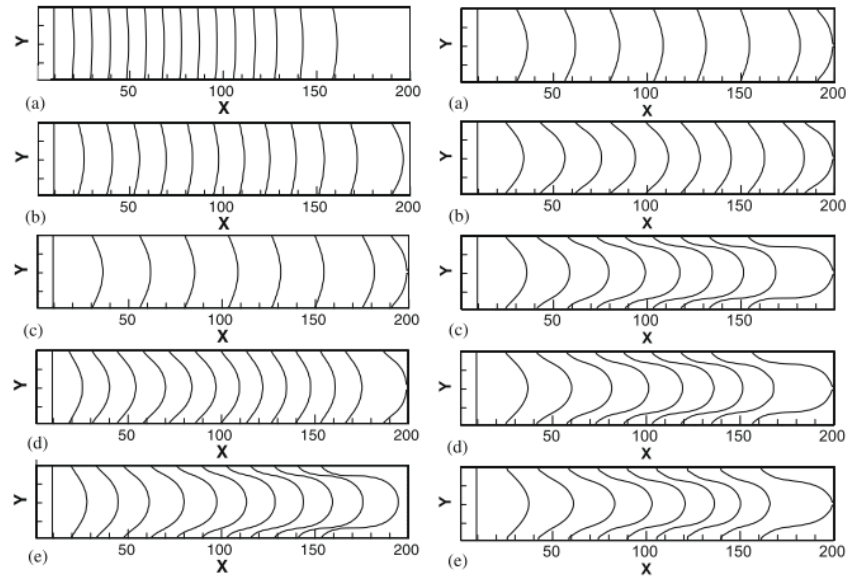
Figure 2.20: Left column: the effect of Ca number on fingering phenomenon with M=1 (a) Ca=0.0091, Δt=1000; (b) Ca=0.0274, Δt=500; (c) Ca=0.0457, Δt=500; (d) Ca=0.064, Δt=200; (e) Ca=0.0732, Δt=200. Right column: the effect of viscous ratio on fingering phenomenon (a) M=1, Δt=1000; (b) M=2, Δt=400; (c) M=3, Δt=400; (d) M=4, Δt=400; (e) M=5, Δt=400. [14]

Boltzmann method is regarded as a promising method with which to simulate the pore-scale multiple phase multiple component flow in complex media such as porous media, as it is easy to control the fluid/fluid and fluid/solid interaction and the interface is formed automatically. More details of the Lattice Boltzmann method will be introduced in the next chapter.

The LBM has been used in studies of the physical mechanisms of viscous fingering at pore scale [131] [14]. Viscous fingering is becoming a concern in the industrial application of enhanced oil recovery by injecting CO$_2$, because it affects the recovery efficiency of oil. This viscous fingering also occurs in CO$_2$ geological storage, when the less viscous CO$_2$ displaces the more viscous brine/water in the porous structure. The understanding of the physical mechanisms and factors from the oil field can be also applied to CO$_2$ displacement in CO$_2$ geological storage.

Kang et al. [131] investigated the relative permeability saturation curve which varies according to the viscosity ratio, M=viscous of displaced fluid/viscous of displacing fluid, for multiphase flow in porous media. They achieved this by carrying out a series of numerical simulations of fluid displacement in a horizontal channel. The simulation results

of the relative permeability curve obtained from the Shan-Chen multiphase LBM model get a good agreement with the analytical results. Furthermore, Kang et al. evaluated the capillary number, viscosity ratio and wettability on the fingering phenomenon using the Shan-Chen multicomponent LBM model. The capillary number is defined by

$$Ca = \frac{u_t \rho_o v_o}{\sigma} \tag{2.7}$$

where u_t is the velocity of the interface in the center. ρ_o and v_o are the density and kinetic viscosity of the displaced fluid, respectively. σ is the surface tension. The simulation results suggested that the finger width decreases with the increase of M or Ca. Finger development is related to the wettability of the displacing fluid. The minimum capillary number forming a finger formation decreases with the reduction in the wettability of the displacing fluid.

Dong et al. also used the Shan-Chen multicomponent LBM model to investigate the effects of the Ca number (see Eq.2.7), Bo number, wettability and viscosity ratio on the viscous fingering phenomenon [14]. The Bo number represents gravity versus surface tension, $Bo = \frac{\rho g L^2}{\sigma}$, where ρ is the density, g is gravitational acceleration, L is characteristic length, and σ is surface tension. The simulation confirmed the ability of the LBM in the application of immiscible displacement studies. The results, as shown in left hand side of Figure 2.20(a)-(e), indicate that the curvature of the interface between two immiscible fluid increases with Ca. In addition, fingering is formed when Ca increases to 0.0732. Figure 2.20(b) shows that the viscosity ratio affects the fingering formation, while the relationship between the fingering length and viscosity ratio is not linear. Moreover, the simulations indicate that the Bo number significantly changes the contact point of the displacing fluid with the upper boundary. The simulation results got a good agreement with Kang's results in terms of the simulation results of the different viscosity ratios [131].

In addition to the investigation of the fingering phenomenon, fluid dissolution and solid precipitation occurring during CO$_2$ geological storage have been studied at pore scale. There has been some concern about this process, because it significantly changes the properties of the porous media, such as porosity and permeability [132].

Kang et al. [132] using the LBM method investigated the solid dissolution and precip-

itation in porous media with the different dimensionless numbers, Péclet and Péclet-Damköhler. Two lattices have been applied to describe the fluid flow and solid concentration, respectively. A special boundary condition, derived from the first-order kinetic reaction equation ($D_f \frac{\partial C}{\partial n} = k_r (C - C_s)$, where C and C_s are the solute concentration on the solid/fluid interface and the saturated concentration, respectively. D_f is the diffusivity, k_r is the reaction rate, and n is the normal direction pointing inwards the fluid), has been proposed to control dissolution and precipitation. The Péclet number and Damköhler numbers are defined by $Pe = \frac{UL}{D_f}$ and $Da = \frac{k_r}{U}$, respectively. U and L are the characteristic velocity and length, respectively. Pe is the ratio of advection to the molecular diffusion. PeDa is the reaction versus the molecular diffusion. The simulation results show that (a)PeDa>1 and Pe>1, the wormhole phenomenon has been observed. (b)PeDa>1 and Pe<1, the permeability slowly increases, as the dissolution occurs on the wall facing the inlet. The simulation results also found that the dissolution and precipitation cannot be reversed.

Huber et al. proposed another LBM model to investigate heterogeneous dissolution and precipitation in porous media [133]. Unlike Kang's dissolution/precipitation model [132] using the special boundary condition to describe the reaction, Huber's model includes the solid/fluid interface in the simulation domain. A flag variable is adopted to distinguish the advection-diffusion fluid and solid. It uses a Two Relaxation Time (TRT) model to represent the advection-diffusion fluid with the iterative. TRT offers the possibility of adjusting the advection-diffusion fluid function. The reaction of dissolution or precipitation has been imposed by the source/sink term. Regarding these two relaxation times, one is in the collision term, while the other is embedded in the source/sink term to control the solid diffusion. The simulation results indicate that permeability increases with the increase of Pe and the decrease of PeDa during the dissolution process and the relationship is the opposite for precipitation [133]

Parmigiani et al., coupling the thermal reactive model, known as enthalpy conservation to the Shan-Chen multicomponent LBM model, investigated the mass and reactant transport in porous media [15]. The simulations were carried out by injecting the non-wetting fluid into the porous media, which was filled with the wetting fluid. With the exception of two sets of particle distribution functions for wetting and non-wetting fluid, a set

2.5. Numerical Simulations for CO$_2$ geological storage
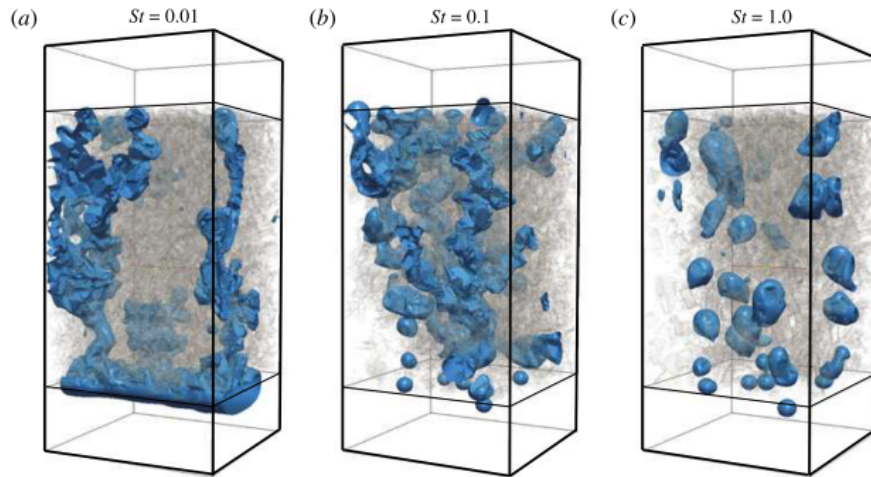
Figure 2.21: The effect of St number on the non-wetting fluid distribution in 3D porous media [15]

of particle distribution functions for the advection-diffusion was introduced to describe the temperature distribution. A source term and a sink term were applied to control the crystallization and melting, respectively. The simulation results, as shown in Figure 2.21, present that the capillary fingers distributions became unstable as the increase of St. The Stefan number is the ratio of enthalpy resulted by the dissolution/melting to the enthalpy kept in the system, which is defined by $St = \frac{c\Delta T}{L_f}$, where ΔT is the temperature difference between the non-wetting fluid and the melting temperature, c and L_f are the specific heat and the latent heat of fusion, respectively. Figure 2.21 shows that as St increase, the non-wetting fluid is not continuous and breaks into several slugs.

Apart from the LBM method, Ferer et al. proposed a two-dimensional pore-scale model to investigate the injection of CO$_2$ into the brine saturated reservoir [16]. This model includes a series of pore bodies with a finite volume connected by the throats, as shown in Figure 2.22. The model is based on the capillary pressure equation, known as Young-Laplace's Law, and volume conservation, assuming the pressure in the pore body is uniform. Young-Laplace equation is defined by $\Delta P = \frac{\sigma}{R}$, ΔP is the pressure difference on the fluid interface. σ is the interfacial tension. R is the radius of curvature. The modelling results suggest that the fractional saturation of CO$_2$ in two-dimensional porous media is related to the viscosity of CO$_2$. The lower viscosity CO$_2$ results in the low fraction saturation of CO$_2$ [16]. Bromhal et al. includes buoyancy forces into Ferer's model to
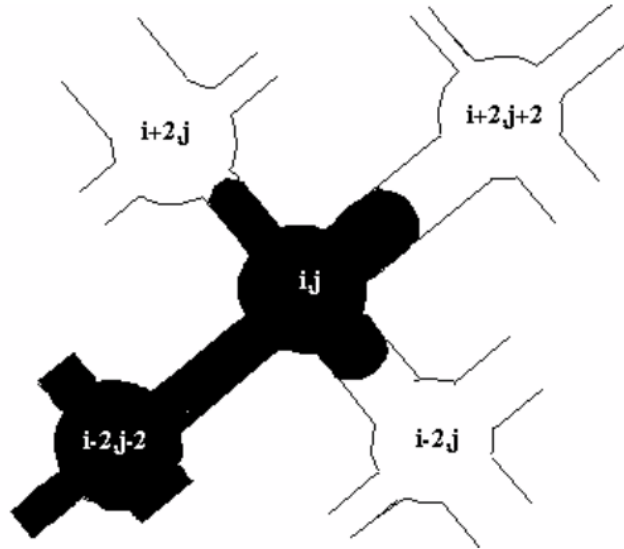
Figure 2.22: Two dimensional distribution of the throats and pore bodies of Ferer's pore-scale model [16]. The black fluid is the non-wetting displacing fluid. The white fluid is the wetting displaced fluid.

investigate the CO$_2$/oil flow in porous media, in terms of viscosity ratio and density ratio [123]. It was found that saturation decreases with the decrease of viscosity or density ratio.

Bandara et al. used the Smoothed Particle Hydrodynamics model to investigate the two-dimensional capillary trapping mechanisms at pore scale [89]. Ca and Gr are in the range of 0.0003-0.0345 and 0.21-39.27, respectively. The porous media is assumed by the uniform crossed distribution of a spherical circle. It was found that the proportion of trapped CO$_2$ relies on the balance between gravitational, capillary and viscous forces [89]. As Gr is high (e.g. Gr=24.5 and 39.27) and Ca is low (Ca=0.0305 and 0.0009), the gravity dominates the displacement of CO$_2$ and the gravity fingers are obtained, which gets a good agreement with the experimental observations [134]. CO$_2$ is driven to reach the caprock and the trapping fraction is approximately 60%. As Ca is low, the capillary force dominates the displacement of CO$_2$ and the CO$_2$ plume is discontinuous. The capillary force restricts the development of the CO$_2$ plume. A small fraction of the CO$_2$ is separated from the plume. As Gr is small, the trapped fraction of CO$_2$ depends on the capillary force [89]. The simulation results at pore scale agree with the results in Darcy scale [89]. In addition, the simulation results suggest that high injection rates obtain more effective capillary trapping.

Lopez et al. applied the pore-network modelling to investigate CO_2/brine displacement in porous media for the In Salah project [126]. The relative permeability curve confirms the experimental results [126]. The residual CO_2 saturation obtained by the simulation, 36%-44%, is a little higher than the experimental results: 15%-40%.

Raoof et al. used a multidirectional pore network model to investigate the effects of saturation on dispersion with the use of advection-dispersion equation [128]. The porous media was constructed of different angular forms of pores with a cubic shape. It concluded that dispersivity is strongly affected by saturation, and that relationship is not monotonic [128].

Overall, traditional numerical methods are inadequate for consideration of both small-scale and large-scale processes, and this may be the reason why the numerical simulation diverges from the monitored results. The investigation in each scale is important to comprehensively understand the CCS. The modellings in each scale supports the other and enables an exchange the information. In the upscaled investigation, it has been proven that the dissolution and capillary in the small scale impact on the migration and immobilization of CO_2 in the large scale [135]. Therefore, the models developed in the small scale can be used to support the upscaled models. In this study, the focus is on the pore scale study using the lattice Boltzmann method.

2.6   Summary

Global warming is regarded as a serious problem. The Carbon dioxide Capture and Storage is proposed as an effective approach to capture CO_2 emissions, store them and prevent them from being released into the atmosphere, leading to a reduction in the concentration of greenhouse gas in the atmosphere.

Of the two technologies of carbon dioxide storage techniques discussed above, ocean storage and geological storage, considering the impact on the ocean environment, geological storage appears to be a more effective mitigation option. Geological storage sites include deep saline aquifers, depleted oil and gas fields and coal beads.

2.6. Summary

Although CO_2 geological storage is underway in several places, the technology must be developed further for worldwide application on large scale as a primary pathway to cut CO_2 emissions. Because of the fact that natural seeps has occurred worldwide, understanding CO_2 storage mechanisms is obviously important and necessary to improve technologies and reduce assessment uncertainties, such as assessing risk, efficiency and safety problems. Answering these questions depends on understanding the complex mechanisms of geological underground storage, including the interplays of viscous, capillary, buoyancy forces and heterogeneity in geological formations. The studies of CO_2 geological storage in terms of the experimental investigation and numerical simulations are reviewed at various scales in this chapter.

It appears the investigation of the CO_2 geological storage at pore scale does contribute to understanding of the large-scale processes, and it has enabled improvement of large-scale models. However, few numerical simulations of CO_2 geological storage at pore-scale have been published. In comparison with investigations at other scales, one of the advantages of studies at pore-scale is that it can describe the motion of CO_2 in a relatively elementary volume by changing the properties and boundary condition.

Thus, in this study the focus is on the mechanisms investigation of geological storage at pore scale, which can be used firstly to answer the question of how CO_2 is stored and secondly what happens to the CO_2 in the storage state. A numerical simulation framework will then be built which provides the basis for the design, management and optimization of operations in CO_2 geological storage.

Chapter 3

Lattice Boltzmann method

3.1 Introduction

The objective of this thesis is to develop a novel numerical model of two-phase flows and mass transfer at pore scale. The first step is to choose the numerical scheme of multiphase/multicomponent fluids at pore scale to build up the model. Several methods are used to simulate multiphase flow at pore scale, such as Pore-network models (a network of pore volumes connected by channels) [130] [136] [128], Lattice Boltzmann method [137] [125] [138] [139] [124] [89], Smoothed particle hydrodynamics (SPH)(superposition of smooth bell-shaped functions) [140] and volume-of-fluid method (grid-based computational fluid dynamics with interface tracking) [141]. These pore-scale multiphase fluid flow methods have been reviewed in detail by Meakin et al. [142]. In this study, LBM is used to simulate multiphase/multicomponent flow at pore scale.

In comparison with other numerical methods, there are two primary advantages of the lattice Boltzmann model. Firstly, it achieves an effective algorithm to simulate the single phase or multiple phase/component fluid flows in complex geometries [143], such as the flow in porous materials [144]. Secondly, it enables utilization of the parallelize simulation process to reduce the computational time for the enormous operations [145]. Because of the variously successful applications, LBM has become a promising option for simulating single and multiphase fluids flow [144], especially for simulations of unsteady flows [146], phase separation [147], phase change [148], solute and heat transfer [149].

Lattice Boltzmann model (LBM) evolved from Lattice Gas Automata (LGA) and can be obtained by means of Boltzmann equation. Unlike conventional computational fluid dynamics methods which solve the discretization of macroscopic continuum equations,

the lattice Boltzmann method incorporates microscopic models and mesoscopic kinetic equations to make the macroscopic averaged properties obey the macroscopic equation [144]. The application of LBM in immiscible fluids flow (oil/water) in porous media has been investigated [150], such as the simulation of Enhanced Oil Recovery (EOR).

In this chapter, the evolution from LGA to LBM is introduced in Section 3.2. Since lattice Boltzmann equation is not only the evolution of LGA, but also can be obtained by discretization of the continuous Boltzmann equation, the discretization process from Boltzmann equation to lattice Boltzmann equation is described in Section 3.3. The LBM models for multicomponent fluids flow are reviewed in Section 3.4. The governing equations of LBM multicomponent multiphase are introduced in Section 3.5. Because the particles interaction is one of the key models of LBM, it was investigated, not only the introduction from literature review, but also the evaluation in Section 3.6. The boundary conditions is introduced in Section 3.7, following by the review of the challenges of LBM MCMP in Section 3.8. LB unit are introduced in Section 3.9. The applications of LBM in the simulation of mass transfer are reviewed in Section 3.10..

3.2 Lattice Gas Automata (LGA)

LBM is the evolution of the LGA, which is considered as the cellular automata methods used to simulate fluid flows utilizing the discrete space and time [151]. The LGA is a discrete system with a series of Boolean variables on the regular gird.

The first LGA was developed by Hardy, de Pazzis and Pomeau in 1973 [152], named the HPP model. The HPP model is a two-dimensional model with square lattices. It has been used to simulate sound waves [153]. However, it has been approved that the HPP model does not obey the Navier-Stokes equation, because of the insufficient degree of rotational lattice symmetry [154]. In 1986, a two-dimensional LGA was proposed by Frisch, Hasslacher and Pomeau (FHP) [155], which discovered the importance of the symmetry constraint and promoted the development of LGA [154]. The FHP used the triangular lattice, which has enough symmetry and recoveries Navier-Stokes equations of incompressible fluid dynamics [156]. The collision rule is based on the local conservation

of mass and momentum. Based on the FHP model, many LGA models have been introduced and applied in the simulation of fluid mixture [157] [158], chemical reaction [159] and the immiscible Cellular-Automaton model with interfacial tension [160].

However, considering about the defects of the LGA, such as lack of Galilean invariance, statistical noise, exponential complexity for three-dimensional lattices [161], the Lattice Boltzmann Models was introduced.

In the lattice gas automaton, a Boolean variables $n_i(x,t)$ (i=1,...,M) is used to describe the particles occupation on the nodes. M is the number of directions of the particle velocity. The evolution equation of LGA is given by

$$n_i\left(x+e_i,t+1\right)=n_i\left(x,t\right)+\Omega_i\left(n\left(x,t\right)\right) \tag{3.1}$$

where e_i is the local particle velocity. The Boolean field $n_i(x,t)$=1 or 0. $n_i(x,t)$=1 indicates the presence of the particle at site x. In contrast, $n_i(x,t)$=0 means the absence of the particle. The particles' moving is determined by the rule of collision ($\Omega_i\left(n\left(x,t\right)\right)$) and streaming ($n_i\left(x+e_i,t+1\right)=n_i\left(x,t\right)$). Streaming is the particles moving to its neighbor nodes in its velocity direction. Collision occurs as the particles interact with other particles and change the velocity direction by the scattering rules. Finally, the macroscopic quantities are obtained by counting the average over a large region to reduce the statistical noise. Therefore, the model is not efficient.

The improvement of LBM is to replace the Boolean variables $n_i(x,t)$ by the particle density distribution function f_i (mean numbers of particles), is introduced in Sec.3.3), and neglects the motion of individual particle [162]. The density distribution function is as the ensemble average of the Boolean variable. Consequently, the discrete collision is modified by the collision operator in LBM [161].

3.3 From Boltzmann equation to lattice Boltzmann equation

The lattice Boltzmann equation is not only the evolution of LGA, but also can be obtained by discretization of the continuous Boltzmann equation [163]. The Boltzmann equation describes the probability of a single particle within a given position and momentum by a distribution function f, for which the governing equation is,

$$\frac{\partial f}{\partial t} + \xi \cdot \nabla_x f + F \cdot \nabla_\xi f = \Omega(f) \tag{3.2}$$

where x is the particle's coordinate, ξ is the particle microscopic velocity, F is the external force, and Ω is collision integral. With assumption of homogeneous distribution for all particles, the collision term can be expressed by the BGK collision operator [164],

$$\frac{\partial f}{\partial t} + \xi \cdot \nabla_x f + F \cdot \nabla_\xi f = \frac{f - f^{eq}}{\lambda} \tag{3.3}$$

where λ is the relaxation time. The f^{eq} is the Maxwell-Boltzmann distribution function and defined by

$$f^{eq} = \frac{\rho}{(2\pi RT)^{(D/2)}} exp \left[-\frac{(\xi - u)^2}{2RT} \right] \tag{3.4}$$

where R is specific gas constant, D is the dimension of the space, and T is the temperature. The macroscopic density ρ and the velocity u can be obtained by

$$\rho = \int f d\xi \tag{3.5}$$

$$\rho u = \int \xi f d\xi \tag{3.6}$$

In lattice, continuous Boltzmann equation is discrete into a system, which is shown in Figure 3.1. In order to determine the discrete velocity, a Taylor-series expansion of Eq.3.4
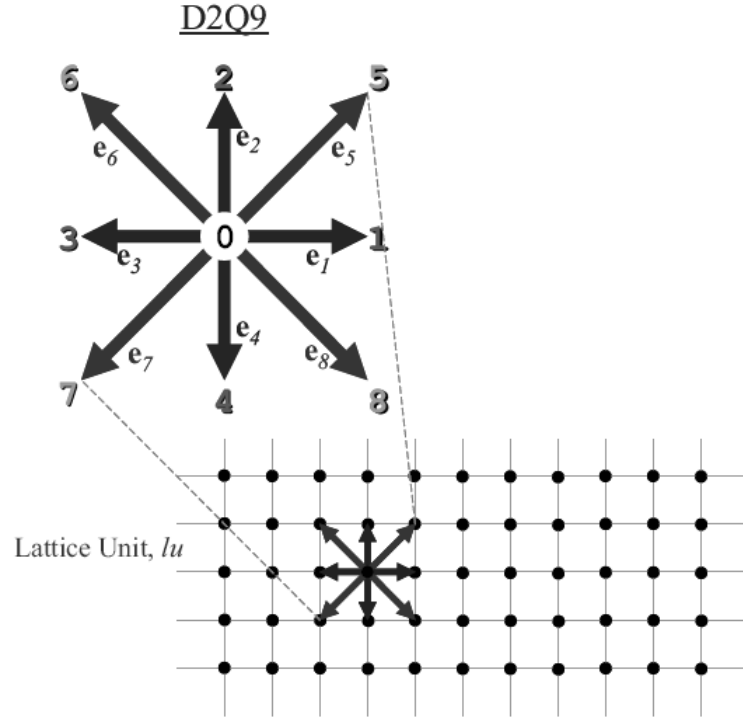
Figure 3.1: Discretization of the continuous domain

to second order in velocity u is obtained

$$f^{eq} = \frac{\rho}{(2\pi RT)^{D/2}} exp\left(-\frac{\xi^2}{2RT}\right)\left[1 + \frac{\xi \cdot u}{RT} + \frac{(\xi \cdot u)^2}{2(RT)^2} - \frac{u^2}{2RT}\right] \tag{3.7}$$

To get the correct Navier-Stokes equation, the selected discrete velocity is established as the accurate numerical integration

$$\int \xi^k f^{eq} d\xi = \sum_i w_i c_i^k f^{eq}(c_i), \quad 0 \le k \le 3 \tag{3.8}$$

where w_i and c_i are the weights of the numerical integration and the discrete velocity, respectively. A new distribution function is defined by $f_i(x,t) = w_i f(x,c_i,t)$. The evolution equation is given by

$$\frac{\partial f_i}{\partial t} + c_i \cdot \nabla f_i = -\frac{1}{\tau_c}\left[f_i - f_i^{eq}\right] \tag{3.9}$$

where $f_i(x,t) = w_i f(x,c_i,t)$ and $f_i^{eq}(x,t) = w_i f^{eq}(x,c_i,t)$. In Eq.3.9, only the velocity is discrete, both of the time and space are continuous. This equation is known as Discrete Velocity Boltzmann Equation. Correspondingly, the macroscopic density and velocity are

given by

$$\rho = \sum_i f_i \tag{3.10}$$

$$\rho u = \sum_i c_i f_i \tag{3.11}$$

Then, Eq.3.9 is discreted along the characteristic direction, a second order central difference equation is obtained

$$f_i(x + c_i \delta t, t + \delta t) - f_i(x, t) = -\frac{1}{\tau}\left[f_i(x, t) - f_i^{eq}(x, t)\right] \tag{3.12}$$

where $\tau = \tau_c / \Delta t$ is the dimensionless relaxation time. Eq.3.12 is the lattice Bhatnagar-Gross-Krook (LBGK) [164] equation. Therefore, the lattice Boltzmann equation is a finite difference of the continuous Boltzmann equation [163] and a second order accurate in both space and time [165].

3.4 Reviews of LBM multiple phase/component (MPMC) models

The LBM for immiscible multiple phase flow was originally developed from lattice gas model proposed by Rothman and Keller [160], which introduced "red" and "blue" colours to distinguish between two fluids. The collision rule is based on the conservation of fluid color, mass and momentum, and modified to satisfy the surface tension. The first LBM for immiscible fluids flow was developed by Gunstensen [166]. This LBM model introduced a two-step collision rule to produce surface tension. The first step is to add a perturbation to the particle distribution to obtain the surface tension. The perturbation is related to the colour-gradient on the interface. The second step is to recolor mass, based on the zero diffusivity rule between two colors [166].

Recently, three popular LBM models have been applied when investigating the MPMC fluids flow, namely the Shan-Chen (SC) model, the free energy model and the He-Shan-Doolen model.

The lattice Boltzmann MPMC was first proposed by Shan-Chen by introducing a non-

3.4. Reviews of LBM multiple phase/component (MPMC) models

local interaction force between particles at neighboring lattice sites in 1993, named the pseudopotential model (Shan-Chen model) [147]. As an alternative LBM method, Shan-Chen model has been widely applied in simulations of the multiple component fluid flow [167] [168] [169] and multi-phase flow [170] [171] [172], in which the internal and external forces are applied into the momentum equation, and in turn contribute to the change in density distribution as a result of the collision and stream rule. The advantages of the Shan-Chen model are that it is easy to trace the motion of interface between phases and to implement the forces in the model, such as buoyancy and interface tension. The main disadvantages of the Shan-Chen model are that the temperature is not introduced in the model directly, which is mimicked by the strength of the interparticle interaction; and that unphysical spurious velocity was found on the interface [173]. However, due to the clear physical concepts, the Shan-Chen model has been successfully applied in the simulation of interfacial phenomena such as the Laplace law for bubbles, capillary wave and viscous fingering phenomenon [131].

Swift et al. proposed a free energy model [170] [171] for non-ideal fluids in 1995. The primary advantage of this model is that temperature was well-defined in the model. In addition, spurious velocity is almost negligible, due to the benefit of local momentum conservation [1]. The model is suitable for simulation of a limited porous size and local momentum conservation is satisfactory. However, this model suffers from the unphysical Galilean invariance effect, because of the unphysical viscous stresses which cannot be neglected [174].

He, Shan and Doolen [175] proposed a LBM multiphase model for dense gases by kinetic equation with a BGK collision model in 1998, which was a revision of the Shan-Chen model. The mean-field theory has been used to study long-range intermolecular interaction. The capillary effect has been successfully analyzed by this model [175]. Molecular interaction and gravity forces are introduced in the collision operator. The kinetic equation in Enskog's theory satisfies the mass, momentum and energy equations. However, the model suffered from numerical instability with regard to complex fluid [1]. This numerical instability can be mitigated by improved numerical schemes [1].

In this study, the Shan-Chen's interparticle interaction pseudopotential model is adopted

and improved for the development of CO_2 dissolution model. The details of Shan-Chen model are described in the following sections.

3.5 Governing equations of LBM multiple phase/component (MPMC) models

In Shan-Chen LB model, the fluid is regarded as a series of discrete particles and characterized by the collision and stream rules. For multicomponent model, the dynamics of each component is described by a set of distribution function and equilibrium function, from which the macroscopic properties and momentum of fluid particles can be estimated. The interaction between fluid particles is imposed on the collision operator, and the details are discussed as follows.

The distribution function is used to represent the probability of particle molecules in a given space and time. Considering the component of σ, the distribution function of the component is governed by lattice Boltzmann equations with the LBGK [164] collision algorithm,

$$f_i^\sigma(x+e_i\Delta t, t+\Delta t) - f_i^\sigma(x,t) = -\frac{1}{\tau_\sigma}[f_i^\sigma(x,t) - f_i^{\sigma,eq}(x,t)] \qquad (3.13)$$

where the superscript *eq* denotes the equilibrium state. f_i^σ is the distribution function of σth component in the *ith* velocity direction with a given position and momentum. For the multiple phase model, f_i^σ denotes the mass density. For the multiple component model, f_i^σ is normally replaced by the population of the particles n_i^σ. The σth component has its own molecular mass m^σ and the population of the particles n_i^σ, $\sigma = 1, 2, ..., S$. S is the number of components. Therefore, $f_i^\sigma = m^\sigma n_i^\sigma$.

The terms on left and right hand side of Eq.3.13 are the stream and collision, respectively. τ_σ is the relaxation time parameter for this explicit scheme, related with macroscopic kinematic viscosity by $\tau_\sigma = \frac{1}{c_s^2}\upsilon_\sigma + \frac{1}{2}\Delta t$. c_s is the speed of sound for perfect gas. The

3.5. Governing equations of LBM multiple phase/component (MPMC) models

equilibrium distribution function for σth component can be described by

$$f_i^{\sigma,eq}(x) = \omega_i \rho_\sigma(x) \left[1 + 3\frac{e_i \cdot u_\sigma^{eq}}{c^2} + \frac{9}{2}\frac{(e_i \cdot u_\sigma^{eq})^2}{c^4} - \frac{3}{2}\frac{u_\sigma^{eq} \cdot u_\sigma^{eq}}{c^2} \right] \qquad (3.14)$$

where e_i is the velocity vector to indicate possible particles moving from one lattice node to the nearest-neighboring node. c is the basic speed on the lattice ($c = \Delta x / \Delta t$).

For a bth velocities and nth dimension model, the weighting factors and discrete velocities for the common DnQb model are listed as below.

D1Q3 (one dimensional, three velocity lattices):

$e_i = c\,[0, 1, -1]$, i=0, 1, 2.;

$c_s = \frac{c}{\sqrt{3}}$;

$$w_i = \begin{cases} 2/3 & c_i^2 = 0; \\ 1/6 & c_i^2 = c^2. \end{cases} ,i = 0,1,2.$$

D1Q5 (one dimensional, five velocity lattices):

$e_i = c\,[0, 1, -1, 2, -2]$, i=0, 1, 2, 3, 4.;

$c_s = c$;

$$w_i = \begin{cases} 1/2 & c_i^2 = 0; \\ 1/6 & c_i^2 = c^2; \\ 1/12 & c_i^2 = 4c^2. \end{cases} ,i = 0,1,2,3,4.$$

D2Q9 (two dimensional, nine velocity lattices):

$$e_i = c \begin{bmatrix} 0 & 1 & 0 & -1 & 0 & 1 & -1 & -1 & 1 \\ 0 & 0 & 1 & 0 & -1 & 1 & 1 & -1 & -1 \end{bmatrix} ,i = 0,1,2,3,4,5,6,7,8;$$

$c_s = \frac{c}{\sqrt{3}}$;

$$w_i = \begin{cases} 4/9 & c_i^2 = 0; \\ 1/9 & c_i^2 = c^2; \\ 1/36 & c_i^2 = 2c^2. \end{cases} ,i = 0,1,2,3,4,5,6,7,8.$$

D3Q15 (three dimensional, fifteen velocity lattices):

3.5. Governing equations of LBM multiple phase/component (MPMC) models
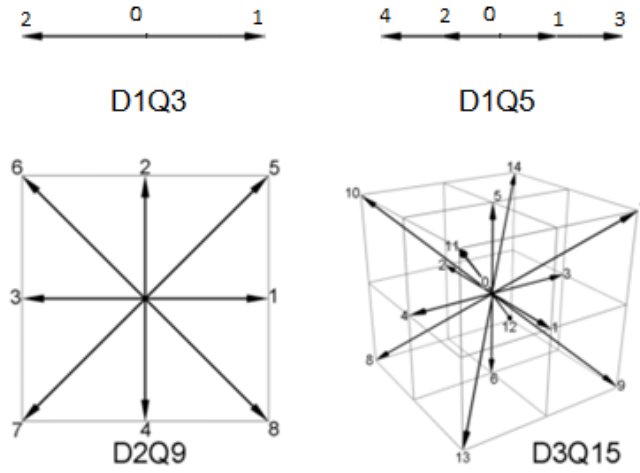
Figure 3.2: DnQb model for LBM. Top left: n=1 and b=3; Top right: n=1, b=5; Bottom left: n=2, b=9; Bottom right: n=3, b=15.

$$e_i = c \begin{bmatrix} 0 & 1 & -1 & 0 & 0 & 0 & 0 & 1 & -1 & 1 & -1 & 1 & -1 & -1 & 1 \\ 0 & 0 & 0 & 1 & -1 & 0 & 0 & 1 & -1 & 1 & -1 & -1 & 1 & 1 & -1 \\ 0 & 0 & 0 & 0 & 0 & 1 & -1 & 1 & -1 & -1 & 1 & 1 & -1 & 1 & -1 \end{bmatrix}.$$

$i = 0, 1, 2, 3, 4, 5, 6, 7, 8, 9, 10, 11, 12, 13, 14;$

$c_s = \frac{c}{\sqrt{3}};$

$$w_i = \begin{cases} 2/9 & c_i^2 = 0; \\ 1/9 & c_i^2 = c^2; \quad i = 0, 1, 2, 3, 4, 5, 6, 7, 8, 9, 10, 11, 12, 13, 14. \\ 1/72 & c_i^2 = 3c^2. \end{cases}$$

The distribution of the discrete velocities for each model is as shown in Figure 3.2.

The macroscopic density and velocity of each component are defined by

$$\rho_\sigma = \sum_i f_i^\sigma \tag{3.15}$$

$$u_\sigma = \frac{1}{\rho_\sigma} \sum_i f_i^\sigma e_i \tag{3.16}$$

The equilibrium velocity in Eq.3.14 is determined by the forces acting on the σth compo-

nent in the momentum equation, which is described by

$$u_\sigma^{eq} = u' + \frac{\tau_\sigma F_\sigma}{\rho_\sigma} \qquad (3.17)$$

where u' is the common velocity without the force, which is given by

$$u' = \frac{\sum_\sigma \sum_i f_i^\sigma e_i / \tau_\sigma}{\sum_\sigma \rho_\sigma / \tau_\sigma} \qquad (3.18)$$

where F_σ is the total force acting on the σth component.

In order to simulate multiphase or multicomponent fluids, the interaction forces are incorporated into the momentum equation, Eq.3.16. The forces cause the momentum (velocity) change in the equilibrium distribution function. The forces include the long range interparticle fluid-fluid interaction forces $F_{\sigma\bar\sigma}^f$, the fluid-solid surface force F_σ^s and external force such as gravity F_σ^g.

3.6 The forces for LBM MCMP models

3.6.1 The interparticle interaction

Fluid-fluid long range interparticle interaction forces include the fluid particle interaction within an identified fluid, which is the force described by non-ideal EOS, and that between fluids or components, which is defined as interfacial tension.

According to the suggestion from Shan-Chen [147], this interparticle interaction force $F_{\sigma\bar\sigma}^f$ can be simulated by

$$F_{\sigma\bar\sigma}^f = -\Psi^\sigma(x) \sum_\sigma G_{\sigma\bar\sigma}{(x,x')} \Psi^\sigma(x)\left(x'-x\right) \qquad (3.19)$$

where σ and $\bar\sigma$ indicate a pair of fluids or phases, ψ_σ and $\psi_{\bar\sigma}$ are the "effective mass", which are the function of density. $G_{\sigma\bar\sigma}$ is the Green's function to describe the interaction strength between two components, and $G_{\sigma\bar\sigma} = G_{\bar\sigma\sigma}$. Shan-Chen proposed that if only the interactions between nearest neighbors are considered, for D2Q9 model, $G_{\sigma\bar\sigma}$ can be

described by a symmetric matrix [147]

$$G_{\sigma\bar{\sigma}}(x,x^{'}) = \begin{cases} G_{\sigma\bar{\sigma}} & \left|x-x^{'}\right| = c \\ G_{\sigma\bar{\sigma}}/4 & \left|x-x^{'}\right| = \sqrt{2}c \\ 0 & otherwise \end{cases} \tag{3.20}$$

The interaction strength $G_{\sigma\sigma}$, $G_{\sigma\bar{\sigma}}$, $G_{\bar{\sigma}\sigma}$ and $G_{\bar{\sigma}\bar{\sigma}}$ correspond to the interaction forces of $F_{\sigma\sigma}^{f}$, $F_{\sigma\bar{\sigma}}^{f}$, $F_{\bar{\sigma}\sigma}^{f}$ and $F_{\bar{\sigma}\bar{\sigma}}^{f}$, respectively. $F_{\sigma\sigma}^{f}$ and $F_{\bar{\sigma}\bar{\sigma}}^{f}$ are related to the nonideal part of EOS for each component. The interfacial tension is determined by $F_{\sigma\bar{\sigma}}^{f}$ and $F_{\bar{\sigma}\sigma}^{f}$.

Equation of state (EOS)

In MCMP LBM, the intermolecular interaction, $F_{\sigma\sigma}^{f}$, is related to EOS. Shan-Chen (SC) [147] proposed the interaction force between particles of a real fluid and demonstrated it by simulation of the phase separation. The interaction force is defined by

$$F_{\sigma\sigma}(x) = -G_{\sigma\sigma}\psi(x)\nabla\psi(x) \tag{3.21}$$

where $G_{\sigma\sigma}$ is the interaction strength to control the interaction potential, which is related with the temperature. The positive and negative G represent the repulsive and attractive force, respectively. G=0 presents the ideal gas. The gradient part $\nabla\psi(x)$ can be evaluated by the nearest particles or extended to include the next-nearest particles.

Applying the interparticle interaction force as Eq.3.21, the EOS in LBM can be obtained as [172],

$$P = \rho RT + \frac{G_{\sigma\sigma}RT}{2}\left[\psi(\rho)\right]^{2} \tag{3.22}$$

If setting RT$= \frac{1}{3}$. it becomes,

$$P = \frac{\rho}{3} + \frac{G_{\sigma\sigma}}{6}\left[\psi(\rho)\right]^{2} \tag{3.23}$$

where the second term of Eq.3.23 is the non-ideal part, which is the particles interactions term. $\psi(\rho)$ as a function of density is the interaction potential. For simplicity, $\psi(\rho) = \rho$ [167]. Other forms of $\psi(\rho)$ were introduced, e.g. $\psi(\rho) = \rho_{o}\left[1 - exp\left(-\rho/\rho_{o}\right)\right]$ [147],
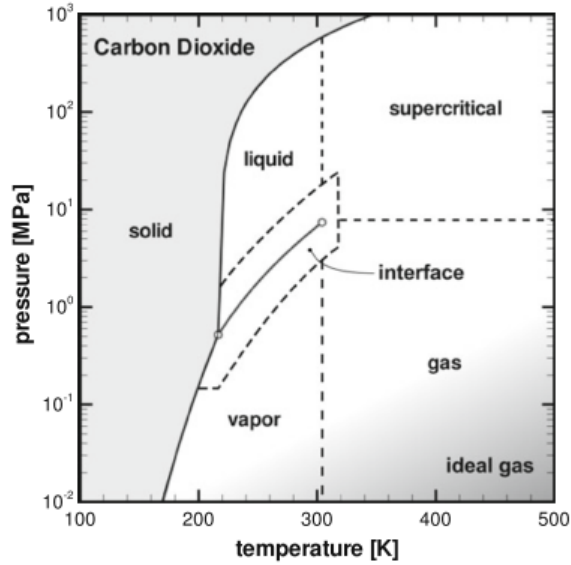
Figure 3.3: Carbon dioxide pressure-temperature phase diagram [17]

$\psi(\rho) = g\rho2_o\rho^2 / \left[2(\rho_o + \rho)^2 \right]$ [176]. However, for a real fluid, the accuracy EOS in LB is converted by the EOS in physical state.

EOSs of CO_2 and water

In physics, the first EOS was introduced by J.D. van der Waales in 1873 [177], and it performed better than the previous ideal gas law. Redlich-Kwong's EOS [178], proposed in 1949, is considered to be an improvement on the other equations, although error is apparent in the liquid phase. Kerrick et al. modified the Rehdlich-Kwong equation for H_2O, CO_2 and H_2O-CO_2 systems at a range of pressures ($\geq 1kb$) and temperatures (400-800°C) [179].

Huang et al. developed an EOS for carbon dioxide by using the quintic equation in a wide range of temperatures from 216 to 423 K and pressure up to 310.3 MPa [180]. Duan et al. [181] [182] proposed an EOS for H_2O, CO_2 and H_2O-CO_2 systems extending the pressure and temperature to 10 GPa and 2573.15 K, respectively, using a molecular level simulation with error less than 2%.

Bottcher et al. investigated four different EOSs, including Peng and Robinson (PR) [183], Duan et al. [181], and Span and Wagner [184] in the comparison with CO_2 density measurements, in terms of the vapour region, liquid region, interface region, gas region

3.6. The forces for LBM MCMP models

and supercritical region, as shown in Figure 3.3. Since the Span and Wagner's EOS achieved the best result but with iterations, it was concluded that PR EOS [183] as a cubic equation is the best option to describe the CO_2 properties, with regard to the simplicity and accuracy [17].

Based on the literature reviews, Yuan et al. [185] firstly incorporated the EOSs published in the physical state into the lattice Boltzmann simulation. Yuan et al. [185] investigated the merging of different representative EOSs into the multiple phase LBM simulation, in terms of spurious velocity, density ratio and temperature range. It was demonstrated that a realistic EOS obtains lower spurious velocity and develops a coexistence curve which matches the experimental data. On the other hand, the temperature was successfully introduced to the lattice Boltzmann simulation. A comparison of the simulation results of Shan-Chen, vdw, Redlich-Kwong, PR and Carnahan-Starling suggests that the PR EOS obtains the lowest spurious velocity and largest density ratio range, although the PR EOS was inaccurate regarding water density. Therefore, a realistic EOS is an important factor for the stability of a simulation.

Interfacial tension

Regarding the MCMP model, interparticle interaction forces are the forces which describe the interfacial tension between fluids. In the LBM, fluid-fluid interfacial tension is simulated by establishing a steady state droplet/ bubbles in another fluid. To simulate interfacial tension, other forces such as buoyancy are all excluded. With regard to a steady state droplet/bubble, the Laplace-law $((\Delta P = \sigma/R)$) can be applied and the interfacial tension in LBM can be identified by the changes in droplet/bubble size with a given pressure difference.

In this study, interfacial tension is predicted by setting a steady state droplet in the centre of simulation domain filled with another fluid. The 2D simulation in a 300×300 lattices LBM domain is performed by setting $G_{11}=G_{22}=0.0$ and $G_{12}=G_{21}=0.1$ by giving the initial droplet size R. The periodic boundary conditions are applied on both of x and y directions. The pressure of each fluid is calculated by Eq.3.23.

The results of ΔP and R when the simulations reach to the steady state are illustrated in
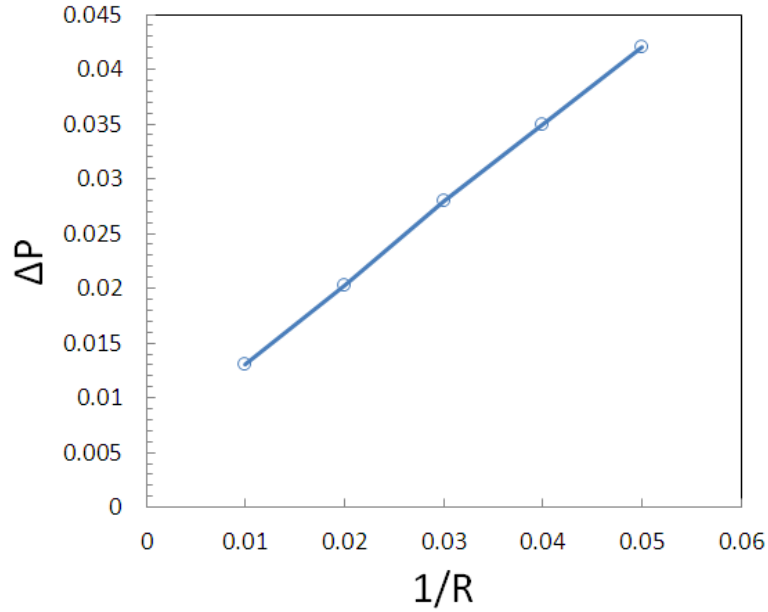
Figure 3.4: The test of Laplace's Law for multicomponent model

Figure 3.4. With a series of initial radius, in the steady-state, the difference of the pressure inside and outside droplet is linear with the reciprocal of the radius, as shown in Figure 3.4. It satisfies the Laplace's Law ($\Delta P = \sigma/R$). The surface tension (σ) is 0.7625 in LB unit.

It must be noted that the interparticle forces proposed by Shan-Chen generate the unphysical numerical diffusion. To identify this unphysical numerical diffusion, the static droplet/bubble simulation is applied to illustrate this numerical diffusion effect. This unphysical numerical diffusion produces some unphysical results to transfer the particles within two fluids.

The simulation is carried out in a 200×200 simulation domain. The initial density ratio of two components is set be 1.0. The relaxation times are 0.5546 and 1.0, respectively, which are converted from the viscosities of CO_2 and water in physics. To be simple, $G_{11} = G_{22}$ is set to be 0.0. The density distributions are obtained under a series of interaction strength G_{12} (G_{21}).

Figure 3.5 shows the density distribution along the central section (y=100), under the interaction strength $G_{12} = 2.4$. It shows that there is not pure single fluid region. The fluid penetrates into each other. This is the result due to the numerical diffusion.
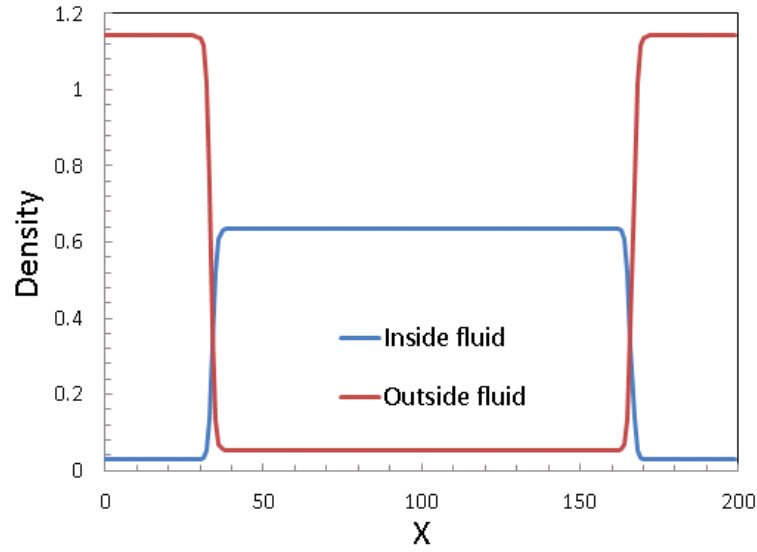
Figure 3.5: The fluid distribution demonstrated by density along x-axis in the middle of y direction, y=100.

It is found that the numerical diffusion is related with the interaction strength G_{12}. To illustrate the numerical diffusion, a density ratio of ρ_{ND}/ρ is defined in this study. ρ_{ND} and ρ are the droplet density in the surrounding fluid produced by the numerical diffusion and the density of the droplet, respectively. As shown in Figure 3.6, the numerical diffusion reduces with the increase of G_{12}. In this case, the critical interaction strength G_{12} is 3.15. Larger than the critical interaction strength, the unphysical negative numerical diffusion density occurs. It means an unphysical mass source generated.

It is concluded that G_{12} should be chosen at the point that generates the minimum numerical diffusion, which can be obtained by the curve interpolation, as shown in Figure 3.6. The selection of G_{12} should be based on two criteria. Firstly, the positive numerical diffusion should be as small as possible. Secondly, the spurious velocity at the fluid-fluid interface should be as low as possible, since the spurious velocity is related to the simulation stability and difficult to distinguish from the real velocity on the interface between components.
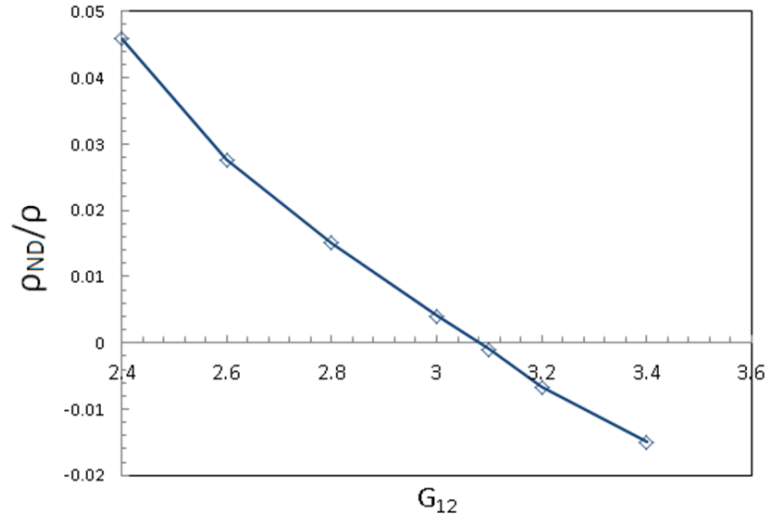
Figure 3.6: The numerical diffusion varies with G_{12}

3.6.2 The fluid/solid surface interaction force

In the CO_2 geological storage site, the sediments are composed of different substances. Therefore, the interaction between the sediment and fluid is another factor which should be considered during storage. In the LBM, the interaction between solid and fluid is controlled by the fluid-solid surface force, which is given by

$$F_\sigma^s = G_{ads}\Psi_\sigma \sum_i w_i s\left(x + e_i\Delta t\right) e_i \tag{3.24}$$

where $s(x + e_i\Delta t)$ is used to distinguish the fluid and solid particle. $s(x + e_i\Delta t) = 1$ as solid is at the node of $x + e_i\Delta t$. Otherwise, $s(x + e_i\Delta t) = 0$. The coefficient G_{ads} describes the interaction strength between the solid and fluid. This fluid-solid surface force provides the options of LBM in simulation various solid wall in a channel or a porous media.

The fluid/solid surface force is validated by the simulation of multicomponent fluids flow in the channel. The simulation is carried out in a 100×300 lattices domain and density ratio is set to be 10. Fluid One with the size of 100×100 lattices is located in the channel, which is filled with Fluid Two. The densities of the injected fluid (Fluid One) and displaced fluid (Fluid Two) are 0.1 and 1.0, respectively. The interparticles potential G_{12} is set to be 1.8, which is based on the minimal numerical diffusion criterion discussed in Section 3.6.1. The surface adhesion parameters of two fluid are G_{ads1} and

3.6. The forces for LBM MCMP models

θ	70°	60°	45°	0°	135°	150°	160°	170°
G_{ads1}	0.0	0.0	0.0	0.0	0.9	1.27	1.56	1.8
G_{ads2}	1.56	1.27	0.9	0.0	0.0	0.0	0.0	0.0

Figure 3.7: Simulation results of the contact angle varying with the adjusting of the surface adhesion parameter.
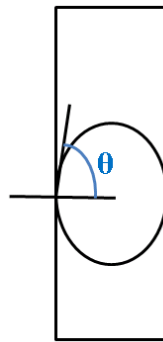
Figure 3.8: Illustration of the definition of the contact angle

G_{ads2}, respectively.

A series of LB simulation with different G_{ads1} and G_{ads1} are carried out to obtain different contact angles. Figure 3.7 shows that the desired contact angle on the solid/liquid surface can be adjusted by the surface adhesion parameter G_{ads}. The contact angle is defined as shown in Figure 3.8. The relationship between the contact angle and the surface adhesion parameter is achieved. It presents that the contact angle is linearly increasing with the increase of G_{ads1} (see Figure 3.9) and linearly reducing with the increase of G_{ads2} (see Figure 3.10). As $G_{ads1}=G_{ads2}=0.0$, the contact angle is 90°. As $G_{ads1}>G_{ads2}$, the contact angle is obtuse, that means the wetting ability of Fluid Two is larger than that of Fluid One. Otherwise, the contact is acute, that means the wetting ability of Fluid Two is smaller than that of Fluid One.
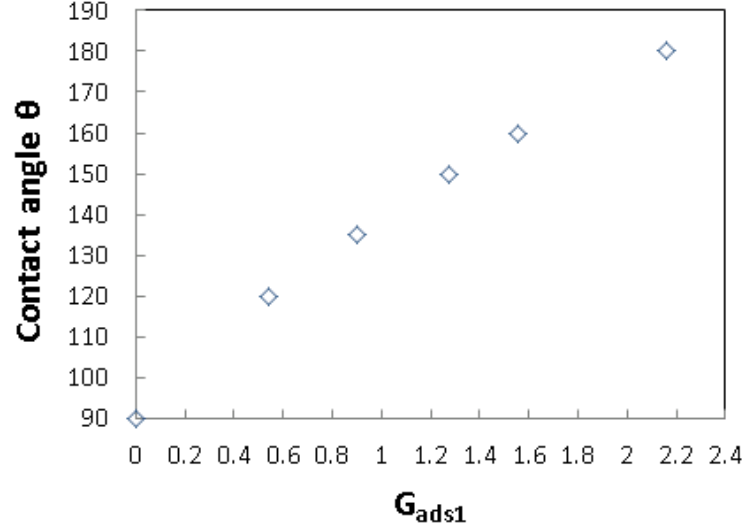
Figure 3.9: The contact angle changes with the surface adhesion parameter G_{ads1}

3.6.3 The gravity force

The gravity force is the external force, which is given by

$$F_{\sigma}^{g} = \rho^{\sigma} g = m^{\sigma} n^{\sigma} g \tag{3.25}$$

where g is the gravitational acceleration in LB unit, m^{σ} and n^{σ} are the molecular mass and number density, respectively. The buoyancy force is the net force of the gravity force for each fluid, defined as $F_{\sigma}^{g} - F_{\bar{\sigma}}^{g}$.

The gravity force is validated by the free CO_2 bubble rising up simulation. A series of bubble diameters are set up to get different Re numbers. The simulation results at Re=8.6 and Re=43 are presented in Figure 3.11 and Figure 3.12, respectively. It shows that the CO_2 bubble shape is spherical at Re=8.6 and deformed to an oblate ellipse at Re=43. The simulation results of the bubble shapes get a good agreement with the study of Gupta et al. [186].

In addition, the CO_2 bubble rising up simulations are carried out to compare with the experimental results [18] at T=307.65 K and P=9.2 MPa, in terms of the rising velocity. Initially, the CO_2 bubble is set at the bottom of the channel, which is filled with water. As the density of CO_2 bubble is smaller than that of surrounding water. The bubble is driven up by the buoyancy force. The simulation condition is based on the experimental

3.6. The forces for LBM MCMP models
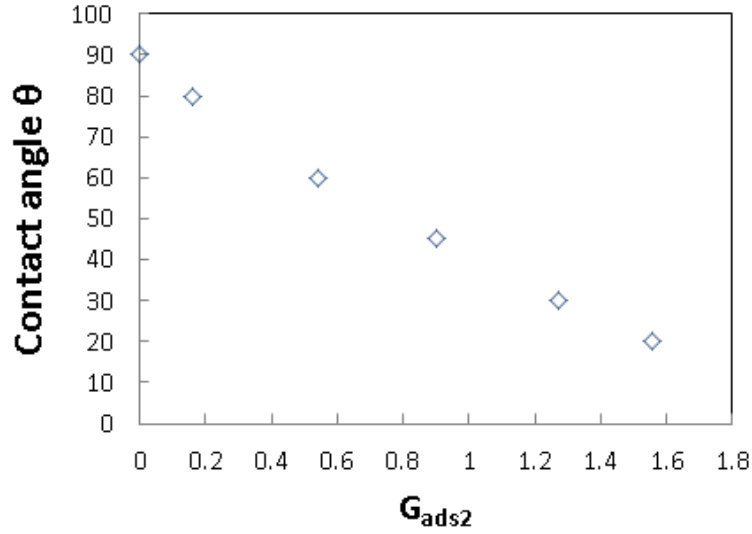
Figure 3.10: The contact angle changes with the surface adhesion parameter G_{ads2}

Table 3.1: The parameters for the rising up bubble simulation

	Experiment	LB
Temperature(K)	307.65	-
Pressure(MPa)	9.2	-
Phase of CO_2	Supercritical	Supercritical
Radius(mm)	0.23	23
Density of $CO_2(kg/m^3)$	684.57	0.68457
Density of water(kg/m^3)	998.2	0.9982
viscosity of $CO_2(m^2/s)$	7.89E-08	0.128
viscosity of water(m^2/s)	7.28E-07	0.266
gravity(m^2/s)	9.81	0.000713

data [18]. The initial parameters in the LBM simulation are illustrated in Table3.1.

Figure 3.13 shows the rising velocity varies with time. It shows that the simulation results of the terminal velocity (the velocity reaching to the steady state) reasonably agree with experimental data in these two cases [18]. The velocity error ((u_{LB}-u_{Exp})/u_{Exp}) are 6.66% and 22.3%, respectively.
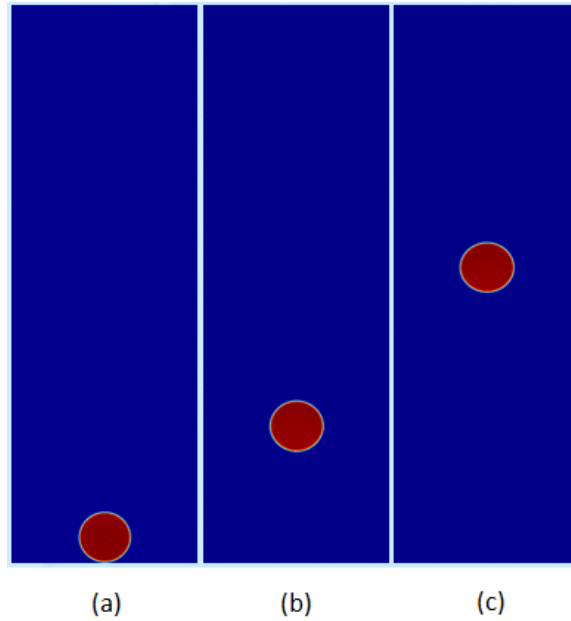
Figure 3.11: Free rising droplets predicted by LBM model at Re=8.6 at different time steps, (a) t=0; (b) t=8400 and (c) t=21200.

3.7 Boundary conditions

In the LBM, the nodes on the boundary are relatively more complex than the bulk nodes, because some distributions of its neighbor nodes are unknown after the streaming process. The boundary condition is required to determine the unknown distributions. Therefore, choosing appropriate boundary conditions in the simulation process is necessary for meaningful results, not only because of accuracy but also with regard to the stability of the simulation.

Various non-slip boundary conditions have been developed since the early 1990s [187] [188] [189] [190] [191] [192] [193] [194]. The accuracy of the boundary conditions is investigated by comparing the analytical solutions of Poiseuille and Couette flows [195]. The non-slip boundary condition enables the implementation of LBM in porous media. In order to be applicable in many types of simulations, the boundary conditions continue to be developed in terms of temporal and spatial extension [193] [149] [190]; for example, simulation of realistic porous media is enabled [196].

In this section, the boundary conditions used in this study are introduced, including the periodic boundary condition, bounce-back boundary condition and Zou-He pressure and
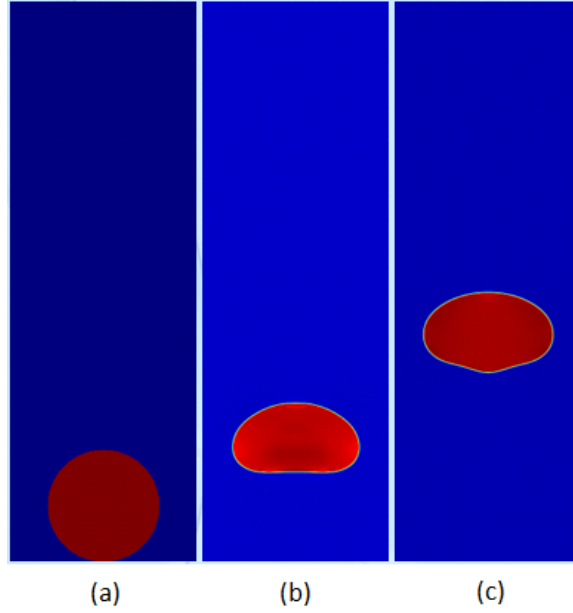
Figure 3.12: Free rising droplets predicted by LBM model at Re=43 at different time steps, (a) t=0; (b) t=4700 and (c) t=9700.

velocity boundary condition.

3.7.1 Periodic Boundary Condition

The periodic boundary is one of the common conditions for the infinite domain and closed edge, in which the system is regarded as a closed one by the edges, as if inlet and outlet edges are joined to each other. In the simulation process, the nodes of the unknown distributions on the boundary, whose neighboring points are on the opposite boundary, are assigned by the opposite point of achieving periodicity. For example, the periodic boundary condition in x direction is shown in Figure 3.14 and achieved as Eq.3.26

$$f[j][0][1] = f[j][N][1];$$
$$f[j][0][5] = f[j][N][5];$$
$$f[j][0][8] = f[j][N][8];$$
$$f[j][N][3] = f[j][0][3];$$
$$f[j][N][6] = f[j][0][6];$$
$$f[j][N][7] = f[j][0][7]; \qquad (3.26)$$
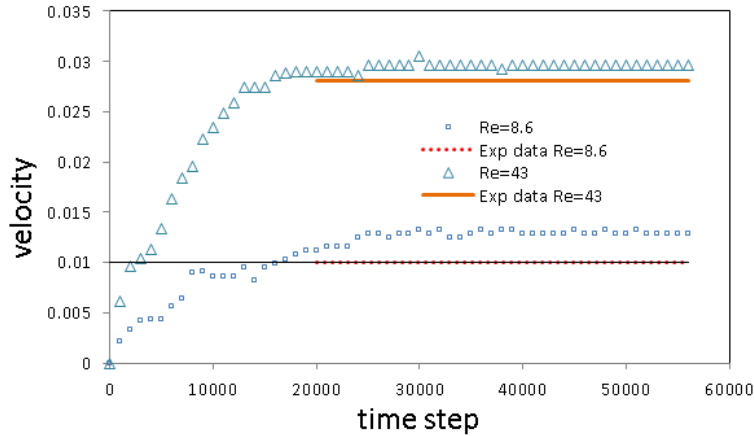
Figure 3.13: The simulations of rising velocity varies with simulation time step, in comparison with the experimental data [18] at Re number of 8.6 and 43

3.7.2 Bounceback Boundary Condition

Bounceback boundary condition has been proposed to achieve a non-slip velocity boundary condition. This means that as the particle collides with the wall nodes, it will bounce back in the opposite direction. Bounceback boundaries are very convenience methods of simulating the fluids in complex geometries, including porous media.

Complex geometries are constructed of the solid nodes. All the solid nodes are categorized into two classes. One is the boundary solids which are between the solid and fluids, which have direct contact with the fluid nodes, namely interface nodes. The other type is the isolated solid that is far from the fluid and surrounded by the solid nodes. Only the interface nodes communicate the distributions with the fluid nodes on each time step. Meanwhile, the isolated solid nodes ignore collide and stream with the benefit of saving unnecessary computational consumption.

Several bounceback boundary conditions have been developed to achieve a non-slip boundary condition [187] [197] [189] [198] [190] [191] [193]. Comparisons between various boundary conditions are conducted and the accuracy of each scheme is illustrated [195]. In general, the methods are divided into two types; one is a full-way bounce-back in which the boundary is on the nodes [198] [189], while the other is a half-way bounce-back boundary with a boundary between the nodes [199] [196]. It is generally accepted that the full-way bounceback boundary condition is of first-order accuracy, while the half-way bounceback boundary condition is of second order [195].
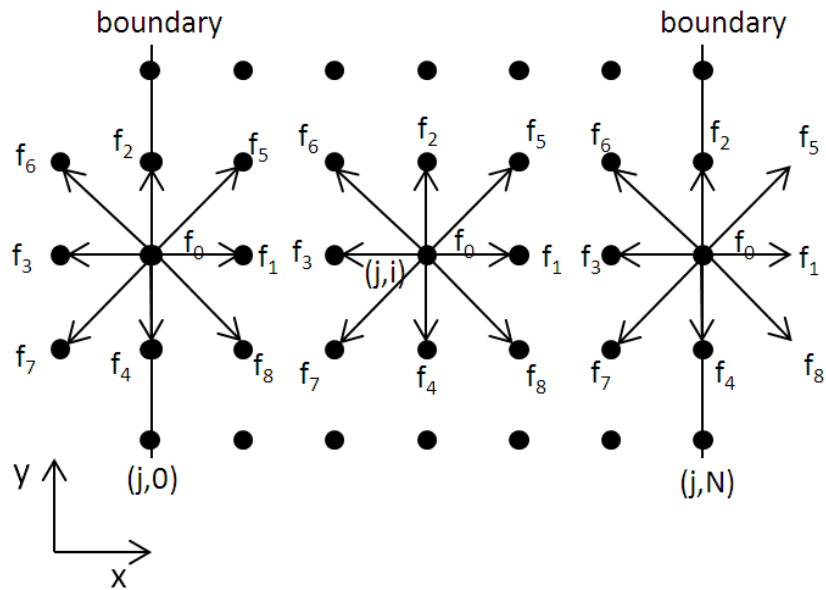
Figure 3.14: Illustration of periodic boundary condition.
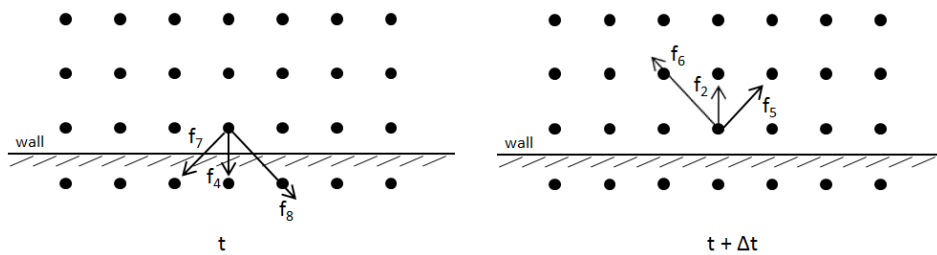
Figure 3.15: Illustration of bounceback boundary condition.

In the full-way bounce-back scheme, the boundary nodes change the usual collision step and keep the usual streaming step. In the specialized collision step, all populations of the particles next to the wall are replaced by the value of their own populations in the opposite direction. The error is found in the implementation of the poiseuille flow simulation [198] [189].

The half-way bounce-back approach unlike the full-way bounce-back approach in which all the populations are opposite, in the half-way bounce-back approach only unknown particle populations are copied. Figure 3.15 illustrates the scheme of a half-way bounce-back boundary condition. The solid nodes are arranged outside the wall. At the time step t, the post-stream value of solid populations are assigned in the opposite direction, followed by the usual collision step and then streamed back to the fluid domain. In comparison with

the full-way bounce-back boundary condition, the primary characteristic of this scheme is modification of the streaming step and keeping the collision step. In the case of the D2Q9 model, the simulation code performs on a node as can be seen below,

$$ftemp = f[j][i][1]; f[j][i][1] = f[j][i][3]; f[j][i][3] = ftemp;$$

$$ftemp = f[j][i][2]; f[j][i][2] = f[j][i][4]; f[j][i][4] = ftemp;$$

$$ftemp = f[j][i][5]; f[j][i][5] = f[j][i][7]; f[j][i][7] = ftemp;$$

$$ftemp = f[j][i][6]; f[j][i][6] = f[j][i][8]; f[j][i][8] = ftemp; \tag{3.27}$$

where $ftemp$ is a temporary variable.

3.7.3 Pressure/Velocity Boundary Condition

In the fluid flow application, the fluid is often driven by the pressure difference or kept in a constant velocity. The implementation of the pressure/velocity boundary condition in the LBM is necessary.

The method used to control the pressure or velocity on the boundary is variation [188] [191] [200]. Skordos [188] proposed a method for calculating the boundary nodes by extending the collision operator based on the velocity gradients, which is only validated in D2Q7. Inamuro [189] proposed a new method to determine the unknown distribution functions by additional constant term. Maier [191] achieved pressure boundary condition by means of an extrapolation scheme which is completely different from the bounceback boundary condition. Zou and He [200] proposed the scheme by the bounceback assumption of non-equilibrium part. For example, $f_i - f_i^{eq} = f_j - f_j^{eq}$, i and j indicate the opposite direction. Recently, Zou-He boundary condition has been widely used in the applications of pressure/velocity boundaries [14] [15] [201]. In this study, Zou-He boundary condition is applied in the simulations.

3.8   Challenges of LBM MCMP models

The LBM MCMP models have been developed and applied in the simulation of fluids flow in complex geometry. However, LBM is still restricted in some requirements, such as the high March number flow, large density ratio, unphysical "spurious velocity".

It has been noted that high-Mach numbers limitation, know as Ma«1, comes from the original LBM assumption. It is still a challenge for the traditional LBM to deal with high-Mach number flows, despite the ongoing methods proposed to relax the limit [202] [145] [203] [204].

In recent years, the LBM MCMP stability is concerned and discussed by the researchers [205] [1] [206]. It has been found that large density ratio of MCMP simulation is restricted by the simulation stability, which is related to "spurious velocity".

The spurious velocity was first discussed by Gunstensen in 1992 [139], which is an unphysical small flow near the interface of two phases/component. The methods used to reduce the spurious velocity and increase the density ratio can be classified into three ways. Several numerical schemes have been developed for the solution of the lattice Boltzmann equation, in terms of the collision operator and the discretization of the stream part [1]. It has been demonstrated that the numerical difficulties, especially the stability, is related with the collision operator, rather than the stream term [1]. Therefore, one way is to improve the scheme for the collision operator [1] [206] [173]. The second way is to discrete density gradient operator in the interparticel interaction force [207]. The third way is to incorporate an accuracy pseudipotential model to describe the pressure [185] [208].

In 2002, Nourgaliev et al. assessed the spurious velocity by the implicit lattice Boltzmann method [1]. The implicit trapezoidal method is with second-order accurate, is considered as a stable scheme by the linear stability analysis [209] [173]. In the implicit model, both of the local and next time step's equilibrium distributions are used to calibrate the collision operator, and the collision operator is evaluated by a trapezoidal rule using the central difference approximation. This method is successfully applied in multiphase simulations and expands the range of Eo and Mo value in the multiphase flow calculations

[210]. It significantly minimized the spurious velocity across the interface in the order of magnitude in comparison with Shan-Chen model. However, the simulation is achieved by the iterations. Even though it converges rapidly, this implicit method apparently increases the CPU time consumption per simulation step due to the iteration calculation [206] [173].

In 2006, Shan indicated that the spurious velocity on a curved interface is resulted from the lowly isotropic discrete density gradient operator [207]. He proposed a high-order isotropic gradient operator and effectively reduced the spurious current in terms of the magnitude and the spatial extent. In the 100×100 lattices simulation domain, the spurious velocity significantly reduces about 3 times as the order of the density gradient increases from three to eight order.

In 2006, Yuan et al. successfully reduced the spurious velocity by using the different equation of states [185]. He proposed that lattice Boltzmann method with Peng and Robinson equation of state sharply decreased the spurious velocity in comparison with the Shan-Chen equation of state, and apparently extends the density ratio range in the multiple phase simulations.

In 2007, Sbragaglia et al. [208] developed another extended pseudopotential method to minimize the spurious velocity by extending the spatial range of the interaction. The spurious velocity is multiply reduced.

3.9   LB unit

LBM simulations resolve the real physical system with the use of "LB variables". The choice of "LB variables" is restricted by the law of similarity. First, the LB simulation must be equivalent to the real physical problem, such as the parameters being related to each other by the same dimensionless number. Second, in order to satisfy simulation stability and accuracy, the discrete parameters are restricted, such as the sufficient resolution and discrete time step [211].

The LBM is a discretization method to recover Boltzmann equation, in which the parameters are the discretization of the macroscopic variables. Unit conversion should be provided in order to achieve a desirable result. In general, the dimensionless value in

Table 3.2: LB unit conversion

	conversion	physical value	LB variable
velocity	$u_{lb} = u_p \times \frac{\zeta_t}{\zeta_x}$	2 mm/s	0.01
viscosity	$v_{lb} = v_p \times \frac{\zeta_t}{\zeta_x^2}$	$2\ mm^2/s$	1/3
density	$\rho_{lb} = \rho_p \times \frac{\zeta_x^3}{\zeta_{kg}}$	$1000\ kg/m^3$	1
gravity acceleration	$g_{lb} = g_p \times \frac{\zeta_t^2}{\zeta_x}$	$9.8\ m/s^2$	0.00735

LBM is equal to the physical quantity divided by the conversion factor. Three independent primary conversion factors are required in incompressible fluid flow simulation, including the factors of length conversion ζ_x, time conversation ζ_t and density conversion ζ_ρ or mass conversion ζ_{kg}.

For example, the 2D fluid flow is constructed in the 3mm×3mm domain, and the inlet velocity is 2 mm/s. The viscosity and density of the fluid are $2mm^2/s$ and $1000\ kg/m^3$, respectively. The LBM simulation is consisted of 100×100 lattices. Therefore, the length conversion factor is $\zeta_x = L/N = 3 \times 10^{-3}/100 = 3 \times 10^{-5}$. To be simply, the density is chosen by 1 in the LBM. The density conversation factor is $\zeta_\rho = \rho_p/\rho_{lb} = 1000/1 = 1000$. Furthermore, the mass conversation factor is described by $\zeta_{kg} = \zeta_\rho * \zeta_x^3 = 1000 \times \left(3 \times 10^{-5}\right)^3 = 2.7 \times 10^{-11}$.

The choice of discrete time is related to the simulation stability, therefore it needs to be fine-tuned. The discrete time is linked to the discrete length by the constraint $\delta_t \approx \delta_x^2$ [211], where $\delta_x = \zeta_x/L = 1/N$, $\delta_t = \zeta_t/t_0$, t_0 is characteristic time, in this case, $t_0 = L/u_p = 3/2 = 1.5s$. Therefore, $\delta_t \approx 10^{-4}$ and $\zeta_t = 1.5 \times 10^{-4}$, respectively. The basic conversion rule is summarized in Table.3.2

3.10   Reviews of mass transfer models of MCMP LBM

In this study, the LBM is used to build up the multicomponent model to simulate mass transfer at pore scale. In this section the applications of LBM in MPMC fluids flow are reviewed, in particular the applications of the LBM in mass transfer.

3.10.1 Mass transfer on fluid/fluid interface

The LBM for miscible flow mixture has been investigated since the 1990s. Holme and Rothman [212] proposed the first LGA model to simulate miscible flow mixture in two-dimension. Lower diffusivity is achieved by the nonlocal interaction. In 1993, Flekkoy [213] following the idea of Holme and Rothman developed a two component miscible fluids LBGK model for mass transfer in both two-dimension and three-dimension. It assumes that the collision between two components is negligible. The scheme is described by

$$N_i(x+c_i,t+1) = N_i(x,t) + \lambda_v N_i^{neq}(x,t) \tag{3.28}$$

$$\Delta_i(x+c_i,t+1) = \Delta_i(x,t) + \lambda_\Delta \Delta_i^{neq}(x,t) \tag{3.29}$$

where

$$N_i = Ri + B_i \tag{3.30}$$

$$\Delta_i = Ri - B_i \tag{3.31}$$

$$N_i^{neq} = t_i \rho \left(1 + \frac{c_i u}{c_s^2} + G Q_{i\alpha\beta} u_\alpha u_\beta \right) \tag{3.32}$$

$$\Delta_i^{neq} = t_i \Delta \rho \left(1 + \frac{c_i u}{c_s^2} \right) \tag{3.33}$$

where R_i and B_i are the mean occupation number of red and blue particles. c_s is speed of sound. G is a constant, such as G=4.5 for BGK model, and determined by the convection term. Δ_i is the gradient. The relaxation times λ_v and λ_Δ are determined by the kinematic viscosity and diffusion coefficient, respectively. c_i is the velocity vector. $Q_{i\alpha\beta} = c_{i\alpha}c_{i\beta} - c_s^2 \delta_{\alpha\beta}$ is the tensor. The high Péclet number flow was investigated in their study. The Péclet number is defined as the ratio of advective transport rate to diffusive transport rate. It has been found that the diffusion coefficient obtained by the simulation is close to the theoretical value, as the diffusion coefficient is greater than 10^{-4}.

Stockman et al. [19] developed a LBM dispersion model by introducing a set of functions for the tracer. The distribution function of tracer has fewer vectors than that of the carrier
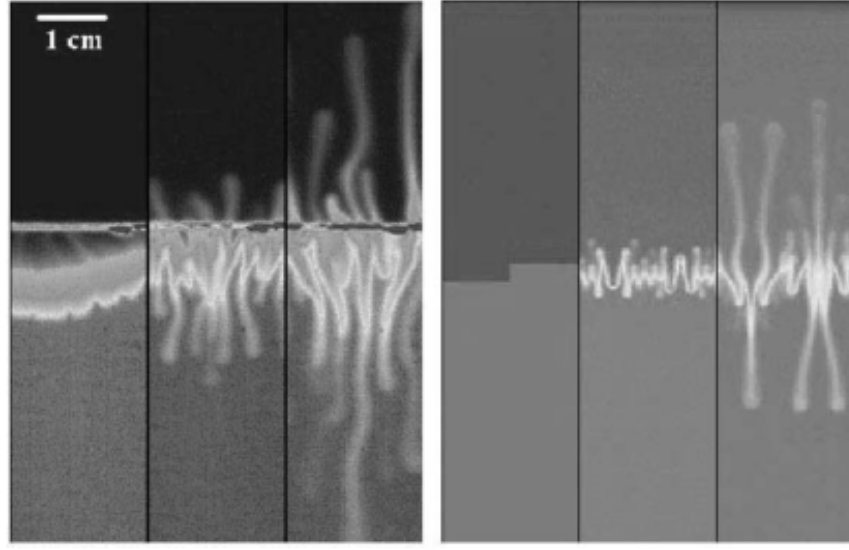
Figure 3.16: Double-diffusive fingering in cell. Left: experimental results. Right: 2D LBM simulation results [19].

fluid. The equilibrium functions for the carrier fluid and the tracer are defined by

$$f_0^{eq} = \frac{\rho}{3} \left[1 - \frac{3}{2} u^2 \right] \tag{3.34}$$

$$f_i^{eq} = t_i \rho \left[1 + 3 e_i \cdot u + \frac{3}{2} \left(3 e_i e_i : uu - u^2 \right) \right] \tag{3.35}$$

and

$$f_{s,i}^{eq} = A + B \left(e_{s,i} \cdot u \right) \tag{3.36}$$

where the subscript "s" denotes the solute. A and B are determined by the solute conservation, known as $\rho_s = \sum f_{s,i}^{eq}$ and $\rho_s \cdot u = \sum f_{s,i}^{eq} e_{s,i}$. This LBM dispersion model is used in the investigation of the double-diffusive fingering. It has been found that the rate of finger growth by LBM simulation is smaller than that in the experiment, as shown in Figure 3.16.

In 1997, Noble [214] developed a 2D LBM to simulate the advection-diffusion fluids flow by an additional four-velocity equilibrium distribution for mass transfer. The equilibrium

distribution function is defined by

$$f_i^{eq} = C \left(\frac{1}{4} + \frac{1}{2c^2} \left(e_i \cdot u \right) \right) \tag{3.37}$$

where C is the solute concentration. The relaxation time in the collision term is determined by the diffusion coefficient.

Knutson [215] used Noble's model to discuss the dissolution in porous media with variable distribution of nonaqueous phase liquid blobs. In the simulation, the porous media was designed by the orderly arrangement of the circle solid grains. The effect of blob configuration and the *Pe* number on the mass transfer were investigated.

In 2002, Inamuro and Yoshino [216] proposed a LBM model for convection-diffusion in two miscible fluid mixtures. This 15-velocity model assumed that the fraction of component B is smaller in comparison with the fraction of component A. Therefore, B-B and A-B collisions are neglected in comparison with B-A and A-A collisions, respectively. The equilibrium distribution function of B is as normal, while the equilibrium distribution function of B only contains two terms, which are up to first order in the flow velocity. The mass diffusivity is related to the relaxation time of component B. The small Knudsen number is a matter of concern in the study. The ability of the model in the thermal fluid system is demonstrated by the simulation of the diffusion between two parallel walls and Rayleigh-Benard convection. The component B is regarded as the temperature distribution of component A. In 2003, Yoshino and Inamuro [149] applied the mass transfer model in porous media, assuming the diffusion fraction is negligible. The mass transfer for miscible fluid in porous media is calculated in a series of Reynolds numbers. It indicates the ability of the LBM in the simulation of mass transfer in simple porous media.

Apart from these, Merks et al. [217] validated the LBM moment propagation method by the simulation of advection-diffusion. In the moment propagation method, a scalar quantity as the dispersion of tracer is started after the stream and collision step. A fraction of the scalar quantity is redistributed according to probability. Zhang et al. [218] proposed a LBM model for advection and anisotropic dispersion. The particle speed space is discretized by the rectangular lattices with 4-velocity in 9 directions, instead of the common square 3-velocity in 9 directions. The relaxation time is dependent on the directions. The
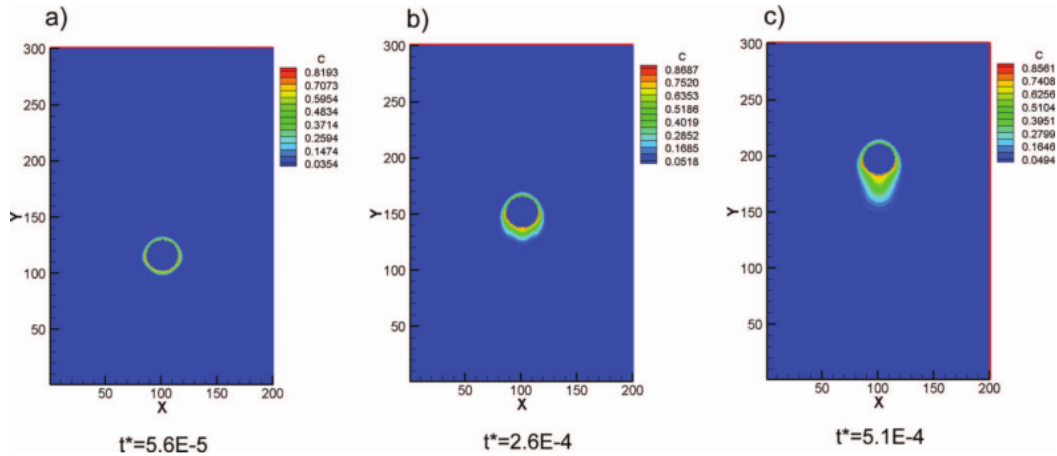
Figure 3.17: Dissolution of single droplet rising up at Eo=0.4428 [20].

mass is calculated by the weighted sum of distribution function; it is no longer the sum of the distribution functions. The concentration is obtained from the particle distribution functions. The benchmark study showed that the model was accurate and efficient in the simulation of dispersion and advection problems.

In 2009, Chen et al. [20] applied Kang et al.'s [219] LBM model to investigate the dissolution of a single droplet rising up. A four-velocity equilibrium distribution function was introduced to describe the mass transfer. The boundary condition proposed by Kang et al. [125] was used to control the diffusion. The simulations assumed that the interface motion resulting from the dissolution is slow and that the droplet interface is not moving. The concentration distribution of the droplet was obtained, as shown in Figure 3.17. The accumulated mass on the bottom side of the droplet was observed. In addition, the dissolution of multiple droplets was investigated by this LBM model.

3.10.2 Reaction flow

The LBM for reaction flow has been developed since the 1990s. Kingdon et al. [220] proposed the first two dimension lattice Boltzmann model for the reaction-flow in two dimensions. The model is carried out on the assumption that reactant is sufficiently dilute. Therefore the interface effect, heat and mass effect are negligible. The chemical reaction was achieved by introducing a source term to the concentration distribution. The diffusivity is related to the relaxation time of the solute in the collision operator. Similar models

are investigated with regard to nonlinear reaction by Weimar and Boon [221].

In 1993, Dawson et al. [222] developed a two-dimensional reaction-diffusion model. The collision operator was defined by reactive terms and nonreactive terms. Quantitative agreement was obtained in a comparison study between this model and theoretical prediction in pure diffusion phenomena and Turing patterns. In addition, Qian et al. [223] proposed a lattice Boltzmann model for the diffusion-driven irreversible chemical reaction. The results show that this model achieves a better result than the cellular automaton model.

3.10.3 Mass transfer on solid/fluid interface

The lattice Boltzmann method for mass transfer on a solid/liquid interface was generated from the cellular automaton model proposed by Wells et al. [224]. The chemical reactions at mineral surfaces were simulated. The mass transfer is controlled by a probability function describing the disequilibrium between the mineral and fluid. The wall node converts to the liquid node based on the dissolution condition.

In 2000, He et al. [225] proposed the first LBM for a surface chemical reaction, which successfully avoids the intrinsic noise in lattice gas automaton. This model assumed the dilute solute, which has no effect on solvent flow. Two distribution functions were implemented to describe the solvent and concentration of solute. The chemical reaction for the fluid is represented by a source term following the collision term. The boundary condition for the diffusion at the macroscopic level successfully converts to the LBM. This approach stems from observation and the non-equilibrium part of the distribution function is related to microscopic velocity and concentration gradient. The simulations results at the steady state confirmed those achieved with the Leveque solution, with the exception of the inlet corner.

In 2002, Kang et al. [125] extended He's model to study chemical reactions in porous media. The boundary condition of the solid wall is similar with He's model to describe the surface reaction. The dissolution of carbonate rocks in HCL and HAc was investigated by the proposed LBM model. The simulation results achieved a qualitative agreement with the experimental results.

3.10. Reviews of mass transfer models of MCMP LBM

In 2003, Kang et al. [132] continued their work to incorporate the precipitation into the dissolution model in a simplified porous medium. The effects of dimensionless parameters (Pe and PeDa number) on the transfer and reaction process were investigated. It was concluded that dissolution and precipitation were complex, even though a simplified geometry was used. Afterwards, Kang et al. [226] presented the Lattice Boltzmann model of multiple aqueous components in porous media taking into account homogeneous and heterogeneous reactions. The homogeneous reactions were based on the local equilibrium mass relation. The mineral reaction was achieved through the boundary condition on the solid surface.

In 2007, Kang et al. [124] further improved the multicomponent reaction model in porous media through implementation of a rigorous derived boundary condition, instead of the thermal boundary condition for mass transfer. The improved boundary condition was derived by the correcting expression of the distribution function. The simulation results showed that the models with the improved boundary condition got better agreement with analytical results, in comparison with the results of the previous boundary condition. Furthermore, the model was utilized in both of D2Q9 and D2Q4 simulations. It was concluded that D2Q4 model is more efficient than the D2Q9 model.

In 2011, Parmigiani et al. [15] used the SC multiphase multicomponent model coupled with Nobel's diffusion model to investigate the mass and reactant transfer in porous media with uniform and random particles. The advection-diffusion process was described by an additional distribution function. Non-wetting fluid was injected into the saturated porous media. The two fluids phases were immiscible. The study only focused on solid melting, which is not suitable for moving solid-fluid boundary cases.

In 2013, Chen et al. [129] combined the single component multiple phase SC model, mass transfer model [227] and Kang's dissolution-precipitation to model thermal driven migration of a brined inclusion in a salt crystal. A concentration boundary was proposed to handle the moving reactive boundary. The mass transfer model was achieved by adding a source term related to the homogeneous reactions after the collision operator. The diffusivity was controlled not only by the relaxation time, but also by adjusting the defined parameter in the equilibrium distribution function of the concentration. It successfully

investigated the physiochemical processes including the phase transition, heat transfer, solid dissolution and precipitation.

3.10.4 Summary

Therefore, recent research efforts in mass transfer are classified into three different methods. (*i*) The model preserves the normal MCMP to simulate the diffusion by reducing the interaction force between different fluids. (*ii*) The second component is modified by a separate distribution function to simulate the solute concentration. It is regarded as the passive solute model. (*iii*) A special boundary condition is applied on the interface between fluid and solid to model the mass transfer.

(*i*)Active Solute Model [228]. This method preserves the normal MCMP model with the complementary density for the binary fluids. Shan and Chen [228] discussed the MCMP diffusion model in detail. It is concluded that the diffusion satisfies the Galilean invariant and the diffusion coefficient is not associated with velocity. The interaction strength has been used to control the miscibility for each component. The advantage of this method of investigating the dissolution and dispersion is that the moving boundary between fluids is easily achieved by the algorithm. However, in this model, the interfacial tension and diffusion are modelled by one force term. It is difficult to distinguish the diffusion from the interfacial tension in two components/phases.

(*ii*)Passive Solute Model [214]. This method introduces an additional lattice to describe the solute concentration using an individual equilibrium distribution function with four velocities. The velocity of the passive solute component is coupled with the fluid component. The relaxation time of the solute lattice is related to the diffusion coefficient. In this method, the interaction force between the solvent and solution are ignored. Clearly the additional lattice describing the concentration requests more computational resources.

(*iii*)Solute transfer in the solid-liquid interface. This method was successfully used to simulate solid dissolution and precipitation. The boundary conditions between components/phases were treated specifically for the solid dissolution, such as that proposed by Kang et al. [125]. It has been adopted in the droplet dissolution simulation by Chen et al. [20] with the assumption of a fixed fluid-fluid interface.

3.10. Reviews of mass transfer models of MCMP LBM

Based on the discussion above, no appropriate mass transfer models for LBM have been developed. Therefore, it is necessary to develop a suitable physical model to simulate mass transfer, which has been fully engaged for model development, mass and energy.

Chapter 4

Development of LBM CO$_2$ dissolution model

4.1   Introduction

In the CO$_2$ geological storage, injected CO$_2$ is at a free supercritical phase. As the density of supercritical CO$_2$ is lower than that of the aqueous phase, CO$_2$ tends to escape from the storage site driven by the upward buoyancy force.

The geochemical trapping occurs and restrains the migration of CO$_2$. The CO$_2$ dissolves into brine causing its density to increase at orders of 0.1% to 1%, depending on pressure, temperature, and salinity, as shown in Figure 4.1. The density increase of CO$_2$ creates a solute induced buoyancy force. This negative buoyancy force generates an additional nature convection on the interface between CO$_2$ and the aqueous phase to refresh the interface between CO$_2$ and brine, consequently enhancing the CO$_2$ dissolution. In this study, convection is defined by the movement of fluid molecules through adcection, which not include the diffsuion. The rate of CO$_2$ dissolution would be limited by the rate at which CO$_2$ can be removed from the interface by molecular diffusion. On the other hand, the CO$_2$ solution reacts with the mineral to form carbonates and is trapped as the solid phase. The study of the CO$_2$ solute driven convection corresponds to the security and CO$_2$ permanence storage.

To fully understand this complex interaction mechanism, which is the key predicting CO$_2$ leakage from the storage sites, it is vital to develop a pore-scale mechanism model to simulate such a multiple fluids interaction process in geo-formation. Based on the literature reviews on applications of LBM to mass transfer in Section 3.10, it is clear
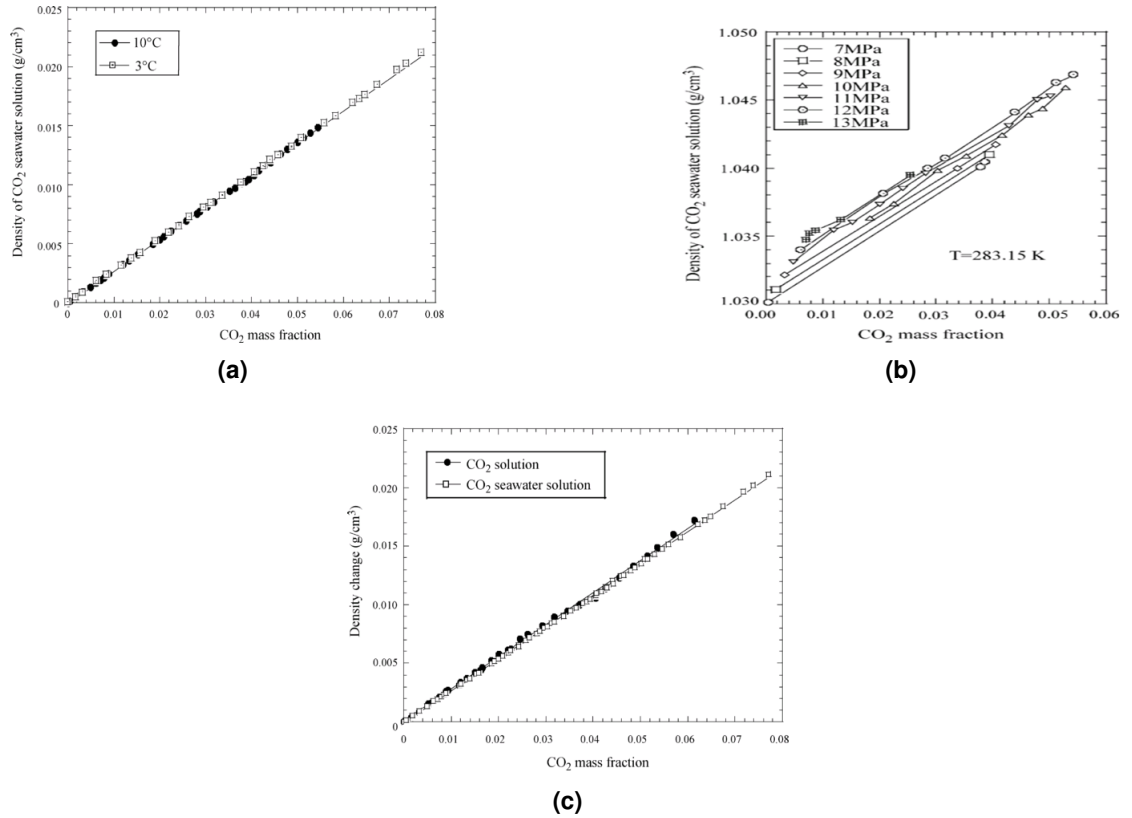
Figure 4.1: Density increase of CO_2 solution under different (a) temperature; (b) pressure; (c) salinity [80]

.

that none of the existing models have been adequate to accurately describe fluid-fluid dissolution. As a result, a new two component dissolution LBM model is proposed in this study. The model is introduced in this chapter in detail.

This chapter is organized as follows. The mechanisms and physical model of CO_2 dissolution in water is studied in Section 4.2, which is demonstrated to build up the LBM model for the CO_2 dissolution model. In Section 4.3, the basic equations of this multi-component dissolution model are introduced, followed by an evaluation of the proposed diffusion force. In Section 4.4, the developed dissolution model is calibrated by simulating a lab experiment of CO_2 droplet dissolution. The parameters of the LB simulation are converted by the physical parameters. The EOSs of CO_2 and water are proposed. The simulation results are discussed in Section 4.5, including the effect of the *Eo* number and numerical diffusion on the performance of static droplet dissolution. Finally, A summary and conclusions can be found in Section 4.6.
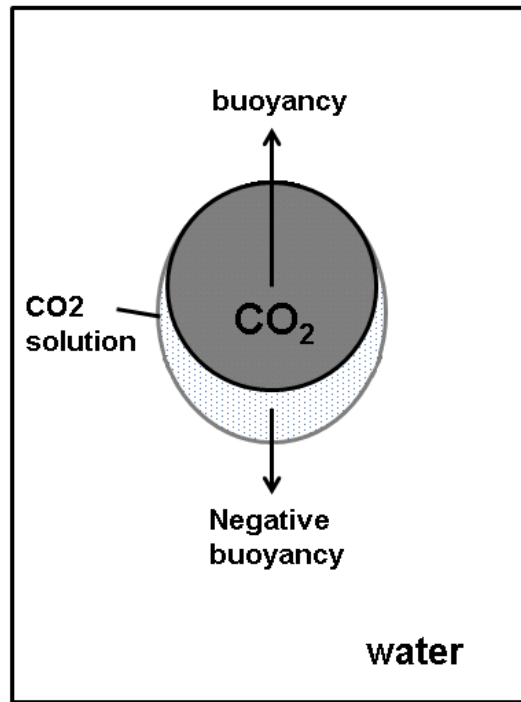
Figure 4.2: Schematic diagram of the CO_2 droplet dissolution mechanisms

4.2 Mechanisms and physical model of CO_2 dissolution in water

The model considers a free rising CO_2 droplet in water, without loss of general, at a state of CO_2 geological storage site. For such a system, CO_2 and water are assumed to be at a thermal equilibrium state and conservation of energy is satisfied.

The momentum exchange of CO_2 and water is driven by forces of buoyancy, viscosity, and interfacial tension. Experimental data shows that at storage state (1000-3000 m depth), CO_2 is lighter than water, while the CO_2 solution is denser than water. Therefore, there will be both positive ($\rho_c < \rho_w$) and negative ($\rho_s > \rho_w$) buoyancies, as shown in Figure 4.2, where ρ is the density and the subscribes c, w and s indicate CO_2, water and CO_2 solution, respectively.

The mass exchange of CO_2 and water is due to CO_2 dissolution. This model assumes that the solution forms a layer at the solute and solvent interface. The reaction at the solute and solvent interface is assumed to instantaneously form a saturated solution at

4.2. Mechanisms and physical model of CO_2 dissolution in water
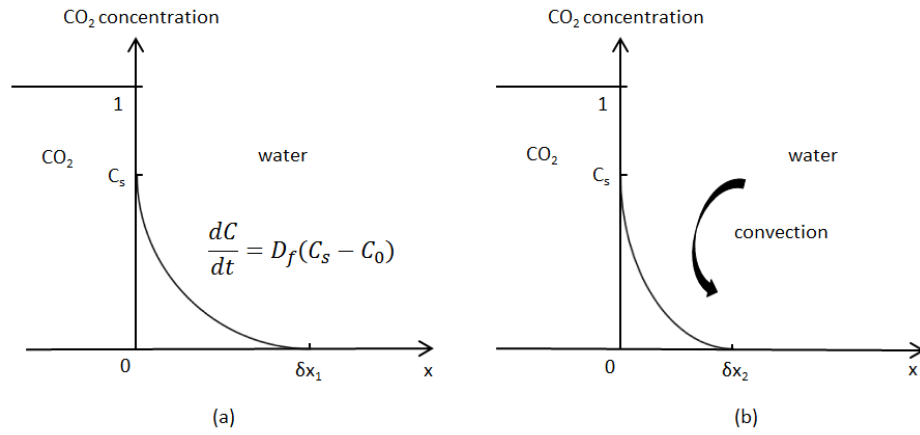
Figure 4.3: Schematic diagram of a physical model in dissolution process. (a)stage one; (b)stage two. Note that $\delta_{x2} \leq \delta_{x1}$.

mass concentration of C_s, namely solubility, which is a physicochemical property of function of temperature and pressure. The rate of dissolution is then controlled by the diffusion of solute molecules from the diffusion layer at the concentration of solubility to the surrounding liquid, which is driven by the concentration gradient.

The momentum and mass exchanges of CO_2 and water are coupled during CO_2 rising, deformation and dissolution. The coupling occurs in two boundary layers of momentum and concentration, which are generated by the coupling of the forces, including positive and negative buoyancies, interfacial tension and viscosity, and the coupling of flow and mass transfer. Flow enhances the mass transfer of CO_2 to water. Meanwhile, the mass transfer of CO_2 dissolution produces negative buoyancy.

A LBM MCMP model is proposed to simulate the CO_2 dissolution. The CO_2 dissolution process can be classified into two stages, as shown in Figure 4.3.

In the first stage, CO_2 diffusion is driven by the gradient of the chemical potential. The chemical potential can be expressed by a thermodynamic force representing the spontaneous tendency of the molecular dispersion as a result of the Second Law of thermodynamics. The diffusion flux is governed by Fick's First Law of Diffusion, which is defined as $F_x = -D_f \frac{\partial C}{\partial x}$, where F_x and C are mass flux and the concentration of the diffusion substance, respectively. Taking the Diffusion Layer Model of dissolution into account, when CO_2 is in contact with water, the diffusion layer film instantaneously forms a state of equilibrium on the interface. Therefore, at the interface, the maximum concentration of

CO_2 for mass transfer is CO_2 solubility rather than the total CO_2. Once CO_2 has diffused into the water, a concentration layer forms with concentrations between the CO_2 solubility and that in the surrounding water. The dissolution is ongoing until the chemical potential gradient of the CO_2 in the solution approaches a negligible amount.

In the second stage, once the CO_2 is diffused into the diffusion layer, the convection takes the role of moving the dissolved CO_2 away from the diffusion layer, which is generated by the forces of buoyancies. The pure diffusion layer transfers to a thin convection diffusion layer, as shown in Figure 4.3. The change of the concentration from the diffusion layer is the sum effect of the diffusion and convection.

In LBM, the solution is considered as a mixture of dissolved CO_2 and water, which is governed by the transport equation of water. Therefore, the density of the solution is the density of the mixture of water and dissolved CO_2, while an additional force, the negative buoyancy force, should be added to the momentum equation of water. By such a treatment, unlike existing models of LBM MCMP, no additional Lattice is requested for the CO_2 solution. The interface between the solute of CO_2 and solvent (water) is monitored by the solubility, which moves as the CO_2 dissolves.

4.3   Multicomponent LBM dissolution Model

Based on the discussion of the mechanisms and physical model of CO_2 dissolution, a LB CO_2 mass transfer model is developed. The pseudopotential model [147] introduced in Section 3.4 is applied to describe the chemical potential (diffusion coefficient). The model couples mass transfer and momentum transfer. The momentum transfer forces, including interfacial tension, the interparticle interaction force for real fluid, and buoyancy, are introduced in Section 3.6. In this section, the diffusion force is investigated and developed.

4.3. Multicomponent LBM dissolution Model

4.3.1   The diffusion force

In the proposed dissolution model, a diffusion force is introduced to simulate the CO_2 particles transfer to water. By applying the interparticle interaction pseudopotential concept, the diffusion force is defined as,

$$F_{\sigma\bar{\sigma}}^d = -G_d \psi_\sigma(x) \sum \psi_{\bar{\sigma}}(x^{'})(x^{'} - x) \tag{4.1}$$

where G_d is diffusion potential strength of the solute particles transporting into the solvent. ψ_σ and $\psi_{\bar{\sigma}}$ are the effective number density of solute and solvent in the solution, respectively, which are determined by EOS of solute and solvent, respectively. For CO_2 and water system, ψ_{CO_2} and ψ_{water} are to be introduced in Section 4.4.3.

It can be seen from the proposed diffusion force that CO_2 diffusion can be directly described from the mechanisms of particle interactions, rather than by means of adopting an additional transport LB equation to link the diffusion coefficient to the relaxation time, where it should be noticed that an additional equilibrium function for diffusion component also has to be set up. Looking at the mechanisms of dissolution, the inter-particles interaction actually occurs at all directions rather than just four directions, as is also the case regarding the forces. Consequently, the diffusion of CO_2 into water can be predicted by simply implementing such a diffusion force into the momentum equation. Shan-Chen discussed the diffusion phenomena in the multicomponent LBM model [228]. However, the diffusion force was not distinguished from the interaction forces in their multicomponent model.

The diffusion potential strength used to simulate the diffusion coefficient can be calibrated by the analytical solution of a one-dimensional semi-infinite diffusion.

The mass diffusion flux F_x is given by [229]

$$F_x = -D_f \frac{\partial C}{\partial x} \tag{4.2}$$

where C is the concentration of the diffusion substance, x is the coordinate and D_f is the diffusion coefficient.

4.3. Multicomponent LBM dissolution Model
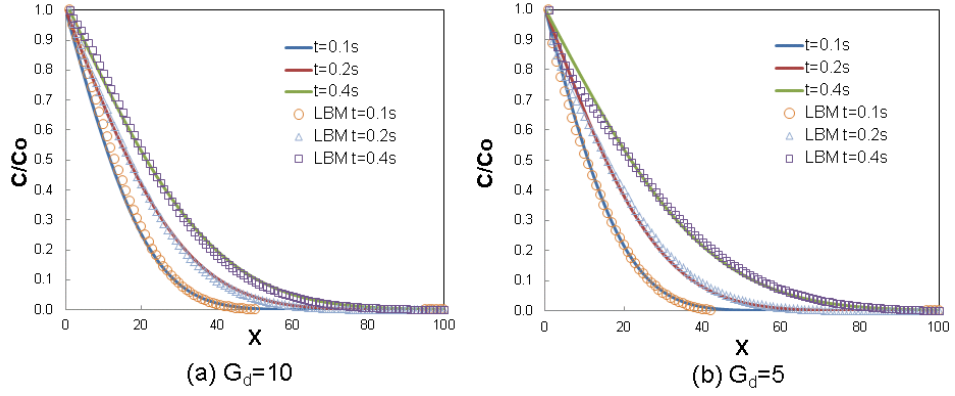
Figure 4.4: Diffusion from a semi-infinite medium. Analytical solution shown as solid line, LBM solution as open symbols.

One dimension transportation equation of mass transfer is,

$$\frac{\partial C}{\partial t} + \frac{\partial F_x}{\partial x} = 0 \tag{4.3}$$

Substitute Eq.4.2 into Eq.4.3, a analytical solution of diffusion can be obtained [229]

$$C = C_0 erfc \frac{x}{2\sqrt{D_f t}} \tag{4.4}$$

by setting the initial condition, $C = 0$ at $x > 0, t = 0$, and boundary condition of $C = C_0$ at $x = 0, t > 0$. C_0 is the concentration of the diffusion boundary. In the proposed dissolution model, C_0 is the solubility, C_s.

A 2D LBM simulation is conducted to simulate spherical droplet diffusion into water with the periodic boundary condition. Along the central line of the diffusion bubble, the diffusion is regarded as the semi-infinite diffusion on each side.

Figure 4.4 shows the comparison results of concentration distributions between the LB simulation and analytical solution under two diffusion potential strengths, they are G_d=5 and G_d=10, respectively. It can be seen that the LB simulation results of the concentration distribution at each selected time are in a good agreement with those from the analytical solution [229]. The simulation demonstrates that the proposed diffusion force is able to describe the molecular diffusion in the LB simulation.

The relationship between the diffusion coefficient (D_f) and diffusion potential strength
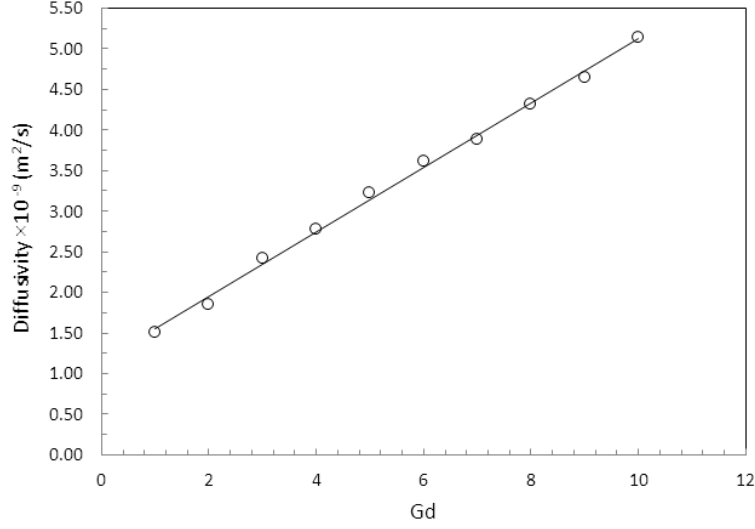
Figure 4.5: The relationship between the diffusion coefficient and diffusion potential strength G_d.

is obtained, as shown in Figure 4.5. It presents that the diffusion coefficient linearly increases with the increase of the diffusion potential strength G_d. The diffusion potential strength G_d is as a function of diffusion coefficient, in this case, is found to be

$$G_d = 0.2475 \times 10^{10} D_f - 2.72277 \tag{4.5}$$

where G_d is in LB unit and D_f is in m^2/s. It has to be noticed that Eq.4.5 is the result from the case set, which is taken to demonstrate the methodology to link the G_d in LBM to D_f in physics as an example. For other cases, the same method can be used to obtain the relationship between the diffusion potential strength and the diffusion coefficient.

4.3.2   LBM dissolution model

Based on the mechanisms and physical model of CO_2 dissolution in Section 4.2, in this section, the LBM dissolution model is introduced. The characteristic of this model is the implementation of the momentum and mass transfer forces in LBM.

For the CO_2 and water system considered in this study, the forces acting on the CO_2 are those of interparticle interaction forces between molecules, F_{11}^f, the interfacial tension, F_{12}^f, and gravity, F_1^g. In the case of water, they are the interparticle forces F_{22}^f, the interfacial tension F_{21}^f and gravity, F_2^g. The net gravity is applied to the CO_2 droplet, known

as buoyancy force. Therefore, the forces applied in the momentum equations of CO_2 and water are

$$F_c = F_{11}^f + F_{12}^f + \left(F_1^g - F_2^g\right) \tag{4.6}$$

and

$$F_w' = F_{22}^f + F_{21}^f \tag{4.7}$$

where F_{11}^f, F_{12}^f, F_1^g and F_2^g have been introduced in Section 3.6.

At the interface between the CO_2 and water, molecular diffusion and convection occurs. The diffusion is described by the diffusion force, F^d. The CO_2 is dissolved into water and treated as a solution. Since the CO_2 concentration is small in mass fraction, known as $C < C_s = 0.05$, the interparticle force F_{11}^f of the CO_2 solution is neglected and the CO_2 is treated as water. C_s is the CO_2 solubility in mass fraction. In addition, once the CO_2 is dissolved into water, the density of the CO_2 solution is greater than the density of the water. Therefore, a negative buoyancy force, which is cannot be ignored, is applied to the water component. The forces for the water component is summarized by

$$F_w = F_w' + F_{21}^d + \left(F_s^g - F_2^g\right) \tag{4.8}$$

where F_s^g is the gravity of solution, $F_s^g = \rho_s g$. The CO_2 solution density (ρ_s) is calculated by the equation proposed by Song et al. [22], $\rho_s = \rho_w(1 + \alpha\chi)$. α is the constant, $\alpha = 0.275$ for fresh water and $\alpha = 0.276$ for seawater [22].

The flowchart of the multicomponent LBM dissolution model is illustrated in Figure 4.6.

4.4 Calibration of the new LBM dissolution model

In this section, the proposed multicomponent LBM dissolution model is calibrated by a lab experiment in terms of the shrinking rate and solution layer thickness. The initial parameters in the LBM dissolution simulations are based on the conversion from the physical unit. The EOSs of the CO_2 and water are investigated and improved.
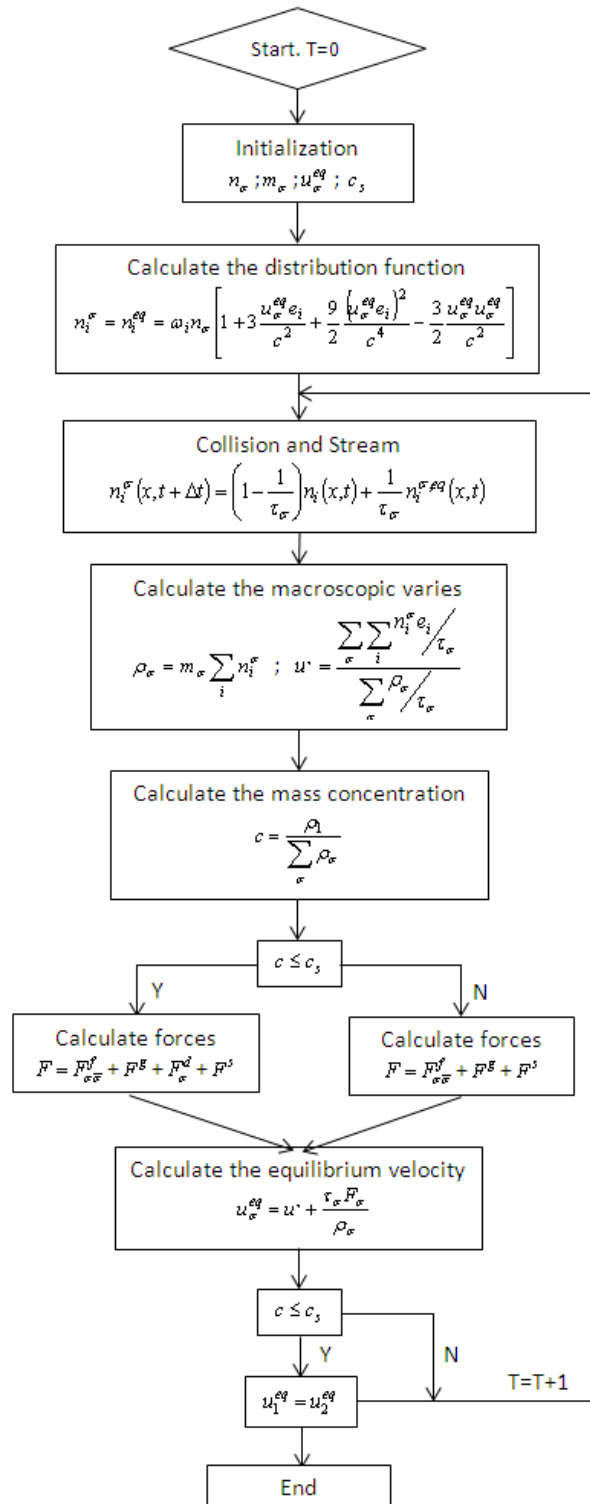
Figure 4.6: The flowchart of multicomponent LBM dissolution model
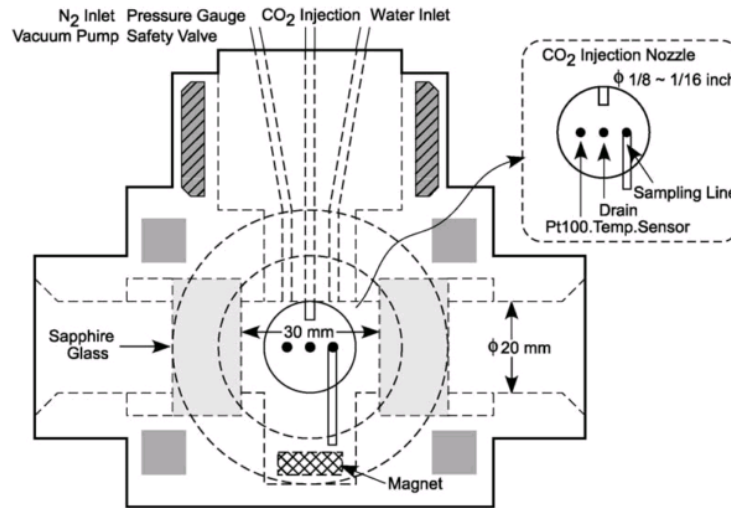
Figure 4.7: Schematics of the experiment set up [21]

4.4.1 Lab experiment of CO_2 dissolution

The proposed multicomponent LBM dissolution model is calibrated by the CO_2 droplet dissolution experiment [21]. The structure of the high pressure vessel of the experiment is schematically outlined in Figure 4.7. The test section is an optical transparent channel at the center of the vessel. Having filled with water, the vessel was maintained at a state of T=288 K and pressure of 9.81 MPa. CO_2 was injected into the water to form a droplet touching to the injection nozzle due to the buoyancy. The CO_2 droplet dissolution was monitored by a high speed camera and the concentration distribution of the dissolved CO_2 was measured by the DeLIF technique. The CO_2 concentration distribution calculated from a PH distribution which can be seen in Figure 4.8.

4.4.2 LBM simulation set-up

The LBM is set to simulate the experiment. The correspondence of the simulation parameters between the lab experiment and the LBM are listed in Table.4.1. The number density for CO_2 and water are n_1=2.02 and n_2=5.5756, respectively. The molecular mass for each component are m_1=44 and m_2=18, respectively. The gravitational acceleration was set based on the non-dimensional number Eo. $Eo = \frac{g\Delta\rho d^2}{\sigma}$, where $\Delta\rho$ is the density difference between two fluids. g is the gravitational acceleration. d is the characteristic length, in this study it is defined by the radius. σ is the surface tension. In the lab experimental
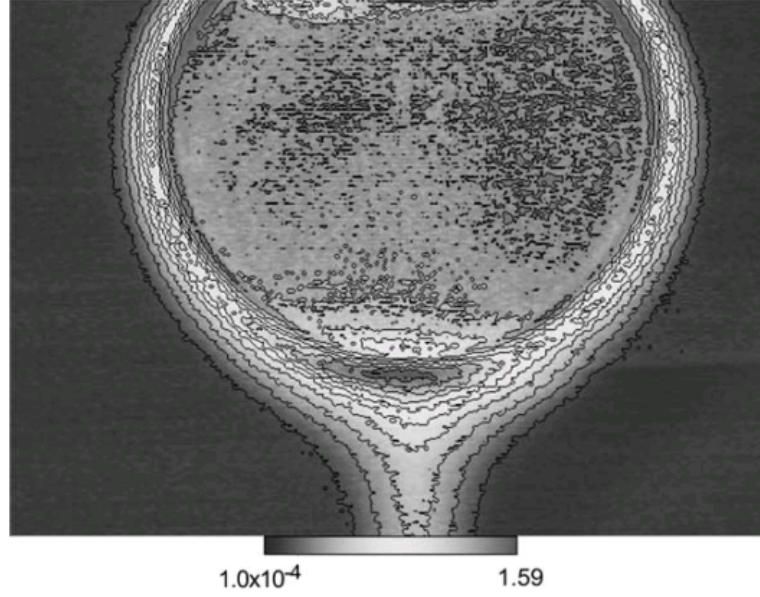
Figure 4.8: The experiment result of the CO_2 concentration (mol/l) distribution [21]

condition, the surface tension is 25 mN/m, therefore, the *Eo* number was calculated as $(1003.611 - 889.21) \times 9.81 \times (5 \times 10^{-3})^2/25 \times 10^{-3} = 1.2387$. In the LBM, the surface tension is not given as a known parameter. The surface tension is determined according to Laplace's law in the stationary droplet without dissolution and gravity. The surface tension is obtained by 122.5769. Therefore, the gravitational acceleration is set to be 0.004973 in LB simulation.

4.4.3 Equation of state

To simulate CO_2 dissolution in water, the EOSs of CO_2 and water must be developed in the LBM, in addition to the LB equations and forces.

EOS for CO_2

Based on the literature reviews in Section 3.6.1, PR EOS [183] is selected for CO_2, which is given by

$$\rho = \frac{\rho RT}{1-b\rho} - \frac{a\alpha(T)\rho^2}{1+2b\rho-b^2\rho^2} \tag{4.9}$$

$$\alpha(T) = \left[1 + \left(0.37464 + 1.54226\omega - 0.26992\omega^2\right) \times \left(1 - \sqrt{T/T_c}\right)\right]^2 \tag{4.10}$$

4.4. Calibration of the new LBM dissolution model

Table 4.1: The correspondence of the simulation parameters between physical unit and LB unit

	Lab experiment	LBM simulation
Temperature	288 K	1
Pressure	9.81 MPa	0.981
Lx	30 mm	300
Ly	30 mm	300
Radius	5 mm	50
CO_2 density	887.34 kg/m^3	88.734
Water density	1003.611 kg/m^3	100.3611
CO_2 viscosity	$0.104 \times 10-6 \ m^2/s$	τ=0.546
water viscosity	$1.13 \times 10-6 \ m^2/s$	τ=1.0
gravity	9.81	4.973×10^{-4}

where $a = \Omega_a R^2 T_c^2 / p_c$ and $b = \Omega_b R T_c / p_c$. For CO_2, Ω_a=0.45724, Ω_b=0.077393, the acentric factor ω=0.2249 [17] and the critical point is T_c=304.25 K, P_c=7.38 MPa, ρ_c=468 kg/m^3.

PR EOS is calibrated by CO_2 experimental data of the pressure against the density at T=288 K, as shown in Figure 4.9. It was found that the pressure calculated by PR EOS deviates remarkably from the experimental data, especially at the state of the lab experimental condition (T=288 K P=9.81 MPa). The pressure error $((P_{Eq} - P_{real})/P_{real})$ between PR EOS and experimental data is approximately 11.4%. Since an accuracy EOS is important for LBM simulation, the PR EOS is corrected to fit the experimental data. The parameters of the corrected PR EOS are Ω_a=0.5167 and Ω_b=0.08255.

It can be seen from the red colour line in Figure 4.9 that the improved PR EOS fits well with the experimental data, especially at the pressure in the range of 6.4 MPa to 10.4 MPa, which covers the lab experimental condition. The pressure error is significantly reduced to 0.031% at T=288 K P=9.81 MPa. Therefore, the improved PR EOS is utilized in this study.

The corrected PR EOS is then converted to LB EOS, according to the corresponding states law. The converter between the physical unit and LB unit is established as below using

4.4. Calibration of the new LBM dissolution model
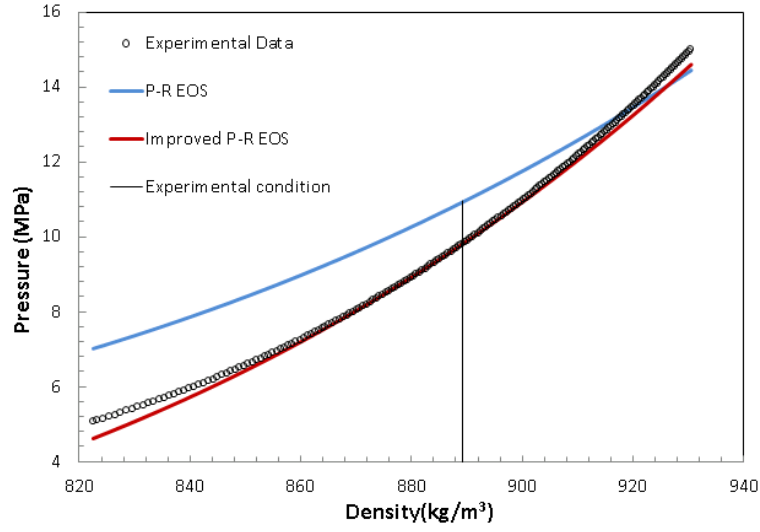
Figure 4.9: The CO_2 pressure changes with density at T=288 K for the experimental data, PR EOS and the improved PR EOS

the critical state,

$$
\begin{aligned}
\frac{\rho^{LB}}{\rho_c^{LB}} &= \frac{\rho^{phy}}{\rho_c^{phy}} \\
\frac{p^{LB}}{p_c^{LB}} &= \frac{p^{phy}}{p_c^{phy}} \\
\frac{T^{LB}}{T_c^{LB}} &= \frac{T^{phy}}{T_c^{phy}}
\end{aligned}
\tag{4.11}
$$

where superscripts *phy* and *LB* denote the physical and lattice Boltzmann unit, respectively. The critical properties in LB unit are set by T_c^{LB}=1.0564, and P_c^{LB}=7.52 and ρ_c^{LB}=5.2291. Therefore, the unit converter of temperature, pressure and density are set to be $\frac{T_c^{phy}}{T_c^{LB}}$=288, $\frac{P_c^{phy}}{P_c^{LB}}$=$10^7$ and $\frac{\rho_c^{phy}}{\rho_c^{LB}}$=$10^4$, respectively.

Based on the unit converter, the PR EOS in LB unit is obtained with the parameters, a=0.2283, b=6.43$\times 10^{-12}$, R^{LB}=1. At the lab experimental state, the LB pressure, temperature and density are P^{LB}=0.981, T^{LB}=1.0 and ρ^{LB}=88.921. The number density of CO_2 is set to be n_c^{LB}=2.02.

Having the LB EOS, the interparticle interaction force of CO_2, F_{11}^f in Eq.4.6, can be identified by taking the interaction potential $\psi(\rho) = \rho_0 \left[1 - exp\left(-\rho/\rho_0 \right) \right]$. Incorporating

4.4. Calibration of the new LBM dissolution model

Table 4.2: water PR EOS parameters

Property	Value
ω [230]	0.344
T_c(K)	647.096
P_c(MPa)	22.064
$\rho_c(kg/m^3)$	322
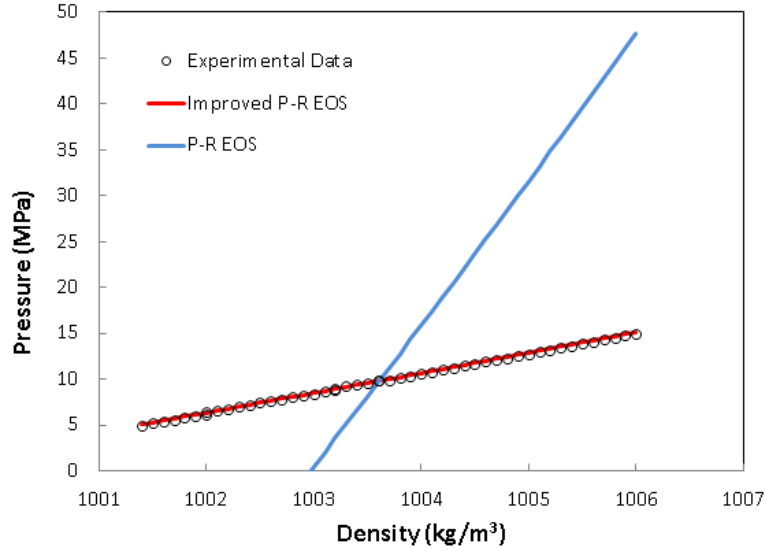
Figure 4.10: The water pressure changes with density at T=288 K for the experimental data, P-R EOS and the improved P-R EOS

Eq.3.23, the interaction potential of CO_2 is obtained by

$$G_{11} = \frac{6\left(P - \frac{\rho}{3}\right)}{\psi(\rho)^2} \qquad (4.12)$$

where P and ρ are the pressure and density in LB unit. At the lab experimental state, the value of CO_2 molecular interaction potential strength is calculated as G_{11}=-0.408446.

EOS for water

As the same treatment of CO_2 EOS, the PR EOS is applied to describe the property of water. The parameters for water's PR EOS are listed in Table.4.2

The values of Ω_a and Ω_b are corrected from those suggested by Yuan [185], which are 0.45724 and 0.06729465, respectively. The corrected Ω_a and Ω_b are 0.1919 and 0.059, respectively. As shown in Figure 4.10, the corrected PR EOS well fits the experimental

data at the lab experimental condition.

In LBM, the parameters of water EOS at lab experimental condition are R^{LB}=1, P^{LB}=0.981, T^{LB}=1.0 and ρ^{LB}=100.3611. The number density of water is 5.5756. The molecular interaction potential strength is calculated G_{22}=-0.8842 by Eq.4.12.

4.4.4 Model calibration

Simulation set-up

The dissolution model is calibrated by the simulation of the CO_2 droplet dissolution experiment [21]. The experiment is considered as a two-dimensional CO_2 droplet dissolution as it did in a cylinder vessel and the nozzle is located at the centre. As the inside size of the test section in the experiment is not mentioned in the paper [21], the LBM simulation was carried out by setting a 2D square domains with 300×300 lattices, in which a CO_2 droplet with radius 50 is located at centre of the top of the domain (the droplet centre is located on x=150, y=250). The resolution and discrete time step are based on the discussed in Section 3.9. The rest of the domain was filled with water. LBM simulation initialized from the end of CO_2 injection. For simplification, injection process is not included. Both of the top and bottom boundaries are the full bounce-back of the wall. The left and right are set to be the periodic boundary condition. Based on the experimental results as shown in Figure 4.1a, the CO_2 solubility is 0.05 at T=288 K and P=9.81 MPa. The interparticle interaction strength G_{12} is selected to be 7.4, based on the discussion in Section 4.5.3. As the discussion of the diffusion force in Section 4.3.1, the diffusion potential strength taken in this simulation is G_d=1.0.

Shrinking rate

The model is calibrated by droplet shrinking and shrinking rate. Droplet dissolution rate can be well demonstrated by the shrinking rate. Since the droplet deforms during dissolution, a normalized effective radius (R^*) is defined as R^*=R_i/R_0, where R_i=$\sqrt{S/\pi}$. S is the area of CO_2 droplet. R_0 is the initial droplet radius. The shrinking rate is defined by dR^*/dt.

4.4. Calibration of the new LBM dissolution model
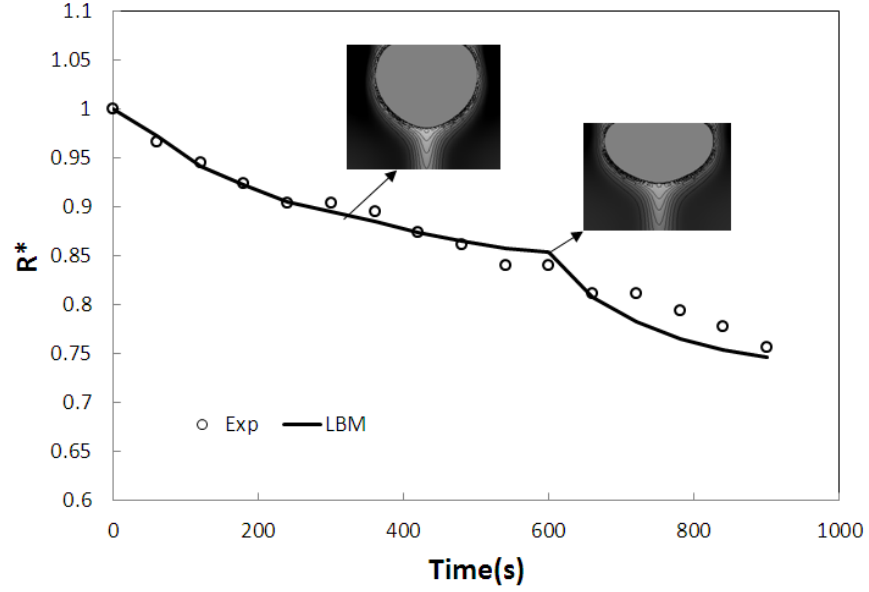
Figure 4.11: Changing of the normalized CO_2 droplet radius with time for both lab experiment and LBM simulation.

It can be seen from the comparison between the results from the lab experiment [22] and the LBM that the droplet shrinking is very well predicted by the developed LBM. The mean shrinking rates are 2.63×10^{-4} and 2.7×10^{-4} for the LBM and the lab experiment in 900 seconds, respectively, as shown in Figure 4.11. A very interesting finding from the LBM simulation is that the droplet retains a spherical shape during the first 600 seconds, which results in a shrinking rate of 2.4×10^{-5} 1/s. This ratio is very close to that of the lab experiment, which is 2.7×10^{-5} 1/s, as shown in Figure 4.11. The deformation of droplet appears from time of 600 seconds, which is due to the formation of a full-developed flow boundary around the droplet by the negative buoyancy. The deformation of the droplet enlarges the interfacial area between the CO_2 and the water, then, in turn, enhanced the dissolution rate, in addition to the enhancement of convections.

The dimensionless transfer rate for mass transfer, Sherwood number, is used to represent the mass transfer ratio of convection to diffusion and obtained by the shrinking rate of droplet. The Sh number is defined by,

$$Sh = kD/D_f \tag{4.13}$$

where D_f is the molecular diffusion coefficient (m^2/s), D is the effective diameter of
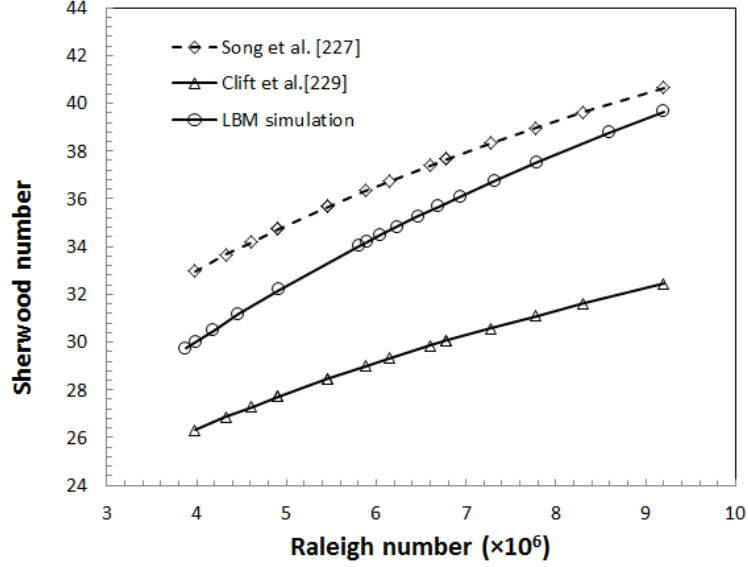
Figure 4.12: The relationship between Sherwood number and Rayleigh number matched to the experimental data from Song et al. [22] and Clift et al. [23]

droplet (m), $D=2\times R_i$. k is the mass transfer coefficient (m/s), which is calculated by mass transfer rate, $\frac{dm}{dt} = -kA\chi\rho_s$. A is the surface area of droplet (m^2/s). χ is the CO_2 concentration in mass fraction. ρ_s is the density of CO_2 solution.

Rayleigh number for nature convection is defined as

$$Ra = \frac{\alpha\chi}{1+\alpha\chi}\frac{gD^3}{\upsilon D_f}$$ (4.14)

where υ is the kinetic viscosity of water (m^2/s). g is gravitational acceleration (m/s^2).α=0.275 for water [22].

The relationship between Sherwood number and Rayleigh number is determined by the simulation results of shrinking rate, surface area and gravity. The comparison result between the simulation result and the experimental data is shown in Figure 4.12. It can be seen that the simulation result is between the formulation in textbook [23] and the experiment data [22]. The simulation result is smaller than the experimental data, due to the different initial droplet size and error of surface area of the droplet resulted by the deformation of droplet.
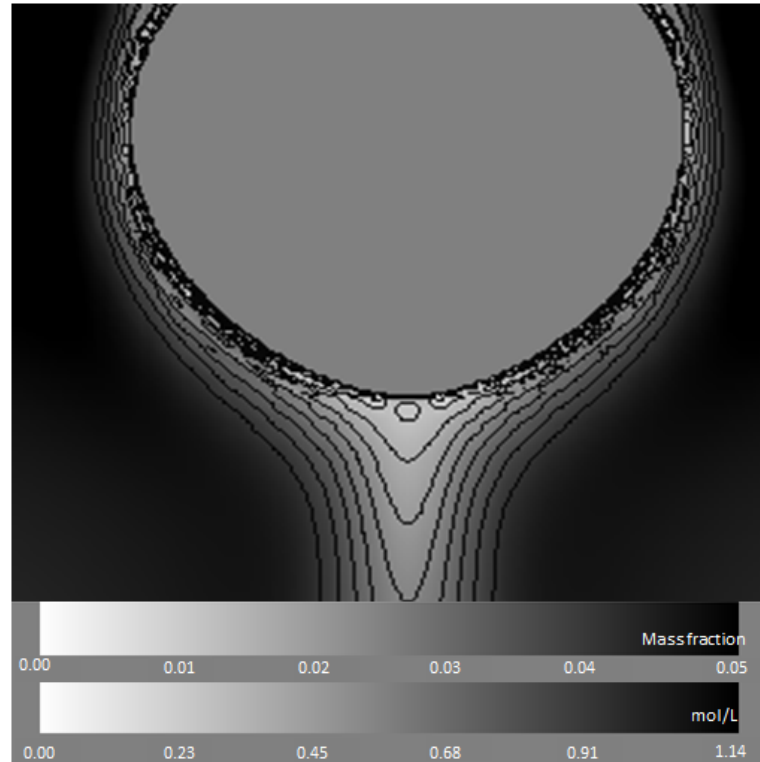
Figure 4.13: LBM simulation results of the CO_2 droplet concentration distribution.

Distribution of dissolved CO_2

The mechanisms of CO_2 dissolution in water by coupling the diffusion and convection can be demonstrated in detail by the distribution of dissolved CO_2 in the concentration layer.

The general distribution of dissolved CO_2, shown in Figure 4.13, is compared with that from the lab experiment, as shown in Figure 4.8, in terms of mass fraction. The difference in mass concentration is due to the selection of CO_2 solubility, which is 0.068 in the lab experiment, but 0.05 in the LB simulation. It is checked that 0.05 is a more reasonable value at the experimental state. It can be seen that the LB simulation agrees well with that of the lab experiment, within the inner layer. Some part-marks-like high concentration areas are produced close to the CO_2-water interface. These are assumed to be the results of interparticle interactions (diffusion and interfacial tension) and buoyancy driving flows. The out-layer is mostly dominated by the convection and the distinguished contours can be formed.

The CO_2 dissolution is examined by the geometry characteristics of concentration layer.
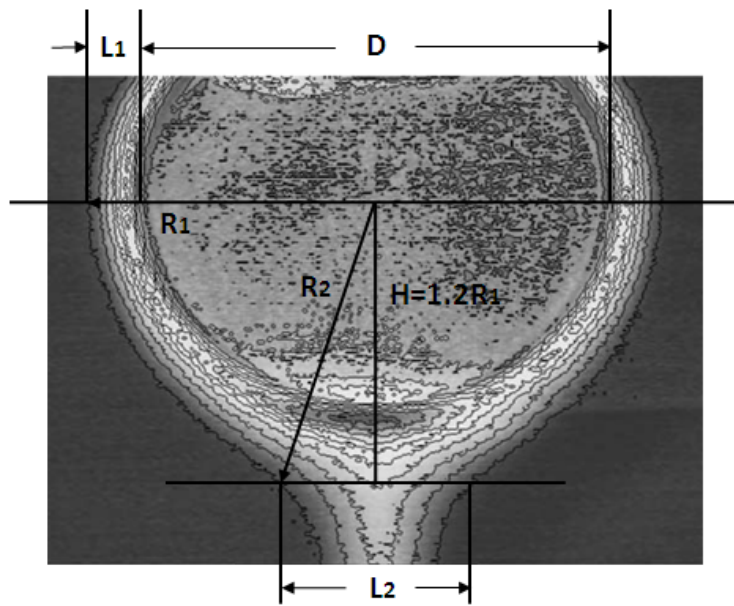
Figure 4.14: Schematic of the CO_2 droplet solution analysis

Table 4.3: The comparison of the CO_2 solution layer between LBM simulation and the experimental result

	LBM	Experiment	error
L_1/D	0.0829	0.102	18.7%
L_2/D	0.428	0.469	8.7%
L_2/L_1	5.1628	4.598	9.5%
R_2/R_1	0.857	0.967	11.4%

The definition of geometry parameters are given in Figure 4.14. L_1 indicates the solution thickness along the maximum droplet diameter, D , in the horizontal direction. L_2 is the thickness of solution layer at H=1.2R_1. D is the maximum diameter of the CO_2 droplet in the horizontal direction.

The values of the geometry parameters are listed in Table.4.3 for both the lab experiment and the LB simulation. It can be seen that the simulation result closely matches the experimental results, with the maximum error less than 20%.
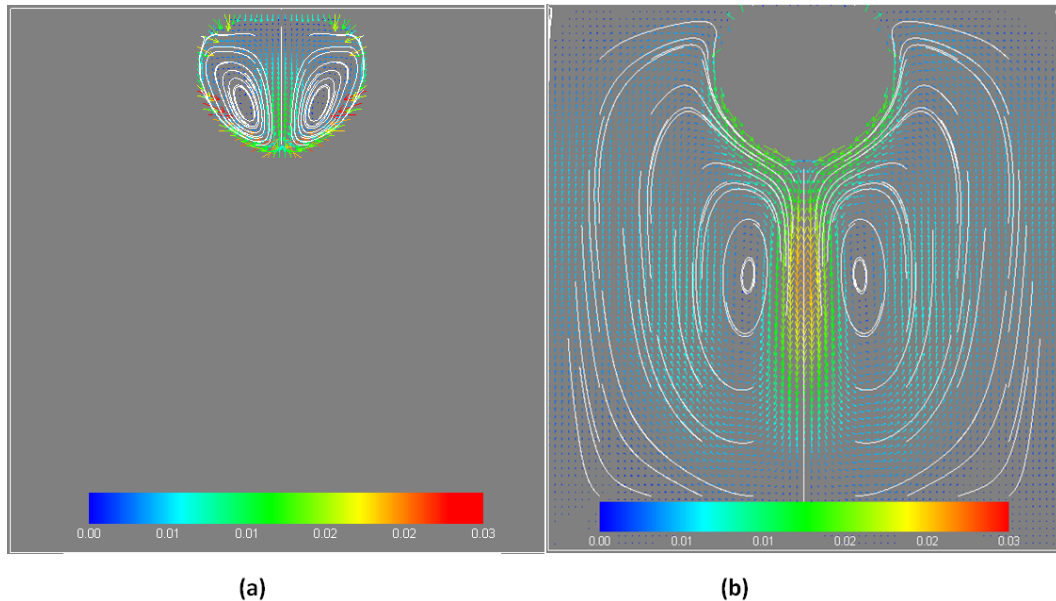
Figure 4.15: Velocity distribution (a) inside CO_2 droplet and (b) of CO_2 solution, which is denoted by the white contours and the velocity vectors. The white contours denote the streamlines.

4.5 Discussion on the static droplet dissolution

4.5.1 Velocity field of CO_2 droplet and solution

To demonstrate the flow direction of the fluid particles at any point in time, the flow field inside the CO_2 droplet and of the CO_2 solution is obtained and shown in Figure 4.15. Streamlines are everywhere instantaneously tangent to the local velocity vector, which are used to show the traveling direction of fluid in time. It can be seen that two vortexes exist inside the CO_2 droplet, which is due to the combined effects of buoyancy and interfacial tension. In addition, due to the negative buoyancy and interfacial tension of the CO_2 solution, another two vortexes symmetrically occur on both sides of the solution tail. Therefore, a low-velocity area is produced at the bottom of the CO_2 droplet. The velocity vectors in Figure 4.15 denote that the maximum velocity occurs on the interface and is 0.030159. For the CO_2 solution, the maximum velocity occurs in the solution tail far from the interface and is 0.024462.
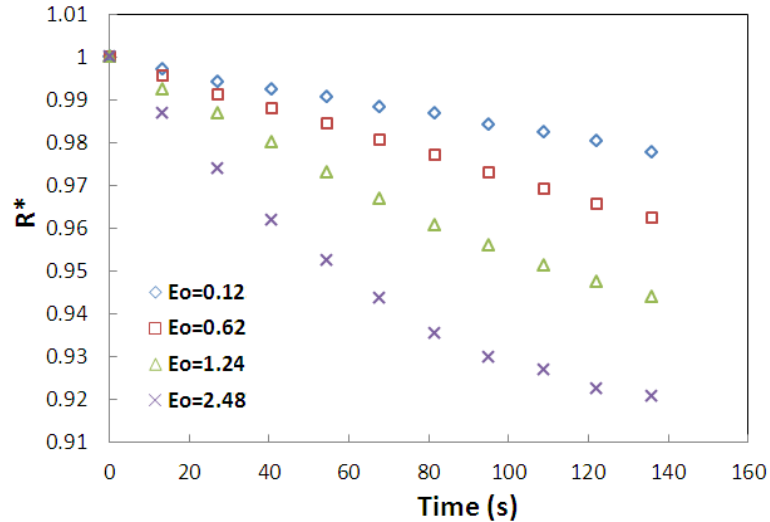
Figure 4.16: The normalized effective radius of the droplet changes with time at a series of Eo number.

4.5.2 Effect of the Eo number on the static droplet dissolution

The proposed dissolution model is used to evaluate the effect of Eo number on the droplet dissolution. The Eo number is the dimensionless number of the ratio of buoyancy force to surface tension. It is used to characterize bubble or droplet deformation. In this study, the effect of Eo number on the droplet dissolution is investigated in terms of the droplet shrinking rate and the change in the droplet shape.

The simulation is set based on Section 4.4. The different Eo numbers are achieved by the changes of gravitational factor or initial diameter of droplet.

The normalized effective radius of droplet changes with time at a series of Eo numbers are shown in Figure 4.16. The shrinking rates at different Eo numbers are obtained. The relationship between the shrinking rate the Eo number is shown in Figure 4.17. Meanwhile, the droplet shape at each Eo number is illustrated in the inset of Figure 4.17. It indicates that the shrinking rate linearly increases with the Eo number. At a low Eo number, the dissolution droplet retains spherical; meanwhile, at a larger Eo such as $Eo =2.48$, the droplet shape changes to an ellipse. Since the droplet shape differ significantly from the spherical one at $Eo= 2.48$, the normalized radius varying with time becomes nonlinear.
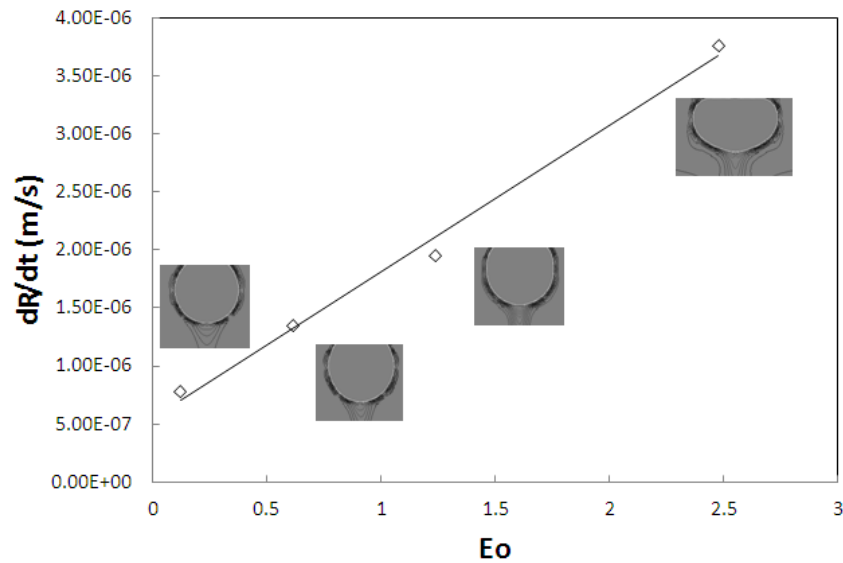
Figure 4.17: The shrinking rate varies with Eo number by LBM simulations. Pictures in the inset show droplet deformation at different Eo number.

4.5.3 Effect of numerical diffusion on the static droplet dissolution

As discussed in Section 3.6.1, an irrational interaction potential causes the numerical diffusion on the interface between two components in a multicomponent LBM simulation. In order to eliminate the interference, the numerical diffusion must be minimized in order to distinguishable from the physical diffusion. In order to further illustrate the effect of the interaction potential on the simulation accuracy, in this section a series of static droplet dissolution simulations are carried out with different interaction potential. The simulation parameters are based on the Section 4.4.

Figure 4.18 shows that the unphysical penetration density reduces with the increase in the interparticle interaction strength G_{12}. It illustrates that each component has its own unphysical penetration density changing with different G_{12}. At G_{12}=7.0, both of the unphysical penetration densities for two components are positive, namely 1.42×10^{-3} and 0.199, respectively. At G_{12}=7.4, the unphysical penetration density of CO_2 is 9.21×10^{-4}, while the unphysical penetration density of water is 0.129. They are 0.05% and 2.32% of each component's physical density. When G_{12} increases to 7.7, the unphysical penetration density of CO_2 increases to 0.02, while in the case of water it decreases to 0.018. The inset figure in Figure 4.18 shows that as the G_{12} is larger than 7.4, the penetration density of

4.5. Discussion on the static droplet dissolution
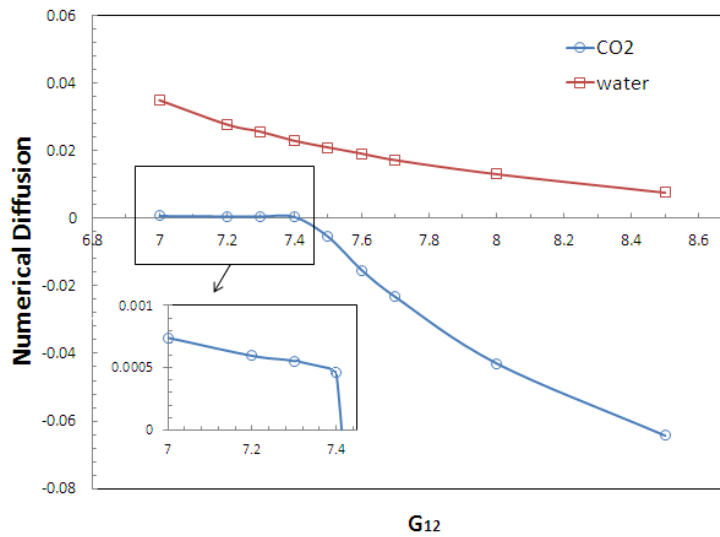
Figure 4.18: The numerical diffusion changes with the interparticle interaction strength G_{12}. The numerical diffusion is measured by the particles of CO_2 penetrated to water indicated by CO_2 density in water, and those of water penetrated to CO_2. Blue Circle: the density of CO_2 penetrated into water; Red Square: the density of water penetrated into CO_2.

the CO_2 is negative. In physics, all matter has a positive density, thus the G_{12} cannot be larger than 7.4, even though the penetration density of water continues to reduce since the G_{12} is larger than 7.4. Meanwhile, since the purpose of the study is to investigate CO_2 dissolution, the numerical diffusion of the CO_2 component must be as small as possible. Therefore, in order to minimize the numerical diffusion, G_{12}=7.4 is taken in the dissolution simulation.

The concentration distributions of the dissolved CO_2 at the same simulation time under different interaction potentials are compared and shown in Figure 4.19. The simulation results indicate that the droplet shape is different under different interaction potentials: the larger the interaction potential, the more spherical the droplet shape. The change in shape of the droplet is the result of the interactions between the strength of the interface tension and buoyancy. At G_{12}=7.0, the concentration gradient near the interface is smaller in comparison with those in the other two cases, which is assumed to be the results from the numerical diffusion of water to CO_2 and the relatively small interfacial tension that makes the droplet deformed. On the other hand, the concentration distribution shows that the concentration contours are discontinuous as negative density exists in the domain, for

4.5. Discussion on the static droplet dissolution
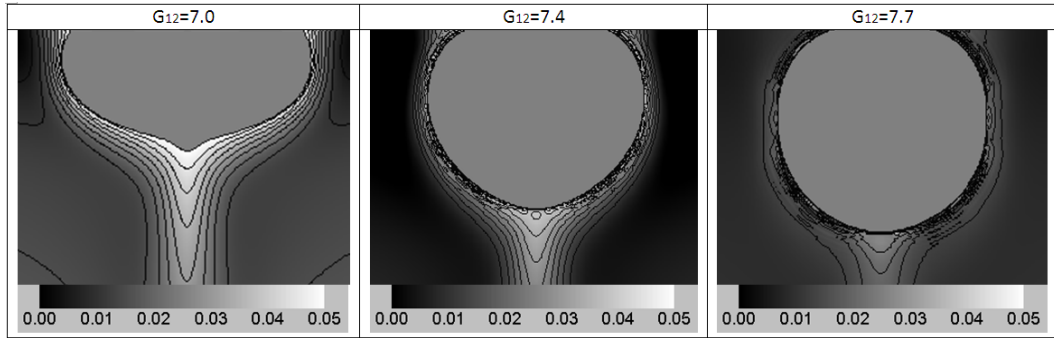
Figure 4.19: Effect of interparticle interaction strength, G_{12}, on droplet deformation and the distribution of dissolved CO_2.
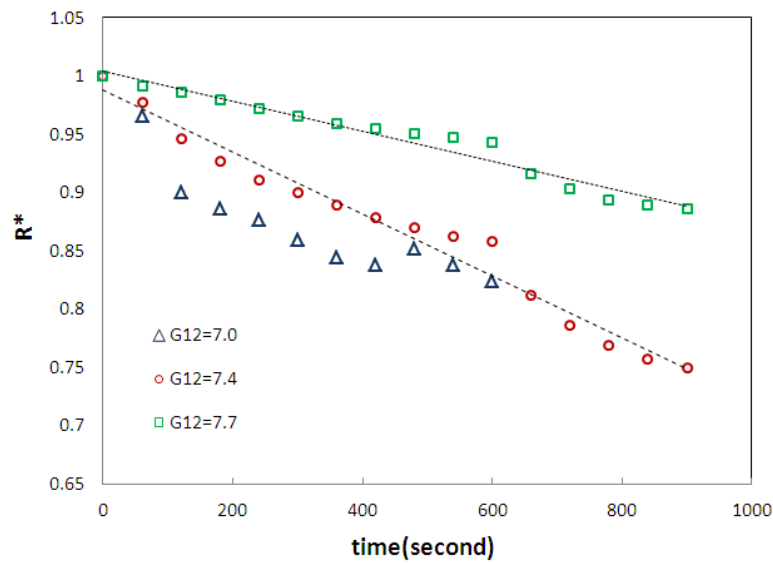
Figure 4.20: The droplet shrinking under different interparticle interaction strength G_{12}.

example at G_{12}=7.7. Therefore, it was found that a small G_{12} produces a larger numerical diffusion, which makes it difficult to distinguish numerical diffusion from real molecular diffusion. On the other hand, a larger G_{12} induces negative density, which is unlikely in physics.

The effect of G_{12} on the shrinking of droplet is shown in Figure 4.20. It can be seen that the shrinking rate reduces with the decrease of G_{12}. Apart from the general linear relations with time, when G_{12} reduces to 7.0, the CO_2 droplet dissolves faster than those of cases under G_{12}=7.4 and G_{12}=7.7 at the early stage (t<120 s), which is caused by droplet deformation. After the 120s, shrinking of the droplet tends to have a linear relation with time, when the droplet approaches a spherical shape. Therefore, the selection of interaction potential is crucial for the simulation of multicomponent LBM dissolution.

4.6 Conclusion

In this chapter, a multicomponent LBM dissolution model is proposed. In comparison with the existing dissolution models, this model has several advantages. It keeps the traditional lattices to describe each component and no lattice for the solution is used to trace the concentration. A crucial aspect of the proposed model is the introduction of a diffusion force, which describes the mechanisms of diffusion in terms of particle interaction.

The dissolution model is calibrated by the experiment results in terms of the shrinking rate and droplet deformation. The simulations by the proposed LBM dissolution model reasonably agrees with those of lab experiment. The effects of the Eo number and numerical diffusion on the performance of the dissolution of a static droplet are investigated. It was found that the shrinking rate increases with the increase of Eo number. On the other hand, the interaction potential strength must be carefully decided for LBM simulation of multicomponent dissolution. Ideally, "zero numerical diffusion" should be approached, while in practice it is difficult to achieve this. For the interparticle potential function applied in this study, extensive studies are required to reduce the numerical diffusion, such as including more neighbour lattices [207] to calculate the interparticle interaction forces or improving the structure of pseudopotential function.

Chapter 5

Applications of CO$_2$ dissolution model

5.1 Introduction

In this chapter, the developed CO$_2$ dissolution model is used to investigate the performance of a CO$_2$ droplet dispersion and dissolution in water in a channel. At the pore scale, the geoformation could be viewed as a network of channels with a variety of sizes and angles. Therefore, a series of numerical simulations are carried out to demonstrate the effect of channel width and channel tilt angle on the behavior of CO$_2$ dissolution and dispersion in water. The droplet diameter initially is 100 lattices. The channel width varies from 100 to 300 lattices and the channel tilt angle is in the range of 0°-90°. All of these simulation results are discussed and analyzed to understand the fluid dynamics of CO$_2$ droplet dissolution in the channel at pore scale.

This chapter is organized as the numerical simulation set-up is introduced in Section 5.2. In Section 5.3 to Section 5.5, the dynamics of a CO$_2$ droplet dispersion and dissolution in a channel are investigated in terms of the rising velocity, shrinking rate and droplet deformation, respectively. Finally, the conclusion is drawn in Section 5.7.

5.2 Numerical simulations set-up

In this section, the proposed dissolution model is applied to investigate the dynamic of CO$_2$ droplet in a channel at storage depth of 1000 m. Simulations were performed in a two-dimensional domain with the boundary condition of periodic in vertical direction and full bounceback for the solid channel wall. A droplet is released from rest to rise with dissolution at the bottom of the channel.

The thermo-fluid states of CO_2 and water for the simulations are T=288K and P=9.81MPa, which simulate to the state of CO_2 geological storage condition at a depth of 1000 m. The parameters of physics and LBM used in the simulation are the same of those used in Chapter 4. The details can be found from Table 4.1.

5.3 Effect of Eo on deformation and rising velocity with and without dissolution

The Eotvos number (Eo) is the ratio of buoyancy force to surface tension force, which is used to characterize the droplet shape and defined as $g\Delta\rho d_e^2/\sigma$, where g is the gravitational acceleration and σ is the surface tension. In order to investigate the effect of Eo on deformation and rising velocity with and without dissolution, a series of interaction strength G_{12} and gravitational factor g were selected to obtain different Eo numbers. In this study, the Eo number is in the range of 0.1 to 67.7.

The droplet deformation at low Eo number, Eo=0.1, is shown in Figure 5.1. Figure 5.1(a) illustrates that without dissolution the droplet shape is spherical, which confirms the results by Gupta et al. [186]. Figure 5.1(b)-(f) show the droplet snapshots from rest to rise with dissolution at different times. The normalized time, t^*=t/t_o, where t_o=L_x^2/G_d. L_x is the channel horizontal width, Lx=100, G_d is the diffusion potential strength of Eq.4.4. It was found that the dissolution droplet retains a spherical shape. However, the droplet size shrinks with time. At $t^* = 8$, the effective droplet diameter reduces to 65.5% of the initial one. In addition, the upper solution layer of the droplet is thinner than that at the bottom of the droplet. This is due to advection accelerating the movement of the solution from the top of the droplet. The solution accumulates at the bottom of the droplet.

The rising velocities of the droplet with and without dissolution are shown in Figure 5.2. It shows that rising velocity increasing gradient of the dissolving droplet is greater than that without dissolution. After reaching the maximum velocity, the droplet without dissolution retains the terminal velocity. However, in the case of the droplet with dissolution, there is no terminal velocity. The rising velocity gradually reduces after t^*=1.0, which is because of the reduction on droplet size, as shown in Figure 5.1.

5.3. Effect of Eo on deformation and rising velocity with and without dissolution

Figure 5.1: Effect of dissolution on droplet deformation at low Eo number, Eo=0.1. (a)Without dissolution at t^*=1, 2, 4, 6 and 8. (b)-(f) With dissolution at t^*=1, 2, 4, 6 and 8. C is the concentration of CO_2.

The LBM simulation results at Eo=0.58 is shown in Figure 5.3. Without dissolution, the droplet shape is an oblate ellipsoidal cap, as shown in Figure 5.3(a). In comparison with Figure 5.1, it can be seen that the droplet shape changes from spherical to an oblate ellipsoidal cap with the increase of the Eo number. Figure 5.3(b) to (e) show that the dissolving droplet forms an oblate ellipsoidal cap and shrinks with time. The effect of dissolution on the droplet deformation is insignificant. In comparison with the simulation results at Eo=0.1, as shown in Figure 5.1, the length of the solution tail at Eo=0.58 is longer than that at Eo=0.1.

The effect of dissolution on droplet deformation at Eo=67.69 is shown in Figure 5.4. A higher Eo number is obtained by changing the initial droplet diameter to 80 lattices. Figure 5.4(a) shows that the droplet shape without dissolution is shaped like a bullet. Figure 5.4(b)-(d) show the deformation and concentration distribution with dissolution at different times. It indicates that at large Eo number, the effect of dissolution on the
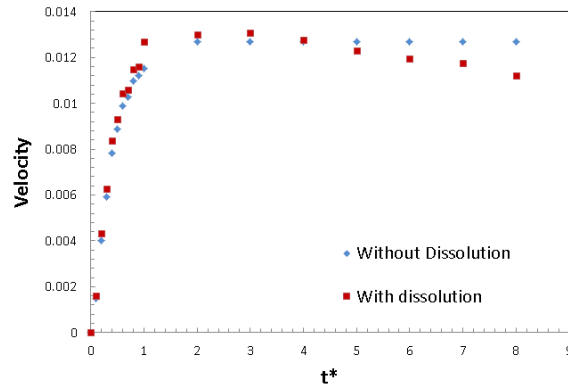
Figure 5.2: Droplet rising velocity changes with the normalized time.

droplet deformation is significant. Simultaneously, the solution tail is elongated by the buoyancy. The breakup of the solution tail occurred at t*=3.0, resulting in the oscillation of the solution tail.

Therefore, the deformation of the droplet with dissolution is related to the *Eo* number. At a low *Eo* number, the effect of dissolution on the droplet deformation is not significant. However, at a higher *Eo* number, namely *Eo*>67.69, the shape of the dissolving droplet significantly changes with time, due to the oscillation and the breakup of the solution tail. In addition, unlike the droplet rising up without dissolution, it is difficult to define the terminal velocity of the droplet rising up with dissolution. The rising velocity of the dissolving droplet gradually reduces with time after reaching the maximum velocity, which is due to the reduction in the droplet size.

5.4   Wall effect on CO$_2$ dissolution

The performance of a droplet rising up in a channel is affected by the relative size of droplet to channel. As the channel width approaches to the initial droplet diameter, the deformation of the droplet is restricted by the channel width. As the channel width increases, the droplet rising up in a channel approaches to the free rising up.

The ratio of the initial droplet diameter, D_o, to the channel width, L_x, is defined by $M = D_o/L_x$. In order to investigate the effect of channel width on the performance of the rising-up droplet with dissolution, in terms of the droplet shape, shrinking rate and rising velocity, a series of simulations were carried out at M=1, 0.67, 0.5 and 0.3. The
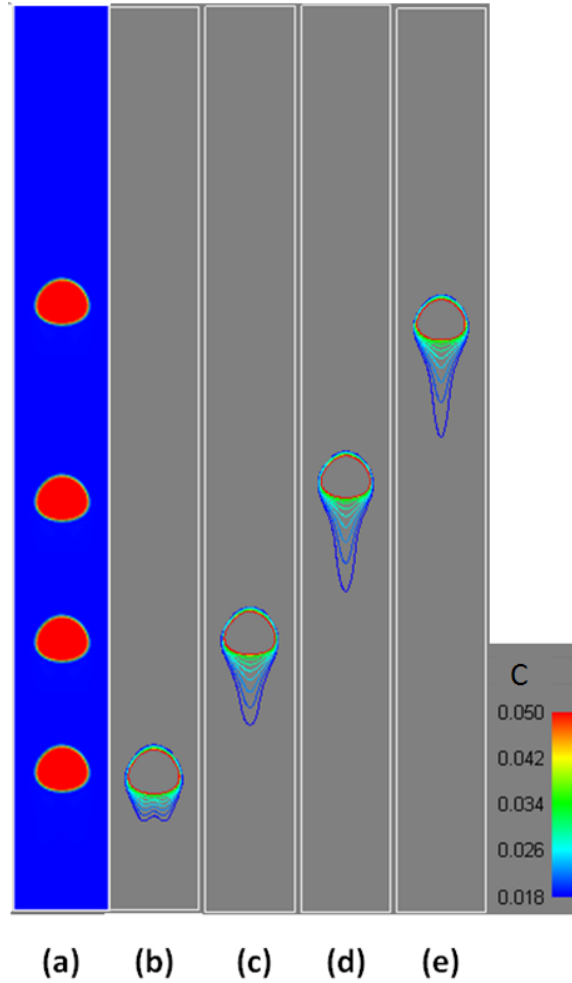
Figure 5.3: Effect of dissolution on droplet deformation at Eo=0.58. (a)Without dissolution at t*=0.5, 1.0, 1.5 and 2.0, (b)-(e) With dissolution at t*=0.5, 1.0, 1.5 and 2.0. C is the concentration of CO$_2$.

droplet was initialized at the bottom of the channel. The droplet diameter was fixed to be 100 lattices in all of these cases. The channel length was set to be 2000 lattices. The top and bottom boundary condition was the periodic boundary condition, which provides a sufficient domain in which to investigate the droplet behavior.

5.4.1 Droplet shape

The droplet concentration distribution and deformation at different time steps under M=1 (L_x=100 lattices) is shown in Figure 5.5. Initially, the droplet blocks the entire cross-section of the channel, as shown in Figure 5.5(a). Eventually, the droplet is confined by the walls and stretched as a bullet shape. The droplet rises up along the wall. The CO$_2$
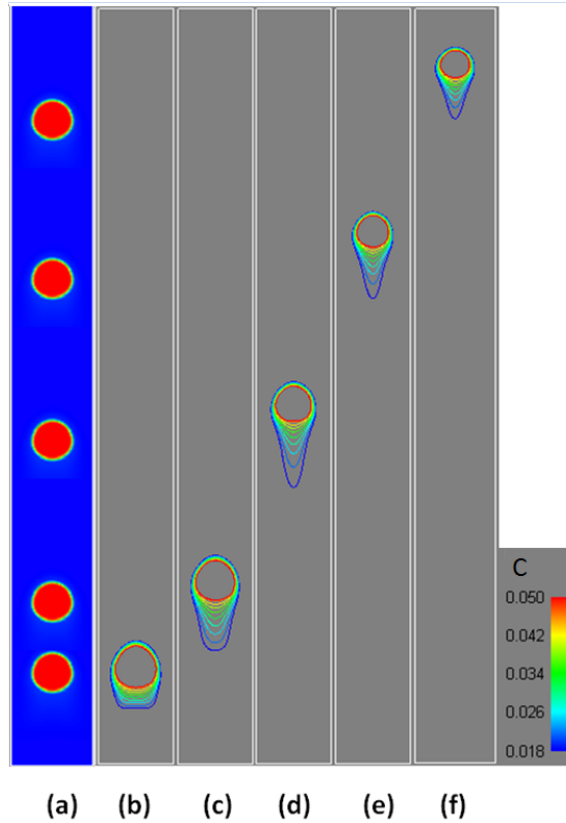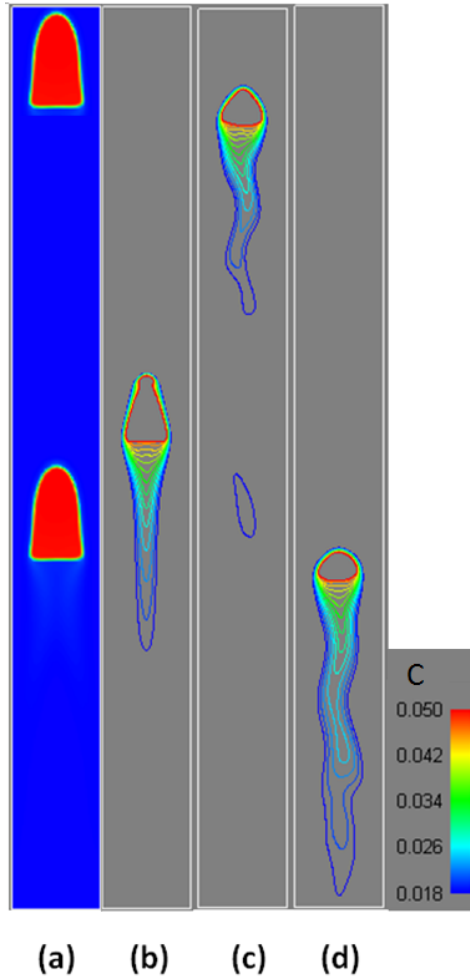
Figure 5.4: Effect of dissolution on droplet deformation at high Eo number, Eo=67.69 (a)Without dissolution at t*=1.0 and 3.0, (b)-(d) With dissolution at t*=1.0, 3.0 and 4.0. C is the concentration of CO$_2$.

solution tail is symmetrical and scissors-type.

As M reduces to 0.67 (L$_x$=150 lattices), as shown in Figure 5.6, the rising up droplet detaches from the wall. There is space for the development of the droplet in the horizontal direction, in comparison with the case at M=1. The droplet shape changes to an oblate ellipsoid cap before t*=4.0. After that, the droplet breakup is observed. The droplet is unstable and the solution tail is no longer symmetrical. At t*=5.0, the droplet breaks up into several small droplets and these dissolve into the water.

At M=0.5, the droplet begins to wobble from t*=3.0, as shown in Figure 5.7(d). Consequently, the droplet breaks up into several droplets at t*=4.0, which is faster than that in the case of M=0.67. The same phenomenon is observed in the case at M=0.3, as shown in

5.4. Wall effect on CO_2 dissolution
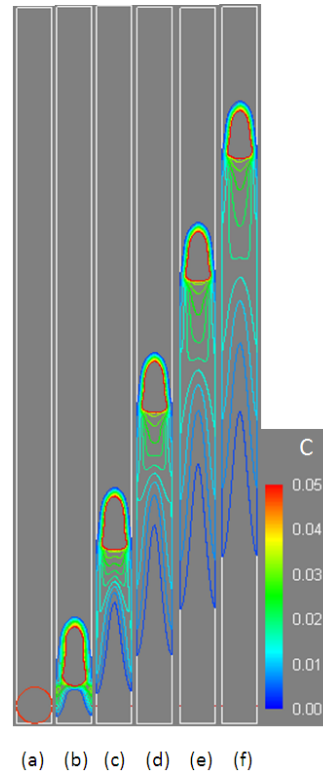
Figure 5.5: The droplet concentration distribution at M=1. (a)-(f): t^*=0, 1, 2, 3, 4 and 5. C is the concentration of CO_2.

Figure 5.8.

Therefore, the simulation results indicate that the performance of the rising droplet in the channel is strongly affected by the channel width. In this study, as the channel has sufficient space for droplet deformation in a horizontal direction, known as M≤0.67, the droplet shape changes into an oblate cap. In addition, wobbling and breakup of the droplet are occurred. In contrast, at M≥0.67, the droplet rises up along the wall and the shape of droplet is stretched.

The aspect ratio is used for discussion of droplet deformation, which is determined by the ratio of the major to minor axis of the droplet, which is defined by D_x/D_y, where D_x and D_y are taken as the vertical and horizontal axis of the droplet, respectively, as shown in Figure 5.9. The aspect ratio distributions under different Ms at the time steps before the droplet breaks up is shown in Figure 5.10. It was found that the aspect ratio distribution range increases with the decrease of M or the increase of channel width. For example, at M=0.3, the aspect ratio is in the range of 1.0-3.3. As a comparison, at M=1, the aspect ratio remains stable at approximately 0.5.
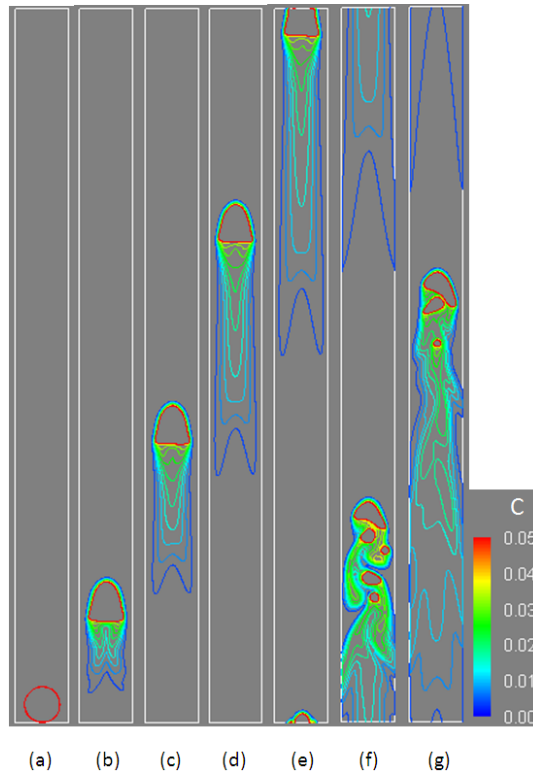
Figure 5.6: The droplet concentration distribution at M=0.67. (a)-(g): t*=0, 1, 2, 3, 4, 5 and 6. C is the concentration of CO$_2$.

5.4.2 Shrinking rate

The dimensionless effective diameter (D*=D$_e$/D$_o$) varies with time is shown in Figure 5.11. For the deformed droplet, the effective diameter D$_e$ is used to describe the shrinking of droplet at each time step, which is defined by D$_e$=$\sqrt{\frac{4A}{\pi}}$, where A is the cross area of the droplet. The shrinking rate is defined by dD*/dt

The simulation results indicate that when the channel width is not great enough for droplet deformation, such as M=1, the droplet shrinking rate is restricted and smaller than the other cases (M=0.67, 0.5 or 0.3). This is due to a reduction in the surface area of the mass transfer, when the droplet rises along the wall. However, when the droplet detaches from the wall, the shrinking rate is not significantly affected by the channel width, for example at M=0.67, 0.5 and 0.3, the difference in the droplet shrinking is negligible, as shown in Figure 5.11.
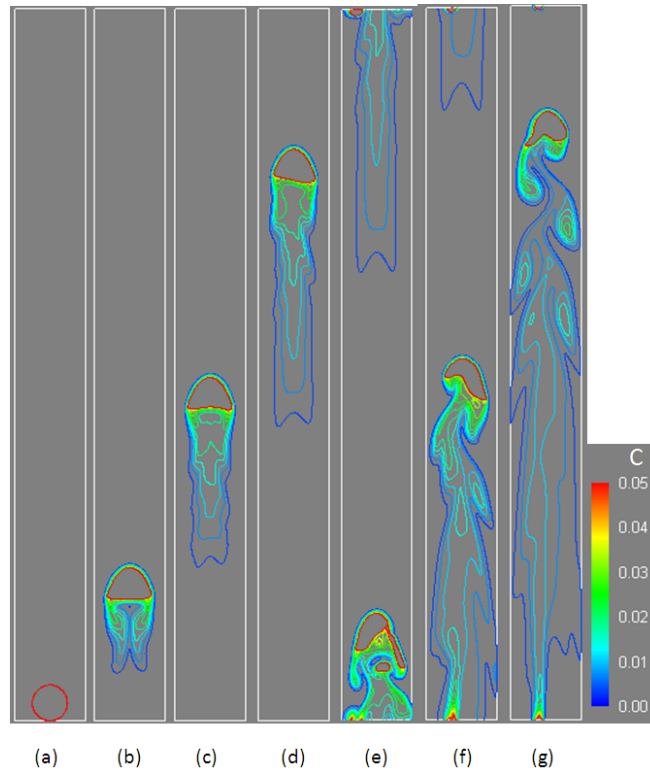
Figure 5.7: The droplet concentration distribution at M=0.5. (a)-(g): t*=0, 1, 2, 3, 4, 5 and 6. C is the concentration of CO$_2$.

5.4.3   Rising velocity

The rising velocities of droplets in channels with different widths are shown in Figure 5.12. It was found that the rising velocity increases with the decrease of M. Wobbling of droplets is observed at small Ms, which is due to the deformation and breakup of the droplet. With the exception of the velocity oscillation, the major trend shows that rising velocity increases sharply in the brief initial period and then gradually declines with time for all of the cases. Before the breakup of the droplets, the maximum velocity for these four cases are 0.037 (M=1), 0.057 (M=0.67), 0.068 (M=0.5) and 0.079 (M=0.3), respectively. The maximum velocity at M=0.3 is approximately 2.12 times of that at M=0.1.

From the simulations, it is observed that the performance of dissolution of droplet in the channel is related with the diameter ratio, $M = D_o/L_x$. In the case of a given droplet, a smaller channel width can successfully reduce the rising up velocity of CO$_2$ in geoformation, and consequently restrict the penetration of the stored CO$_2$. In addition, the shrinking

Figure 5.8: The droplet concentration distribution at M=0.3. (a)-(f): t*=0, 1, 2, 3, 4 and 5. C is the concentration of CO$_2$.

rate of the droplet is reduced as the droplet rises along the wall. In contrast, as there is enough space for the deformation of the droplet, the shrinking rate is independent of the channel width.

5.5 CO$_2$ droplet dissolution in inclined channel

In this section, comparison studies are carried out using a series of numerical simulations of CO$_2$ droplet dissolution in the inclined channels with different tilt angles, which are set to be θ=10°, 30°, 60°, and 90°, respectively, as seen in Figure 5.13 and Figure 5.14. The channel width Lx and the arrangement of the droplet are as the same as those in Section 5.3 and Section 5.4. The channel length increases to 2000 lattices. The dimensionless time t* is the ratio of the simulation time to D_o^2/G_d.

Figure 5.9: Schematic of the major and minor axis of non-spherical droplet.
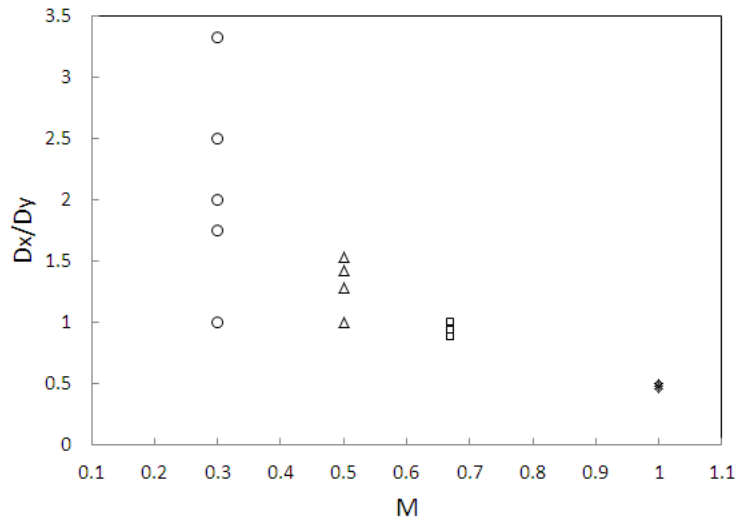
Figure 5.10: Aspect ratio distribution at time step t^*=1, 2, 3 and 4, for the cases with M=1, 0.67, 0.5 and 0.3.

5.5.1 Droplet shape

At M=1, the droplet rises up attaching to the up channel wall in the cases with θ=10°, 30°, and 60°, as shown in Figure 5.13. The droplet does not block the cross-section of the channel, as θ reduces to 60°. The change in channel tilt angle changes the shape of the droplet. With the decrease in tilt angle, the droplet shape changes from a bullet to an ellipse. In addition, the solution tail is as symmetrical as that at θ<90°. The length of the dissolution tail reduces with the decrease of the tilt angle at the same time.

At M=0.3, as shown in Figure 5.14, as $\theta \leq$30° the droplet rises up attaching to the upper wall. In contrast, as $\theta \geq$30° the droplet detaches from the wall and wobbles. The breakup of the solution tail is observed at θ=60°.

Figure 5.11: The effective diameter varies with time at different M.

5.5.2 Rising velocity

The droplet rising velocities in the inclined channels with different diameter ratio Ms are shown in Figure 5.15. It indicates that the rising velocity of the droplet reduces with the decrease of the tilt angle of the channel, regardless of the values of M. For example, at M=1, the maximum rising velocities of droplet at θ=10°, 30° and 60° are 45.7%, 79.2% and 97.6% of that at θ=90°.

The fluctuations of the rising velocity of the droplet are observed in all of the cases except that at θ=10° and M=1.0, which is due to the deformation and breakup of the droplet. The simulation results demonstrate that the fluctuation of the droplet rising velocity is small in the cases with small tilt angles.

5.5.3 Shrinking rate

Effective diameter shrinking with time in the channels with different tilt angles is shown in Figure 5.16. It can be seen that the shrinking rate decreases with the reduction of the channel tilt angle and the relationship is not linear. As M=0.3, the shrinking rate ($\frac{D_e/D_o}{t}$) of the droplet in the channel with θ=10° is 44.13% of that with θ=90°. As M=1.0, the shrinking rate of the droplet in the channels with θ=10° is of 98.77% of that with θ=90°. There, with the decrease of M, the tilt angle has a significant effect on the shrinking rate.
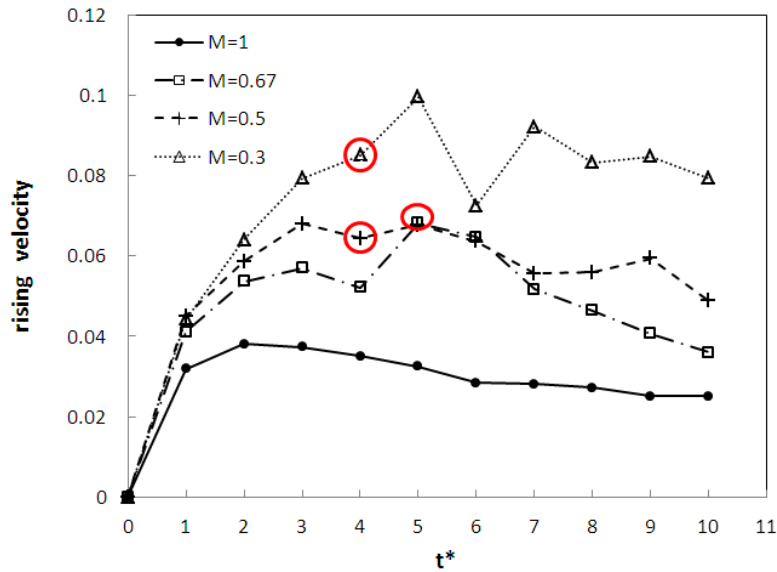
Figure 5.12: The droplet rising velocity varies with time at different M. Red circles denote the break up of droplet.

In comparison with the other cases, the case at M=0.3 and $\theta=90°$ has the largest shrinking rate.

5.5.4   The relationship between Eo and Re

The Re and Eo at each time for the cases at different Ms and θs are plotted in Figure 5.17. Re number is defined by, $Re = U_t D_e/\nu$, where U_t is the rising velocity of CO_2 droplet. D_e is the effective diameter and ν is the kinematic viscosity of water. Eo is defined as, $Eo = g\Delta\rho d_e^2/\sigma$, where g is the gravitational acceleration and σ is the surface tension. The Re number and the Eo number are in the range of 20-600 and 20-48, respectively, in this study.

It was found that with the increase of M, the Eo number increases and the Re number decreases. With the increase of the channel tilt angle, the Eo number increases and the Re number reduces. The wobbling of the droplet is observed at the region with the Re number of 300-600 and the Eo number of 20-43, as shown in the elliptical area of Figure 5.17. A larger shrinking rate is also obtained in this region, as shown in Figure 5.16

113
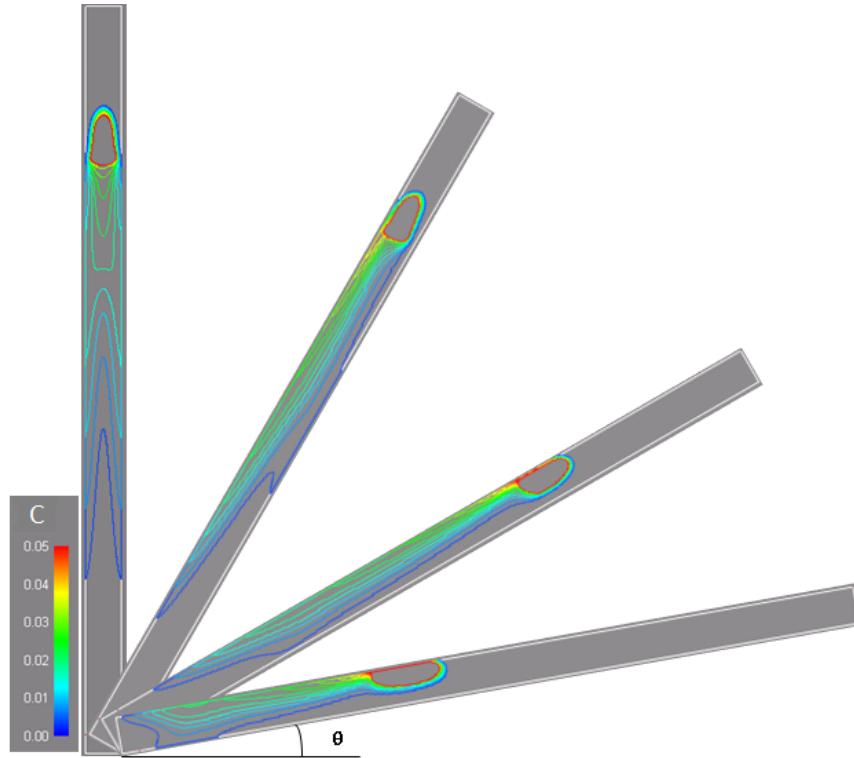
Figure 5.13: The snaps of CO$_2$ droplet concentration contours distributions in the channel with different tilt angles under M=1 at t*=5.

5.6   Dissolution of two CO$_2$ droplets in the channel

In order to investigate the dissolution of two droplets in the channel, the numerical simulations are carried out in the channels with different Ms, which are set to be M=1 and M=0.3, respectively. The channel length is set to be 40000. Two droplets are initially located at and x=L$_x$/2, y=50 and x=L$_x$/2,y=450, respectively. The initial diameters of two droplets are 100 lattices.

At M=0.3, the simulation results indicate that the following droplet gradually closes to the upper one, as shown in Figure 5.18. At t*=2, the following droplet flows into the solution tail of the upper droplet. It can be seen that the shapes of two droplets are different. The deformation of the following droplet is caused by the downward vortex of the upper droplet solution tail, which is consistent with the streamlines, as shown in Figure 5.21 (b). Two droplets wobble at a different frequency. Consequently, the following droplet merges into the upper droplet at t*=3. The solution tail of the merged droplet is asymmetric and wobbling.

5.6. Dissolution of two CO$_2$ droplets in the channel
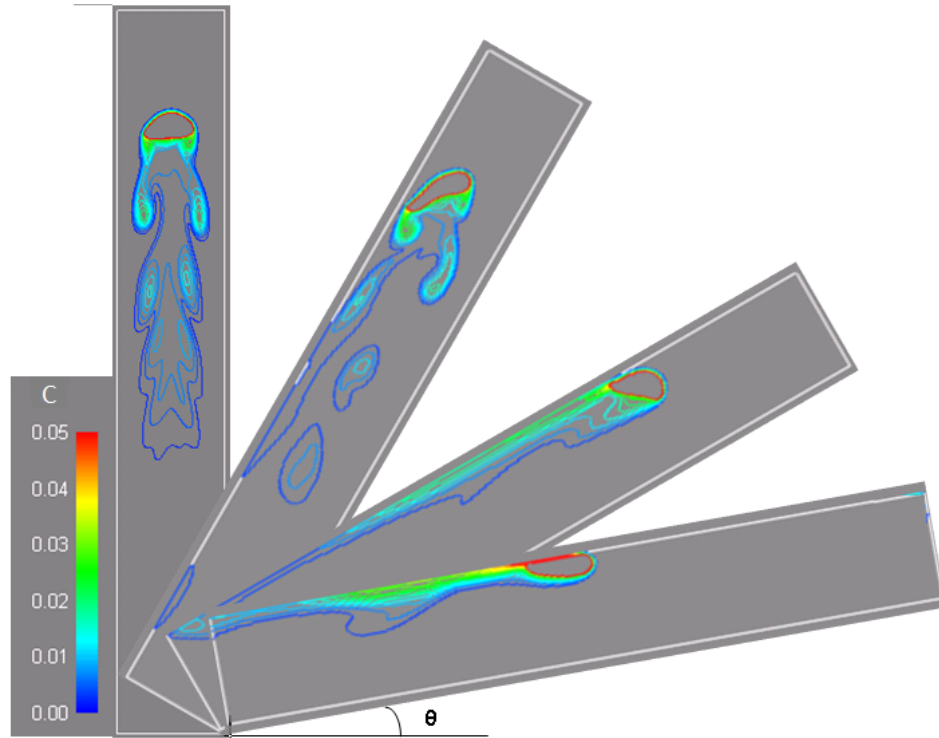
Figure 5.14: The snaps of CO$_2$ droplet concentration contours distributions in the channel with different tilt angles under M=0.3 at t*=3.

The rising velocities of the droplets are shown in Figure 5.19 (a). The red circle in Figure 5.19 denotes the time that the following droplet merges into the upper one. It can be seen that before the following droplet merges into the upper one, the rising velocity of the following droplet is larger than that of the upper one. In addition, the rising velocities of these two droplets are greater than that of a single droplet dissolution before t*=3. The effective diameter of the following droplet is larger than that of the upper one before the droplets merging, as shown in Figure 5.19 (b). In addition, the shrinking rate of the following droplet is smaller than the upper one, which is due to a smaller concentration gradient near the interface of the following droplet and the smaller surface area.

At M=1.0, the coalescence of two droplets is not observed until t*=8, as shown in Figure 5.20. At t*=2, the following droplet approaches the solution field of the upper droplet. The solution tail of the droplets is symmetrical. The streamlines at t*=4 demonstrates that there is no vortex in the droplet solution, as shown in Figure 5.21 (c). Therefore, the deformation of the following droplet is insignificant in comparison with that at M=0.3.

The shrinking rate of the upper droplet is larger than that of the following one, which are

5.6. Dissolution of two CO_2 droplets in the channel
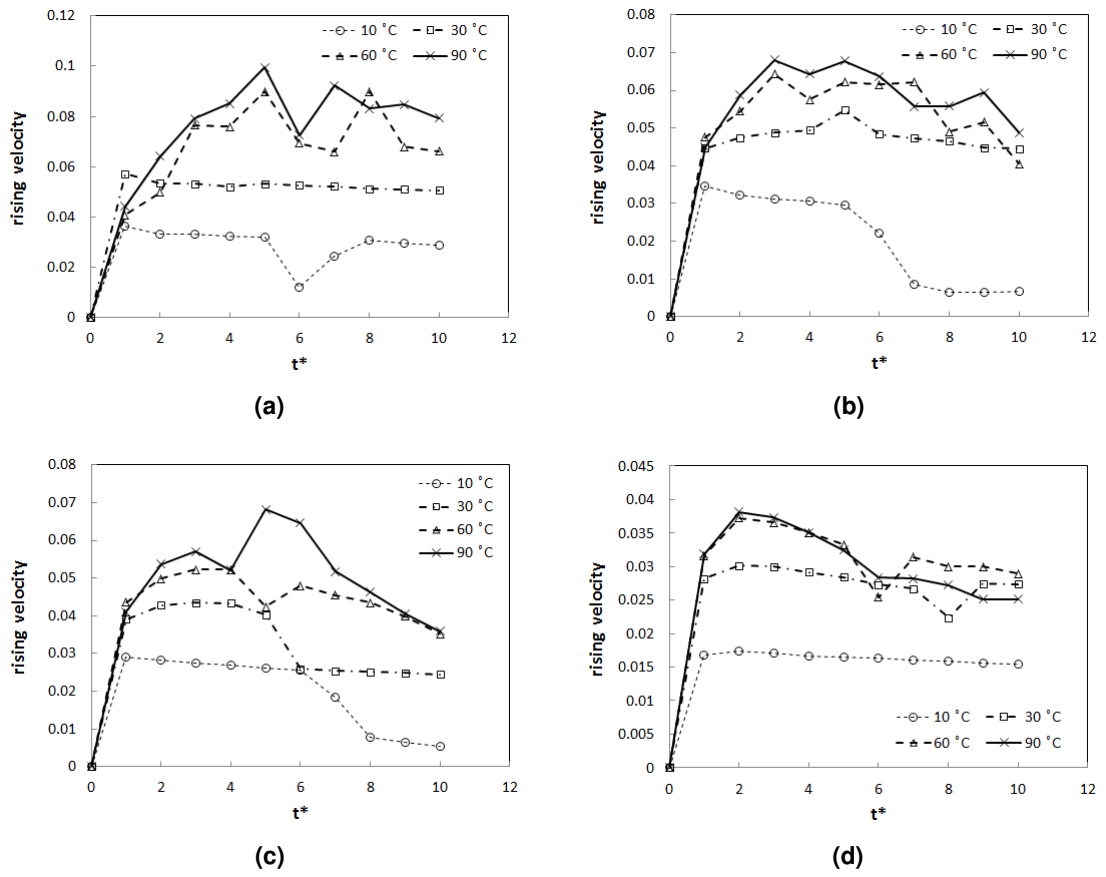
Figure 5.15: Droplet rising velocities change with time in the channel with different tilt angles, including θ=10°, 30°, 60° and 90°, respectively, at (a)M=0.3; (b)M=0.5; (c)M=0.67; (d)M=1.0;

0.02 and 0.011, respectively, as shown in Fig5.22 (b). This is due to the concentration gradient on the interface of the following droplet being smaller than that of the upper droplet. Compared with the dissolution of a single droplet, the shrinking rate of the single droplet is larger than those of both the upper droplet and the following droplet. In addition, the rising velocity of the following droplet is slightly larger than that of the upper droplet, as shown in Fig5.22 (a). The difference in the rising velocities between two droplets and a single droplet dissolution at M=1 is insignificant.

Therefore, the shrinking rate of each droplet in the dissolution of the two droplets is not the same as that in the dissolution of a single droplet in these two cases, M=1 and M=0.3. In addition, the shrinking rate of the upper droplet is larger than that of the following droplet after the following droplet flows into the solution field of the upper droplet.

The coalescence of two droplets is observed in the case at M=0.3. Before the following
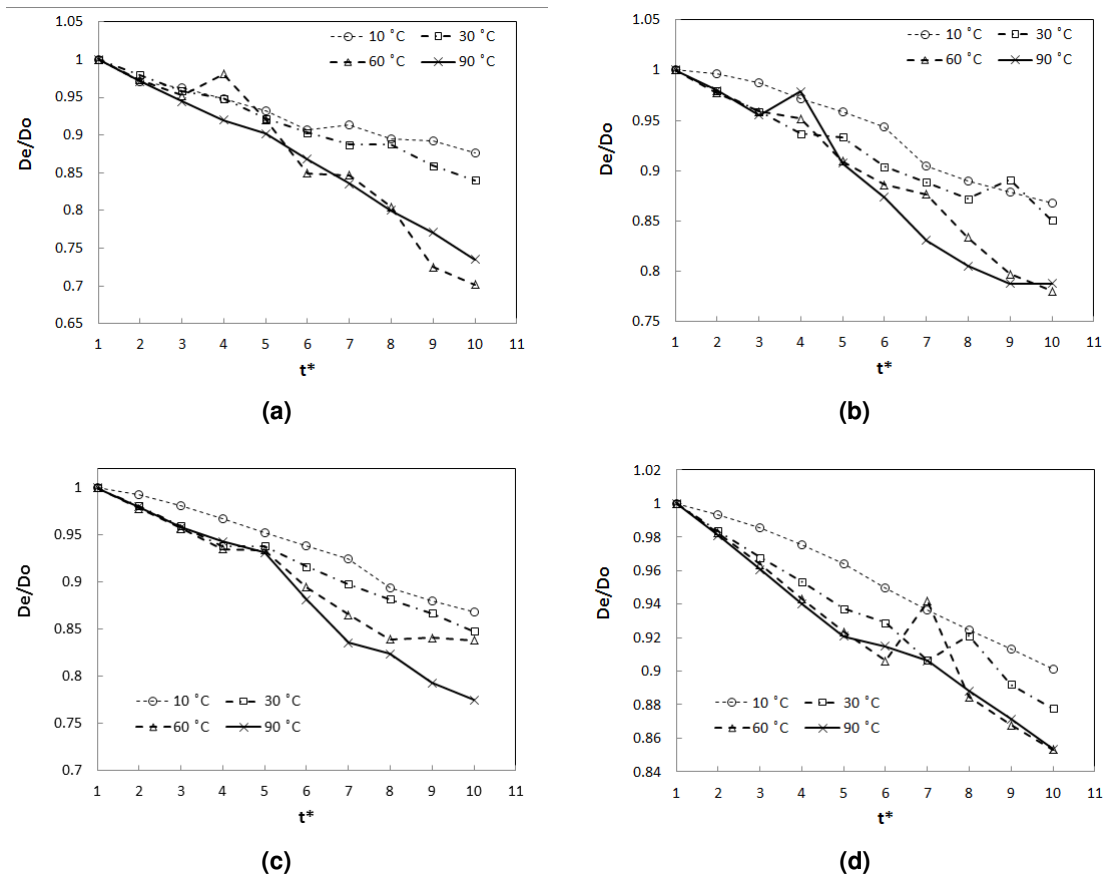
Figure 5.16: Effective diameter changes with time in the channels with different tilt angles at (a)M=0.3; (b)M=0.5; (c)M=0.67; (d)M=1.0;

droplet merges to the upper droplet, the rising velocity of the following droplet is significantly larger than that of a single droplet dissolution. This is due to the deformation of the following droplet being accelerated by the vortex of solution tail of the upper droplet. However, at M=1, there is no vortex existing in the flow fluid of the solution. The difference in rising velocity between the dissolution of two droplets and the single droplet is negligible. The shrinking rate of the dissolution of two droplets is smaller than that of the dissolution of a single droplet.
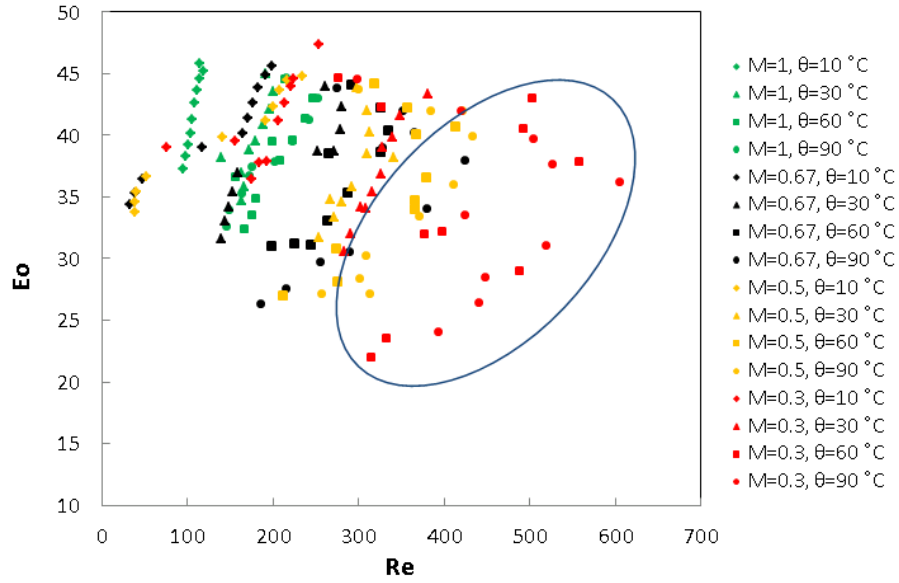
Figure 5.17: *Re* and *Eo* panel at different M and θ.

5.7 Conclusion

The developed LBM multicomponent dissolution model is applied to investigate the performance of CO_2 droplet dissolution in water in the channels at pore scale, in terms of the droplet shape, shrinking rate, droplet concentration distribution and rising velocity.

By the simulating the dissolution of rising droplet at different *Eo* numbers, it was found that the deformation of the rising droplet with dissolution is related to the *Eo* number. At a low *Eo* number, such as *Eo*=0.1 and 0.58, the deformation of droplet resulting from the dissolution is insignificant. At *Eo*>67.69, the shape of the dissolving droplet changes significantly with time, due to oscillation and the breakup of the solution tail. In addition, it is difficult to achieve a terminal velocity of the dissolving droplet, due to the changes in droplet size.

The effect of the wall on the performances of the dissolution of droplet has been investigated. In the case of a given droplet, a smaller channel width can successfully reduce the rising up velocity of CO_2 in geoformation; consequently, it restricts the penetration of the stored CO_2. In addition, the shrinking rate of the droplet is reduced, due to the decrease in the surface area of the mass transfer. As the channel width increases to provide enough space for the deformation of the droplet, such as M≤0.67, the shrinking rate is independent of the channel width.
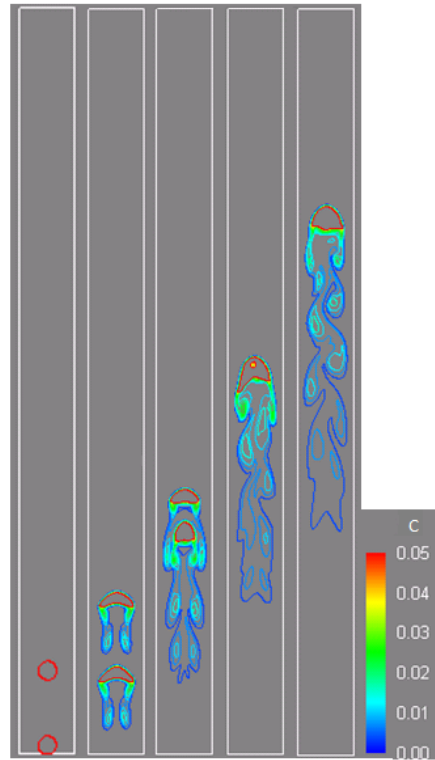
Figure 5.18: Concentration distribution of two droplets dissolution in the channel under M=0.3 at t*=0, 1, 2, 3 and 4.

The simulations of the dissolution of a rising droplet in inclined channels with different tilt angles demonstrate that the shrinking rate reduces with the decrease in the channel tilt angle. The channel at $\theta=90°$ has the largest shrinking rate. The rising velocity of CO_2 reduces with the decrease of the tilt angle. Therefore, the penetration of CO2 into water is reduced in channels with a small tilt angle. Wobbling and breakup of the solution tail are prone to occur in a channel with smaller M and a larger tilt angle. The relationship between the *Eo* and *Re* number is investigated. In this study, the wobbling of the droplet is observed at the region with a *Re* number of 300-600 and an *Eo* number of 20-43, where a large shrinking rate is obtained.

A comparative study of the dissolution of two droplets and of a single droplet are carried out in the channels at M=1 and M=0.3, respectively. It was found that in both cases, the shrinking rate of the upper droplet is larger than that of the following droplet after the following droplet flows into the solution field of the upper droplet. The rising velocity of the following droplet is larger than that of the upper droplet, and larger than that of the single droplet. However, the performances of the dissolution of two droplets are different
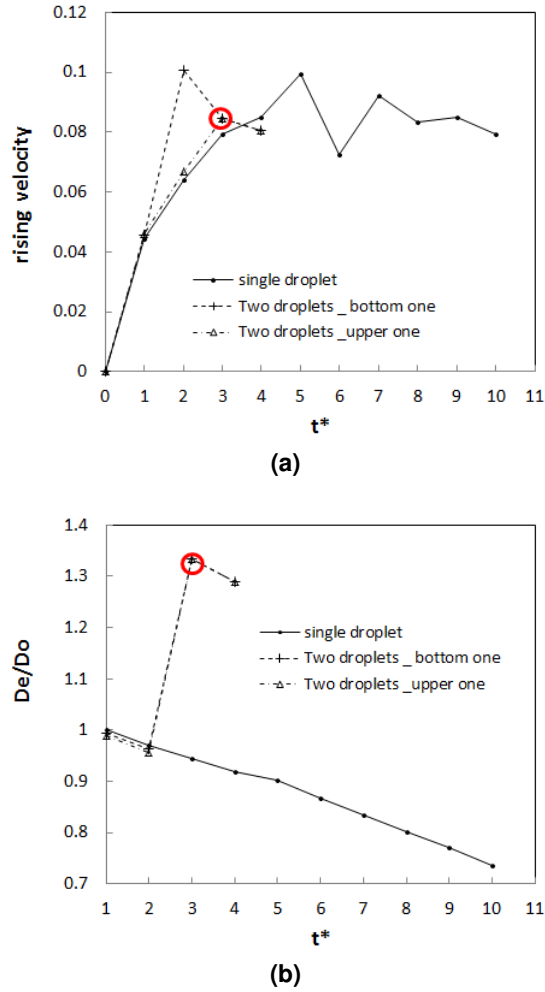
Figure 5.19: The comparison of the dissolution of a single droplet and two droplets at M=0.3. (a) Velocity profile; (b) Effective diameter profile

in the different channels. The deformation of the following droplet is significant in the channel with M=0.3, consequently, the coalescence of two droplets is observed. At M=1, the difference in rising velocity between the dissolution of two droplets and the single droplet is negligible. The shrinking rate of the dissolution of two droplets is smaller than that of the dissolution of a single droplet. It is observed that the wall has a dominant effect on the shrinking of a droplet and rising velocity.

Furthermore, after CO_2 dissolves in water, the density of the CO_2 solution is denser than the water. Consequently, the CO_2 solution flows down to the seafloor due to the gravity and continues penetrating into the marine sediment. Therefore, the mechanism of the CO_2 solution penetration in geoformation is further investigated in the Appendix.
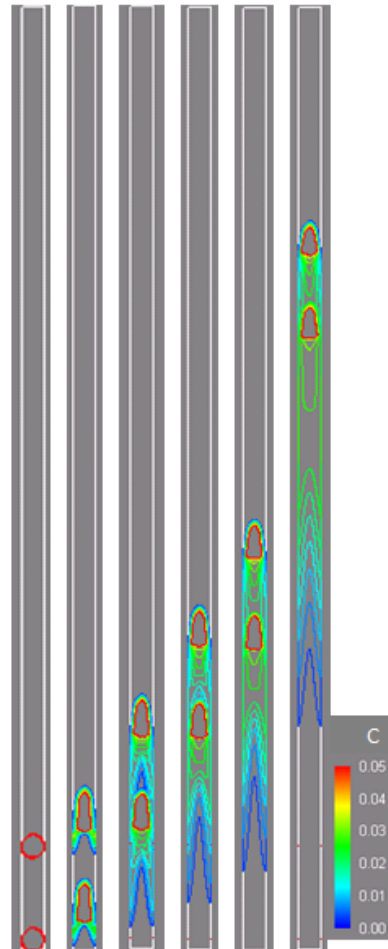
Figure 5.20: Concentration distribution of two droplets dissolution in the channel under M=1.0 at t^*=0, 1, 2, 3, 4 and 8.
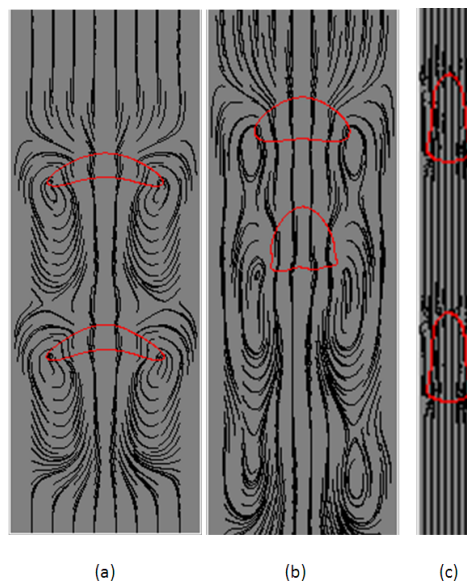
Figure 5.21: Velocity streamlines of two droplets in the channel. (a) M=0.3, t^*=1; (b) M=0.3, t^*=2; (c) M=1.0, t^*=4.

121
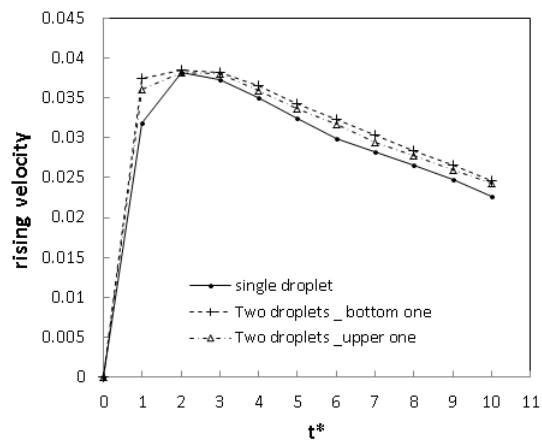
(a)
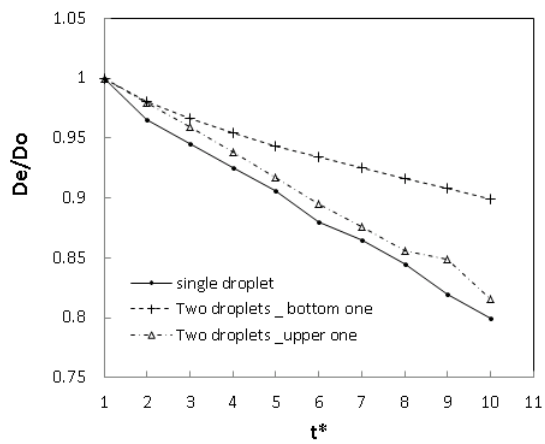
(b)

Figure 5.22: The comparison of the dissolution of a single droplet and two droplets at M=1.0. (a) Velocity profile; (b) Effective diameter profile

Chapter 6

An improved lattice Boltzmann scheme for multiple fluid flow

6.1   Introduction

Based on the reviews in Section 3.8, it is recognized that the numerical stability related to the spurious velocity is an challenge of LBM MCMP in the large density ratio simulations. In this chapter, an improved scheme is developed, based on the non-linear implicit trapezoidal lattice Boltzmann scheme (referred to as implicit scheme in this study) proposed by Nourgaliev et al. [1]. The implicit scheme successfully reduced the spurious velocity in multiphase LBM simulations, however it apparently increases the CPU time consumption per simulation step due to the iteration calculation. In this study, the improved scheme preserves the trapezoidal rule central approximation and avoids CPU time consumed on the iteration calculation. This improved scheme directly evaluates the particle's velocity in the equilibrium state function, instead of calculating the particle's distribution function by iteration in the original implicit scheme.

This chapter is organized as follow. The improved scheme is introduced in Sec.6.2. The applications of the improved scheme in multiphase and multicomponent simulations are illustrated in Section 6.3.1 and Section 6.3.2, respectively. The comparison study between explicit and improved scheme are investigated in terms of the density ratio and spurious velocity. Finally, the conclusions are summarized in Section 6.4.

6.2   The improved LBM scheme

The improved scheme proposed in this study is derived from non-linear implicit trapezoidal lattice Boltzmann scheme [1]. In the implicit scheme, both of the local and next time step's equilibrium distributions are used to calibrate the collision operator [1] [206]. The collision operator is evaluated by a trapezoidal rule using the central difference approximation. The rule is described by

$$f_i^\sigma(x+e_i\Delta t, t+\Delta t) - f_i^\sigma(x,t) = -\frac{[f_i^\sigma(x,t) - f_i^{\sigma,eq}(x,t)]}{2\tau_\sigma^I}$$
$$-\frac{[f_i^\sigma(x+e_i\Delta t, t+\Delta t) - f_i^{\sigma,eq}(x+e_i\Delta t, t+\Delta t)]}{2\tau_\sigma^I} \quad (6.1)$$

The symbols in the above equation are the same with that of the explicit scheme introduced in Section 3.5, except the relaxation time. Note that the relaxation time in implicit LBM scheme is defined by $\tau_\sigma^I = \frac{1}{c_s^2}\upsilon_\sigma$ [206]. In order to distinguish the relaxation time in the explicit scheme and that in implicit scheme, in this chapter, τ_σ^E denotes the relaxation time of explicit scheme in Eq.3.13, and $\tau_\sigma^E = \tau_\sigma^I + \frac{1}{2}$. It is apparent that the collision operators on the right hand sides of Eq.3.13 and Eq.6.1 are different. In the explicit scheme, the distribution function at $t+\Delta t$ can be directly solved by Eq.3.13. However, in the implicit scheme, Eq.6.1 is implicit non-linear equation, since the equilibrium function $f_i^{\sigma,eq}(x+e_i\Delta t, t+\Delta t)$ is related to the distribution function $f_i^\sigma(x+e_i\Delta t, t+\Delta t)$. In the original implicit scheme, the iterative algorithm is used to solve the distribution function at $t+\Delta t$. It is noticed that the consumption of the numerical simulation time increases.

With the effort to the implicit scheme, Eq.6.1 is rearranged and the distribution function is obtained by

$$f_i^\sigma(x+e_i\Delta t, t+\Delta t) = \frac{1}{2\tau_\sigma^I + 1}[B_i^\sigma + f_i^{\sigma,eq}(x+e_i\Delta t, t+\Delta t)] \quad (6.2)$$

where $B_i^\sigma = (2\tau_\sigma^I - 1)f_i^\sigma(x,t) + f_i^{\sigma,eq}(x,t)$. B_i^σ gathers all the terms at time step t and is a constant at time step $t+\Delta t$. The equilibrium function $f_i^{\sigma,eq}$ is described by Eq.3.14, as the same function as that used in the explicit scheme.

Instead of solving Eq.6.1 by iteration as the original implicit scheme, substituting Eq.6.2

6.2. The improved LBM scheme

to Eq.3.18 and Eq.3.17, the equilibrium velocity is obtained by

$$u_\sigma^{eq} = \frac{\sum_\sigma \sum_i f_i^{\sigma,eq} e_i / \left[\tau_\sigma^I(2\tau_\sigma^I + 1)\right]}{\sum_\sigma \rho_\sigma / \tau_\sigma^I} + \frac{\sum_\sigma \sum_i B_i^\sigma e_i / \left[\tau_\sigma^I(2\tau_\sigma^I + 1)\right]}{\sum_\sigma \rho_\sigma / \tau_\sigma^I} + \frac{\tau_\sigma^I F_\sigma}{\rho_\sigma} \quad (6.3)$$

where F_σ is the total force acting on the σth component. The fluid density, ρ_σ, is assumed invariance during the collision process. Therefore, B_i^σ and F_σ are invariance on time step $t + \Delta t$.

Substituting $f_i^{\sigma,eq}$ in Eq.6.3 by Eq.3.14, the first term on the right hand side of Eq.6.3 is described by

$$\frac{\sum_\sigma \sum_i f_i^{\sigma,eq} e_i / \left[\tau_\sigma^I(2\tau_\sigma^I + 1)\right]}{\sum_\sigma \rho_\sigma / \tau_\sigma^I} = \frac{\sum_\sigma 1 / \left[\tau_\sigma^I(2\tau_\sigma^I + 1)\right] \sum_i \rho_\sigma \omega_i e_i \left[1 + 3\frac{e_i \cdot u_\sigma^{eq}}{c^2} + \frac{9}{2}\frac{(e_i \cdot u_\sigma^{eq})^2}{c^4} - \frac{3}{2}\frac{u_\sigma^{eq} \cdot u_\sigma^{eq}}{c^2}\right]}{\sum_\sigma \rho_\sigma / \tau_\sigma^I}$$

$$(6.4)$$

Since $\sum_i w_i e_i = 0$, $\sum_i w_i e_i^3 = 0$, $\sum_i w_i e_i^2 = 1/3$ and c=1, second-order term of equilibrium velocity is eliminated. The following equation is obtained

$$\frac{\sum_\sigma \sum_i f_i^{\sigma,eq} e_i / \left[\tau_\sigma^I(2\tau_\sigma^I + 1)\right]}{\sum_\sigma \rho_\sigma / \tau_\sigma^I} = \frac{1}{2\tau_\sigma^I + 1} u_\sigma^{eq} \quad (6.5)$$

Substituting Eq.6.5 into Eq.6.3, Eq.6.3 can be rewritten as

$$u_\sigma^{eq} = \sum_\sigma \frac{1}{2\tau_\sigma^I + 1} u_\sigma^{eq} + \frac{\sum_\sigma \sum_i B_i^\sigma e_i / \left[\tau_\sigma^I(2\tau_\sigma^I + 1)\right]}{\sum_\sigma \rho_\sigma / \tau_\sigma^I} + \frac{\tau_\sigma^I F_\sigma}{\rho_\sigma} \quad (6.6)$$

Rearrangement of Eq.6.6, u_σ^{eq} can be explicitly solved by

$$\left(1 - \sum_\sigma \frac{1}{2\tau_\sigma^I + 1}\right) u_\sigma^{eq} = \frac{1}{2\tau_\sigma^I + 1} u_\sigma^{eq} + \frac{\sum_\sigma \sum_i B_i^\sigma e_i / \left[\tau_\sigma^I(2\tau_\sigma^I + 1)\right]}{\sum_\sigma \rho_\sigma / \tau_\sigma^I} + \frac{\tau_\sigma^I F_\sigma}{\rho_\sigma} \quad (6.7)$$

In the case of the single component multiple phases LBM simulation, since relaxation time is unique, the equilibrium velocity is obtained by,

$$u^{eq} = \frac{1}{2\tau^I \rho} \sum_i B_i e_i + \left(\tau^I + \frac{1}{2}\right) \frac{F}{\rho} \quad (6.8)$$

6.2. The improved LBM scheme

Table 6.1: The equilibrium velocity formula of explicit and improved scheme

Scheme	Equilibrium velocity formula
Explicit Scheme	$u^{eq} = \dfrac{\sum_i \left[\left(1 - \frac{1}{\tau^E}\right) f_i + \frac{1}{\tau^E} f_i^{eq} \right] e_i}{\rho} + \tau^E \dfrac{F}{\rho}$
Improved Scheme	$u^{eq} = \dfrac{\sum_i \left[\left(1 - \frac{1}{2\tau^I}\right) f_i + \frac{1}{2\tau^I} f_i^{eq} \right] e_i}{\rho} + \left(\tau^I + \frac{1}{2}\right) \dfrac{F}{\rho}$

Substitute B_i into Eq.6.8, the equilibrium velocity is obtained by

$$u^{eq} = \frac{\sum_i \left[\left(1 - \frac{1}{2\tau^I}\right) f_i + \frac{1}{2\tau^I} f_i^{eq} \right] e_i}{\rho} + \left(\tau^I + \frac{1}{2}\right) \frac{F}{\rho} \tag{6.9}$$

In comparison with the equilibrium velocity formula of the explicit scheme, as shown in Table 6.1, it is found that if $\tau^I = \frac{1}{2}$, the improved scheme is the same with the explicit scheme. If $\tau^I \neq \frac{1}{2}$, the difference between explicit and improved scheme is in the terms of the weights of f_i and f_i^{eq}. The effect of relaxation time on the numerical stability of multiphase LBM simulations is further discussed in Section 6.3.1.

In the case of two component LBM simulation, the equilibrium velocity for each component is obtained by

$$u_1^{eq} = \frac{\beta \rho_2 (\tau_1^I F_1 / \rho_1 - \tau_2^I F_2 / \rho_2) - \chi - \tau_1^I F_1 / \rho_1}{\alpha \rho_1 + \beta \rho_2 - 1} \tag{6.10}$$

$$u_2^{eq} = \frac{\alpha \rho_1 (\tau_2^I F_2 / \rho_2 - \tau_1^I F_1 / \rho_1) - \chi - \tau_2^I F_2 / \rho_2}{\alpha \rho_1 + \beta \rho_2 - 1} \tag{6.11}$$

where subscripts 1 and 2 denote component 1 and 2, respectively. And

$$\alpha = \frac{\frac{1}{\tau_1^I} \frac{1}{2\tau_1^I + 1}}{\frac{1}{\tau_1^I} \rho_1 + \frac{1}{\tau_2^I} \rho_2} \tag{6.12}$$

$$\beta = \frac{\frac{1}{\tau_2^I} \frac{1}{2\tau_2^I + 1}}{\frac{1}{\tau_1^I} \rho_1 + \frac{1}{\tau_2^I} \rho_2} \tag{6.13}$$

$$\chi = \frac{\frac{1}{\tau_1^I(2\tau_1^I + 1)} \sum_i B_i^1 e_i + \frac{1}{\tau_2^I(2\tau_2^I + 1)} \sum_i B_i^2 e_i}{\frac{1}{\tau_1^I} \rho_1 + \frac{1}{\tau_2^I} \rho_2} \tag{6.14}$$

It is noticed that from the re-derivation, the implicit scheme is successfully expressed by the improved explicit scheme. The equilibrium velocity is explicitly obtained without iterations. And then the equilibrium distribution function on time step $t + \Delta t$ can be solved by Eq.3.14. Finally, based on the Eq.6.1, the distribution functions of the particles in the whole simulation domain on time step $t + \Delta t$ are solved. The flowchart of the algorithm of the improved scheme is shown in Fig.6.1.

6.3 Simulations and Discussion

6.3.1 Single Component Multiple phase

In order to verify the improved scheme in the simulation of single component multiphase flow, the simulation using the improved scheme using SC EOS [147] and PR EOS is compared with that of the explicit scheme in terms of the density ratio and spurious velocity.

A series of simulations of two-dimensional stationary bubble were carried out in the domain of 50×50 lattice and with the periodic boundary conditions. Initially, the droplet is located at the center of the domain. The densities for two phases are 0.2 and 2.0, respectively. The value of interaction strength was set to be -0.6. The external force is ignored in this study.

Based on the discussion in Section 6.2, it is noticed that the improved scheme is different with the explicit scheme as $\tau^I \neq \frac{1}{2}$. Therefore, in this study, the simulations were carried out with two viscosities, they are $1/12$ and $1/4$, respectively, corresponding to the relaxation times 0.75 and 1.25 in explicit scheme, and 0.25 and 0.75 in the improved scheme.

The comparison result between the improved scheme and explicit scheme using SC EOS is shown in Figure 6.2. As $\tau^I < \frac{1}{2}$, corresponding to the viscosity is $1/12$, the maximum density ratio are 17.59 and 26.99 for the explicit and the improved scheme, respectively. It indicates that the improved scheme successfully increases the density ratio approximately

Start. T=0

Initialization
$\rho \ ; \ u$

Calculate the distribution function by Eq (5.2)

$$f = f_i^{eq} = \omega_i \rho \left[1 + 3\frac{u^{eq} e_i}{c^2} + \frac{9}{2}\frac{\left(u^{eq} e_i\right)^2}{c^4} - \frac{3}{2}\frac{u^{eq} u^{eq}}{c^2} \right]$$

Calculate the equilibrium velocity by Eq (5.14)

$$u^{eq} = \frac{\sum_i \left[\left(1 - \frac{1}{2\tau}\right)f_i + \frac{1}{2\tau}f_i^{eq} \right] e_i}{\rho} + \left(\tau + \frac{1}{2}\right)\frac{F}{\rho}$$

Calculate the equilibrium distribution function by Eq (5.2)

$$f_i^{eq} = \omega_i \rho \left[1 + 3\frac{u^{eq} e_i}{c^2} + \frac{9}{2}\frac{\left(u^{eq} e_i\right)^2}{c^4} - \frac{3}{2}\frac{u^{eq} u^{eq}}{c^2} \right]$$

Calculate the distribution function by Eq (5.10)

$$f_i = \frac{1}{2\tau + 1}\left(B_i + f_i^{eq}\right)$$

Stream

Calculate the macroscopic varies by Eq (5.3) and (5.4)

$$\rho = \sum_i f_i \ ; \quad u = \frac{1}{\rho}\sum_i f_i e_i$$

Calculate the forces and equilibrium velocity by Eq (5.5)

$$u^{eq} = u' + \frac{\tau F}{\rho}$$

Calculate error

$$Err = \frac{\sum_j \sum_i \|u_{T+1} - u_T\|}{\sum_j \sum_i \|u_{T+1}\|}$$

Err<Eps && T<T$_{max}$

Y

T=T+1

N

End

Figure 6.1: The flowchart for the algorithm of the improved scheme.

6.3. Simulations and Discussion
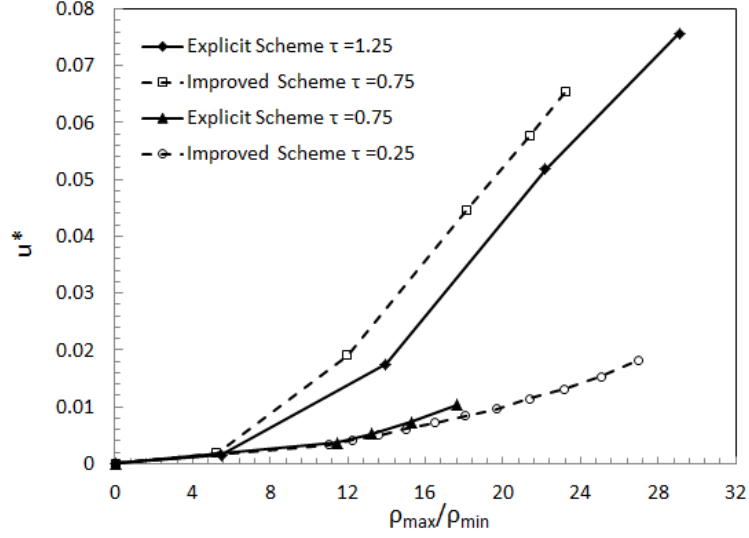
Figure 6.2: The spurious velocities of the explicit and new scheme varies with the density ratio, adopting the SC EOS and viscosity are $1/12$, $1/4$, respectively.

53.4%. On the other hand, achieving the same density ratio, the spurious velocity yields from the improved scheme is less than that from the explicit scheme. As the density ratio is 17.59, the spurious velocity of the improved scheme is 21.7% less than that of the explicit scheme.

In contrast, as $\tau^I > \frac{1}{2}$, corresponding to the viscosity is $1/4$, the spurious velocity of the improved scheme is greater than that of the explicit scheme and the maximum density ratio is 20% less that of explicit scheme. It is concluded that the improved scheme can increase the numerical stability of LBM as $\tau^I < \frac{1}{2}$. However, as $\tau^I > \frac{1}{2}$, the improved scheme produces the greater spurious velocity than that in the explicit scheme.

The PR EOS [185] is applied in both of the improved scheme and explicit scheme to investigate the numerical stability in large density ratio simulation. It is found that the simulations of the explicit scheme using PR EOS at $\tau^E = 0.75$ is unstable and crush after 100 time steps, as shown in Figure 6.3. However, at $\tau^I = 0.25$, the improved scheme using PR EOS can reach the steady state with a series of interaction strength G_{12}. The maximum density ratio is approximately 91.2, as shown in Figure 6.4. It confirms that the improved scheme is much stable than the explicit scheme in the multiphase LBM simulation of large density ratio as $\tau^I < \frac{1}{2}$. In addition, in comparison with the simulation of the improved scheme with SC EOS, the maximum density ratio of the improved scheme using PR EOS
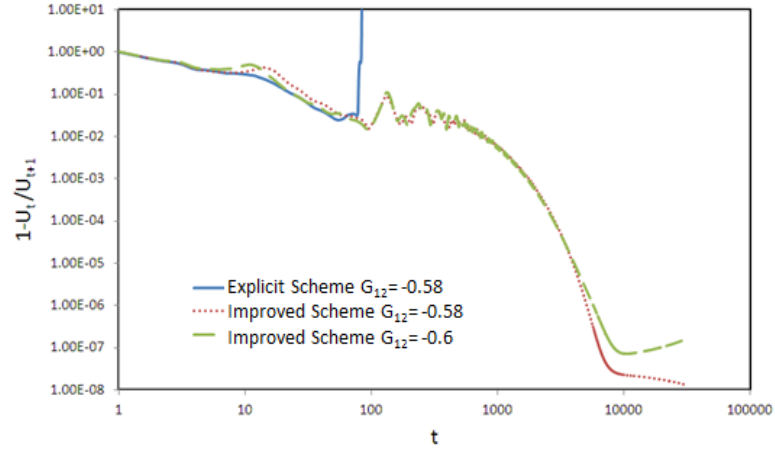
Figure 6.3: The spurious velocity varies with the simulation time step. The vertical and horizontal coordinates are in logarithmic scale.

is approximately 2.4 times greater than that using SC EOS, as seen in Figure 6.4. Therefor, the PR EOS increases the numerical stability in comparison with SC EOS.

The comparison study of the improved scheme and explicit scheme at $\tau^I = 0.5$ is shown in Figure 6.2. It is found that the simulations results of the improved scheme and explicit scheme are negligible. These results is consistent with the scheme discussion that at $\tau^I = \frac{1}{2}$, the improved scheme is the same with the explicit scheme. In addition, it is noticed that at $\tau^I = 0.5$, the maximum density ratio increases to 7000. Therefore, the improved scheme increases the simulation stability as τ^I approaches to 0.5.

6.3.2 Multiple component

In this section, the two-dimensional multiple component simulations of a stationary droplet using the explicit and improved scheme are investigated, in terms of spurious velocity, interaction force and stability. The simulations were carried out in the 100×100 simulation domain. The initial densities of the droplet and the surrounding liquid are 0.6 and 1.0, respectively. The initial radius of the central droplet was set to be 10 lattices. The relaxation times for the explicit and improved method are 1.0 and 0.5, respectively. The periodic boundary conditions were applied on the four boundaries. To be simple, the body force is ignored in this study. The interaction strength for the explicit method was fixed to be $G_{12}=G_{21}=0.1$. The interaction strength of the improved scheme changes from 0.1 to 0.2. The steady-state of the simulation is attained by calculating the entire particles'
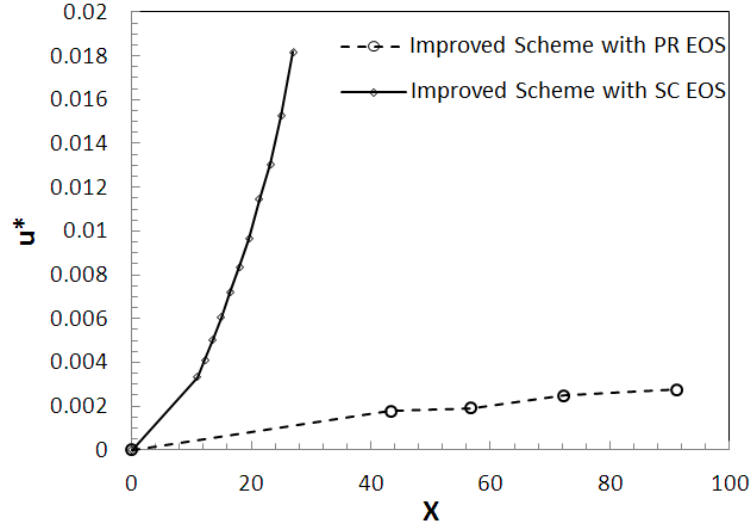
Figure 6.4: The spurious velocity varies with the density ratio in the simulations of the improved scheme using PR and SC EOS at τ^I=0.25.

velocity in the simulation domain and is governed by

$$\frac{\sum_i \left\| u(x_i, t+1) - u(x_i, t) \right\|}{\sum_i \left\| u(x_i, t+1) \right\|} \leq 10^{-10} \tag{6.15}$$

With a series of interaction strength G_{12}, the droplet density distribution of the improved scheme near the interface at the steady-state is compared with that of the explicit, as seen in Figure 6.6. It demonstrates that the values of the interaction strength for the explicit and improved scheme are different to obtain the same density distribution on the steady-state. In order to maintain the sharp interface and same density distribution, the simulation result of the improved method with G_{12}=0.14 is used to compare with that of explicit method with G_{12}=0.1. Both of these two cases keep the same order of numerical diffusion magnitude, 3×10^{-3}.

The spurious velocity distributions along y=50 of the explicit and improved scheme are shown Figure 6.7. The maximum spurious velocity along y=50 for the explicit scheme of G_{12}=0.1 and the improved scheme of G_{12}=0.14 are 8.643×10^{-3} and 1.675×10^{-3}, respectively. It indicates that the spurious velocity effectively reduces as expected though the higher-order expansion of the collision operate. The improved scheme successfully reduces the spurious velocity approximate 80%, as the same density ratio is achieved.
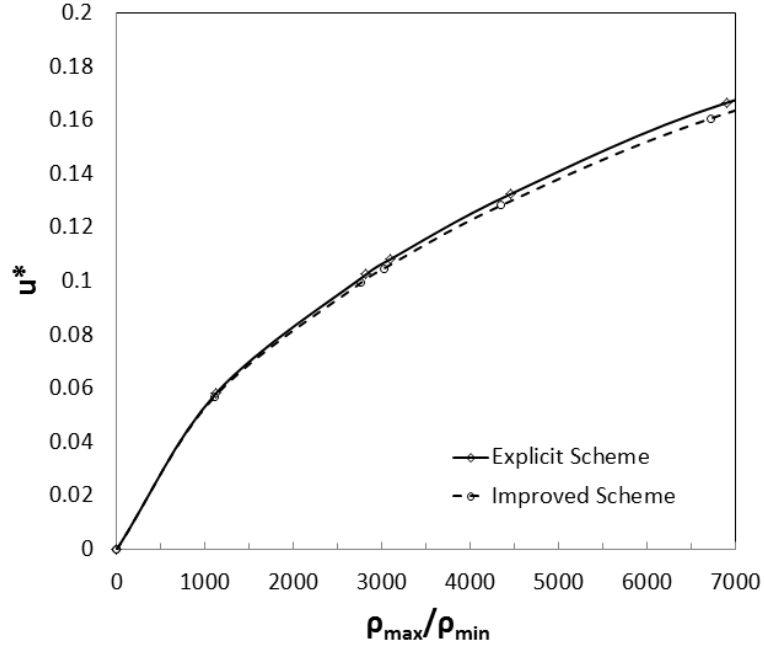
Figure 6.5: The spurious velocity varies with the density ratio in the simulations of the improved scheme and explicit scheme using PR EOS at τ^I=0.5 (τ^E=1.0)

The velocity vector and magnitude of the spurious velocity of the explicit and improved scheme in the whole simulation domain are shown in Figure 6.8 and Figure 6.9, respectively. It is seen that the spurious velocity yielded from the improved scheme is significantly smaller than that from the explicit method, not only the magnitude, but also the spreading region. The maximum spurious velocity of the explicit scheme is 3.579×10^{-2}, in contrast, is 9.298×10^{-3} in the improved scheme. The spurious velocity of the improved method reduces approximate 4 times than that of the explicit scheme. Therefore, this improved method can significantly reduce the spurious velocity near the curved interface in multicomponent simulation.

6.4   Conclusion

In this study, an improved scheme is derived from the non-linear implicit trapezoidal lattice Boltzmann scheme to simulate the large density ratio two-fluids flow. It is found that the non-linear implicit trapezoidal lattice Boltzmann scheme is a linear scheme in nature. From the re-derivation, the implicit scheme is successfully expressed by the improved scheme. The equilibrium velocity is explicitly obtained without iterations. The improved
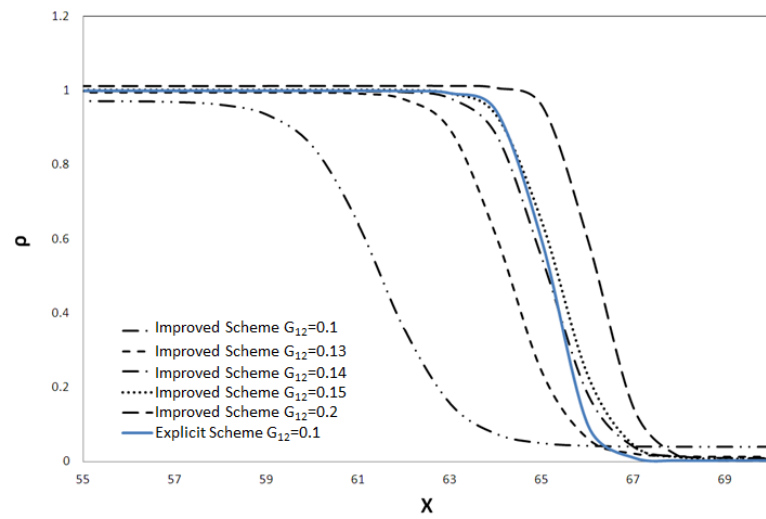
Figure 6.6: The droplet density distribution at the steady-state time step under different interaction strength G_{12}.
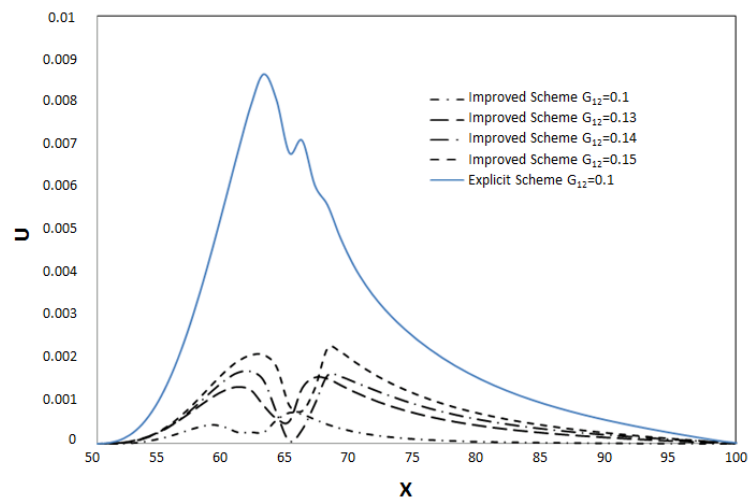
Figure 6.7: The velocity distribution on interface between two component at the steady-state time step (y=50).
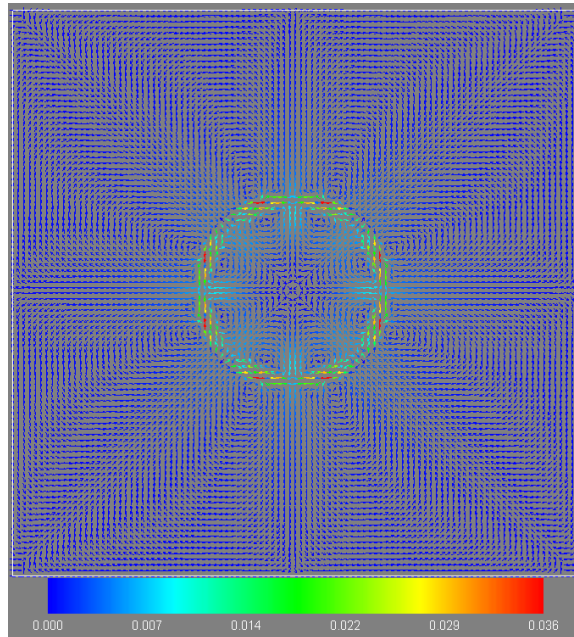
Figure 6.8: Velocity profile in the whole simulation domain for explicit scheme at G_{12}=0.1.
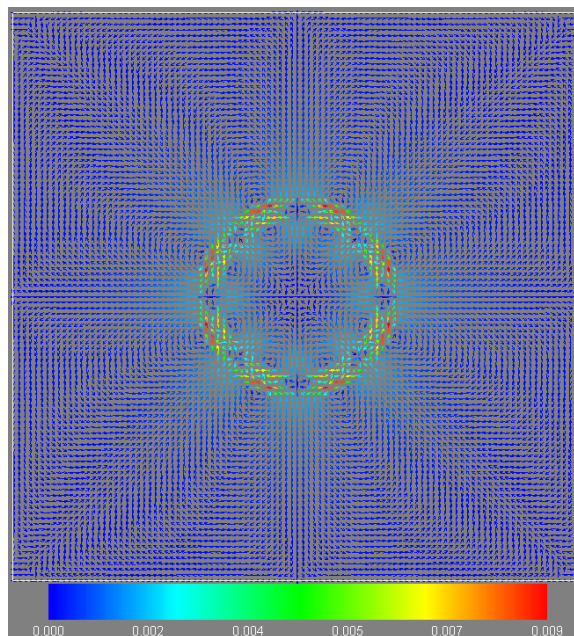
Figure 6.9: Velocity profile in the whole simulation domain of improved scheme at G_{12}=0.14.

scheme successfully reduces the computational time. In addition, the improved scheme retains the second order accurate to reduce the spurious velocity and increase density ratio.

In the simulation of multiphase fluid flow, it is found that the benefit of the improved scheme is related to the relaxation time. As the relation time of the improved scheme τ^I=1/2, the improved scheme is as the same as the explicit scheme. As τ^I<1/2, the improved scheme using SC EOS successfully increases the density ratio approximately 53.4% and reduces the spurious velocity approximately 21.7%, in comparison with that of the explicit scheme using SC EOS. As τ^I>1/2, the explicit scheme, the spurious velocity of the improved scheme is greater than that of the explicit scheme and the maximum density ratio is 20% less that of explicit scheme. It is concluded that the improved scheme can increase the numerical stability of multiphase LBM as $\tau^I < \frac{1}{2}$.

In the simulation of multicomponent fluid flow, with the same density distribution at steady state, the improved scheme reduces both the magnitude and spreading region of the spurious velocity. The spurious velocity of the improved method reduces approximate 4 times than that of the explicit scheme.

Chapter 7

Conclusions and future work

7.1 Conclusion

Global warming is regarded as a serious environmental problem which human beings have to face today. Anthropogenic greenhouse gases are responsible for the most of the observed temperature increase [25]. Carbon dioxide as one of the greenhouse gases appears to be responsible for acceleration of global warming, since the concentration of carbon dioxide in the atmosphere correlates with the variations in Earth surface temperature since 400000 years before 2007 [4].

In order to restrict the concentration of carbon dioxide in the atmosphere, Carbon dioxide Capture and Storage (CCS), as a CO_2 mitigation option, has been proposed and undertaken worldwide. In comparison with other mitigation options, CCS could reduce the mitigation cost and is flexible in reducing CO_2 emission. However, the main risk is leakage, which is also the major concern regarding application of CCS in engineering scales. CO_2 can be stored in a geoformation by relying on various trapping mechanisms. Understanding of the physical and chemical mechanisms of interaction of CO_2, brine and the geoformation is clearly important to assess the risk. The dynamics of interaction in CO_2 geological storage can be described by the theory of multicomponent fluid flow with mass and energy transfer in geoformation. The mechanism study of geological storage at pore scale is critical to understand fundamental knowledge regarding CCS and to enable improvement of the large scale model.

LBM is regarded as an effective model with which to simulate multiphase/multicomponent fluid flow in complex geometries. It is one of types of the numerical models which are suitable not only for use in the mechanism studies to provide data to enable up-scaling of

the model for large scale simulation, but potentially for direct application to Lab scale or even field scale simulations by parallel-LBM using supercomputers.

In this study, LBM was used to develop the multicomponent mass transfer model at pore scale. The contributions from this study to the development of the LBM are summarized as follows.

1) A novel multicomponent LBM dissolution model for simulating mass transfer at pore scale is proposed for the mechanism study of CO_2 dissolution and dispersion in geo-formation. The developed LBM model consists of an interfacial momentum interaction model, a mass transfer model and a convection model.

The interfacial momentum interaction model is based on Shan-Chen's pseudopotential model, which incorporated with the EOS of real fluid. In this model, the interaction strengths of two fluids are optimized to maintain the minimum numerical diffusion near the interface of two fluids. Therefore, physical diffusion was successfully separated from the interfacial tension.

A key characteristic of the proposed model is the introduction of a new diffusion force determined by the given solubility in the mass transfer model. The diffusion is driven by the gradient of chemical potential and is described by the interparticle interaction pseudopotential formation. This diffusion force was calibrated by the analytical solution of a one-dimensional semi-infinite diffusion. The relationship between the physical diffusion coefficient and the diffusion potential strength of the solute particles being transported into the solvent in LBM MCMCP dissolution model was obtained.

The interface between CO_2 and water was determined by the solubility and movable as the CO_2 was dissolving. As the CO_2 was dissolved in water, the solution became a mixture of dissolved CO_2 and water, driven by the negative buoyancy force applied to the water. Therefore, no additional lattice was needed to describe the solute concentration, resulting in a significant saving in computational time. The further dispersion of dissolved solutes is the sum effect of the diffusion and convection.

2) The proposed model was calibrated by a lab experiment involving CO_2 droplet dissolution in water at the state of CO_2 geological storage condition at a depth of 1000m

7.1. Conclusion

depth. Improved PR EOSs of CO_2 and water were introduced and applied in the CO_2 dissolution model. There is a reasonable agreement between the simulation results and the lab experiment, in terms of the shrinking rate of the dissolving CO_2 droplet and concentration distribution of the dissolved CO_2. The effects of Eo number and numerical diffusion on the performance of the dissolution of static droplet were investigated. It was found that the droplet deformation and shrinking rate were related to the Eo number. The shrinking rate increased linearly with the Eo number. As in the case of $Eo \leq 2$, the dissolution droplet remained spherical; while at a larger Eo number, $Eo = 2.4774$, the droplet shape changed to an ellipse. In addition, in order to distinguish the physical diffusion from the numerical diffusion, it is crucial to select a value of the interaction potential strength which approaches the "zero" numerical diffusion. In this study, the interaction potential strength sets to be 7.4.

3) The developed LBM MCMP dissolution model was applied to the investigation of mechanism of CO_2 dissolution and dispersion in geoformation.

3-1) The effects of pore structure on CO_2 dispersion and dissolution were investigated. The geoformation consists of a pores media constructed of channels with different sizes and angles. The effect of channel width and channel tilt angle on the behaviors of CO_2 dissolution and dispersion in water were investigated at the CO_2 geological storage condition (1000 m depth). It was found that the channel with the larger diameter ratio, M, or smaller tilt angle, θ, could reduce the rising up velocity of CO_2 in the geoformation, and consequently restricted the vertical penetration of the stored CO_2. As the channel width increased to provide enough space for the deformation of the droplet, M<1, the shrinking rate was almost independent of the channel width. The channel at $\theta = 90°$ had the largest shrinking rate. In addition, it was found that the wobbling and breakup of the solution tail were prone to occur in the channel with smaller M and a larger tilt angle. In this study, the wobbling of the droplet was observed at the region with the Re number of 300-600 and the Eo number of 20-43.

3.2) The interactions of CO_2 droplets in a pore-scale channel were also examined. The interactions of the penetration into water of a pair of CO_2 droplets in the channels (M=1 and M=0.3) were investigated by the developed model. It was found that the performance

of dissolution of a pair of droplets with an initial distance of 4.5 times the droplet diameter is differed from that of single droplet. Regardless of the channel size, the shrinking rate of the upper droplet was larger than that of the following droplet after the following droplet entered the solution field of the upper droplet. The rising velocity of the following droplet was larger than that of the upper droplet, and also than that of a single droplet under the same conditions. Therefore, multiple CO_2 droplets penetrated the water more easily than the single droplet. It was interested to find that due to the action of the tail vortex of the upper droplet on the following droplet at a different wobbling frequency, the rise of the following droplet accelerated and it then merged into the upper droplet.

4) An examination of the LBM numerical scheme was conducted. In addition to the application of the LBM in CO_2 geological storage, the scheme of the LBM was studied with regard to the high density ratio and spurious velocity. After analysis of the non-linear implicit trapezoidal LBM scheme, an improved scheme was derived by a linear format. An attractive feature of this scheme is the saving in computational time, which benefit in the case of large domain simulations. In the simulation of single component multiple phase, it was found that when the relaxation time of the improved scheme was equal to 1/2, the improved scheme was as the same as the explicit scheme. When the relaxation time of the improved scheme was less than 1/2, the improved scheme successfully reduced spurious velocity by approximately 21.7% and increased the density ratio by approximately 53.4% in the multiphase LBM simulations. In the multiple component simulations, the spurious velocity of the improved scheme was reduced approximate 80% in comparison with the explicit scheme.

7.2   Proposal for the future work

The LB MCMP model is a recently merged numerical technique used to simulate multi-phase fluid flow, in particular molecule interactions, phase separation, phase changes and mass and heat transfer, in addition to traditional computational fluid dynamics (CFD). The LB MCMP model is a model of solving a set of discrete transport equations of fluid particle probability distribution in a phase space, which comprised time, special coordi-

nators and momentum. The features of LBM were reviewed and discussed in Chapter 3. With regard to the further development of the LB MCMP model, some proposals follow.

1). One of the challenges regarding pseudopotential based models is to enhance the numerical stability, which results from the forces introduced on the interface between fluid-fluid and fluids-solid.

For fluid interfacial forces, models are required to precisely describe the characteristics of the interfacial interactions for the exchange of mass, momentum, and energy while generating minimum numerical diffusions, particularly in the case of interfaces with a large density difference. As such, physical diffusions then could be distinguished from unphysical diffusions generated by numerical schemes.

It should be recognized that numerical diffusion and numerical stability are the counterpart of a numerical problem pair. An optimized scheme, particularly for the LB MCMP model, should be further investigated in order to cope with the unequal relaxation time for each fluid.

2). In the case of the CO_2/water system, the modelling of hydrate formation and dissociation is an interesting challenge and also a good opportunity for further application of the LB MCMP model to CO_2 geological and ocean storage investigation. The CO_2 hydrate model can be developed by implementation of the dissolution model developed in this study for modelling the hydrate formation of the CO_2 solution.

3). Development of a mechanism model to upscale the dissolution model from pore scale to the large-scale is another challenge in the future. Since it has a the fine grid in the small-scale, in the large-scale it would be a coarse grid. It is crucial to merge the mechanisms found in the small-scale into the large-scale. In LBM programming, the parallel computing LBM code should be developed by using a cluster-system or supercomputers for a potential engineering application to the transient and three dimensional flows, in order to reduce the computational cost.

In addition to the application of the developed LBM dissolution model in CO_2 geological storage, the proposed model can be applied in the fluid mass transfer problems, such as liquid drug delivery in blood, waste water treatment, and transport of liquid contaminants

in groundwater.

Appendix A

Numerical simulation of CO_2 solution penetration in the marine sediments

A.1 Introduction

From literature reviews, the researchers investigated ocean acidification due to the increased CO_2 concentration in the macroscale [231] [232] [119] [42]. However, the mechanism of the CO_2 solution penetration in microscale has been not paid enough attention. Therefore, the interaction between CO_2 solution and seawater in the marine sediment is concerned about in this study.

Once CO_2 seepage dissolves in the seawater, due to the CO_2 solution is denser than the seawater, the CO_2 solution flows down to the seafloor due to the gravity and continues penetrating into the marine sediment. As CO_2 penetrates in the marine sediment, the PH of the seawater decreases, which threaten the marine organisms and benthic macrofauna habitat in the marine sediment [233] [234] [235] [236]. A prediction of the denser CO_2 solution penetration is valuable to evaluate the CO_2 geological storage site and investigate the impact of CO_2 solution on the marine ecosystem.

One of the key methods for predicting the CO_2 solution penetration in the marine sediment is the numerical simulation. In this study, the numerical simulations are carried out to investigate the mechanism of the CO_2 solution penetration in the marine sediment in microscale, including analyzing the effect of ocean seafloor current, the effect of the pore size, the effect of the grains and the effect of burrow on the marine sediment structure and PH varies.

This chapter is organized as follows. In Section A.2, the model is validated by lab exper-

iment data. The setup of the numerical simulation model to investigate the mechanism of CO_2 solution penetration is described in Section A.3. The simulation results and discussion are presented in A.4, including the effect of ocean seafloor current, the pore size, the grains and the burrow on the CO_2 solution penetration in the marine sediment. Finally, the conclusion is summarized in Section A.5.

A.2 Model Validation

The CO_2 dissolution penetration in the marine sediment can be simplified as the simulation of fluid flow in porous media. To validate the D2Q9 LB model, the simulation results of fluid flow over man-made porous media are compared with the experimental data proposed by C. Manes et al. [237]. The experiment was designed to clarify the surface and subsurface flow within the permeable bed(porous media). In the experiment, glass balls with the same diameter(12mm) packed in a cubic matrix were used to simulate the porous media. Five layer sphere particles imitated a rough and permeable bed were arranged in a open channel. The velocity in each pore was measured by ultrasonic velocity profiler (UVP) [237].

The simulation parameters corresponding to the experimental condition is shown in Table A.1. The unit conversion from experimental condition to LB unit is according to the instruction by Jonas [211]. The simulation is in two-dimensional on the basis of the proportion of width to depth is higher than 5. The simulation domain is of 1036 lattices in x-direction and 296 lattices in y-direction (1036×296), including 20 rows' particles in y-direction and 5 layers in x-direction, as shown in Figure A.1. Initially, the fluid flows into the channel from the left hand side with the equivalent velocity distribution (u_b=0.0254) in x-direction. The space between each particles is 4 lattices, which is in order to reach the porosity 48%. The boundary conditions on top and bottom apply the velocity boundary condition. To save computing time and simulate fluid flow in the channel with 5.5m length, the periodic boundary condition was applied on the left and right boundaries.

The simulation results of velocity distribution in the whole flow domain and subsurface

A.2. Model Validation

Table A.1: Simulation parameters correspond to the experimental condition. H is the depth between the bed surface and free flow surface; R is the radius of glass particles; v is the viscosity of fluid; u_b is the averaged velocity

	Experimental data	LB unit
H	20mm	40
R	12m	24
v	1×10^{-6} m^2/s	0.0002
u_b	0.254m/s	0.0254
ϕ	48%	48%
$Re = u_b H / v$	5588	5588

are shown in Figure A.2. The velocity is averaged in space. The ordinate in Figure A.2 denotes the normalized depth (y/d), d is the diameter of particles. As shown in Figure A.2a, in the surface flow area, the mean velocity decreases with depth and is linear related with the depth, in particular, in the transition region between surface and subsurface flow. Moreover, the velocity decreases slowly in the top boundary area. The results are consistent with the experimental result [237]. In contrast, in the subsurface flow area, the velocity slightly increases with the depth. In order to distinguish the difference, Figure A.2b shows the pore velocity between the five layers. The velocity is selected on the point that is in the middle of two layers in the vertical direction. The velocity results represent that the velocity apparently increases from top pore (y/d=-1) to third one (y/d=-3), while slightly changes from third pore to the bottom one (y/d=-4).

The velocities of the four pores obtained from the simulations are 33.322 mm/s, 42.233 mm/s, 48.021 mm/s and 48.022 mm/s, respectively, which are 30mm/s, 40mm/s, 47mm/s and 47mm/s, respectively in the lab experiment. The simulation result is a little bit higher than the experimental data, it is more likely because of the roughness of the particles, which is not considered in the model. Even so, compared with the measurement result, the simulations get an acceptable agreement with the experiment data in the magnitude and distribution of the velocity.

The validation example demonstrates a satisfactory correspondence between the LBM model and experimental data. This allows more complex process to be researched in the future.
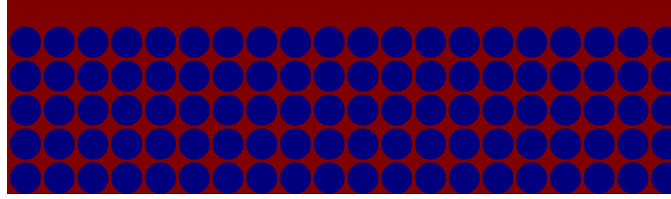
Figure A.1: Schematic of the simulation domain to evaluate the fluid flow in the porous media. Blue color spheres represent the glass particles in the experiment; Red color indicates the fluid space
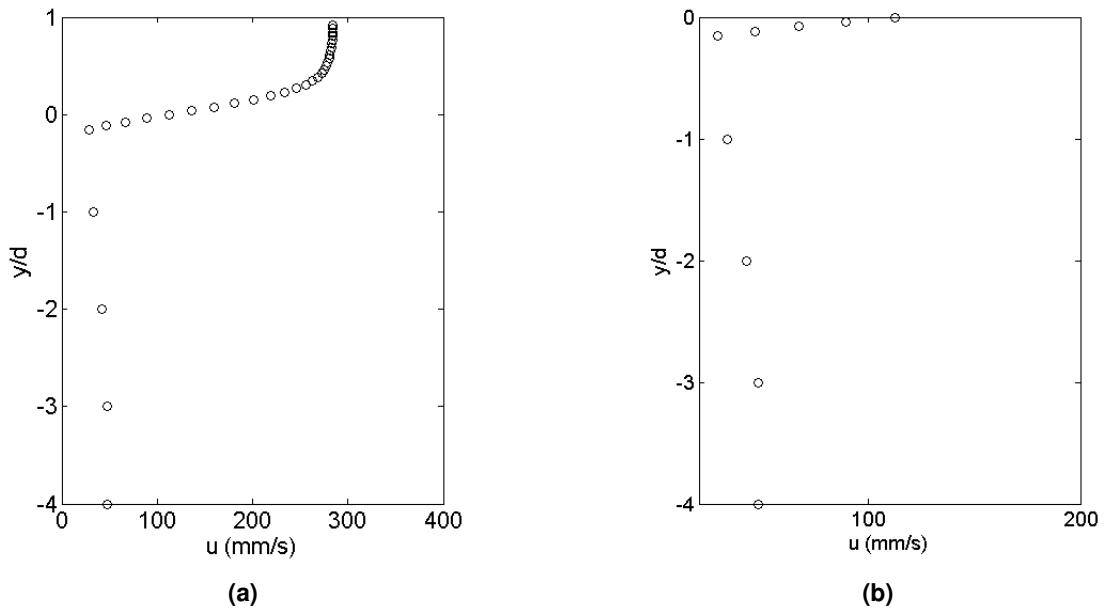
Figure A.2: Velocity profile on x=522lu(lattice unit) for (a)the whole flow domain; (b)four layers' pore velocity

A.3 Numerical Simulation Set Up

To illustrate the impact of CO_2 solution in marine sediments, the LB model is established based on two-component Shan-Chen model described in Sec.3.5. Initially, the CO_2 is located on the top layer above the marine sediment. The seawater (Salinity=3.5%) is filled in the porous media layer on behalf of the marine sediment. Due to the density of CO_2 solution is larger than the seawater, the penetration occurs on the boundary between the CO_2 solution and seawater. The CO_2 solution penetrates into the marine sediment and affects the marine envionment by decreasing the PH. In order to determine the penetration velocity and PH change in the marine sediment, a series of numerical simulation are carried out as follows.

A.3. Numerical Simulation Set Up
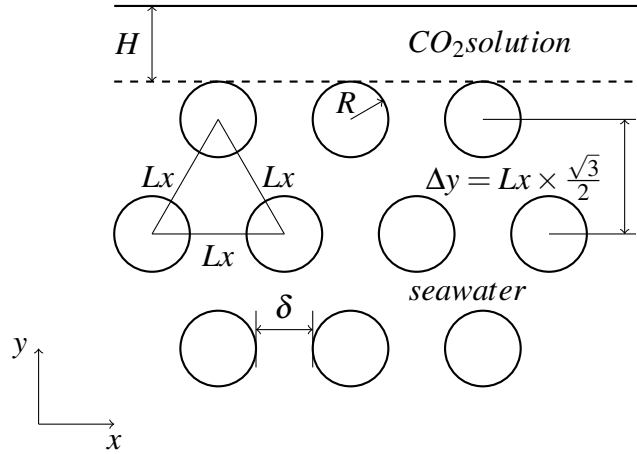
Figure A.3: Schematic of the numerical simulation set up. Dash line is the dividing line between top CO_2 solution layer and porous media layer filled with the seawater; H is the depth of top layer; R is the radius of the particles; δ is the pore between two particles; Lx is the distance between the two center of the particles, $Lx = \delta + 2R$; Ly is the distance between two rows of the particles

Table A.2: Simulation parameters in researching the factors on CO_2 solution penetration. Lx is the length of the horizontal direction; Ly is the vertical depth of the simulation domain; H is the depth between the bed surface and free flow surface; δ is the pores in the marine sediment; R is the radius of the grain; u is the maximum seafloor current in horizontal direction.

	Physical unit	LB unit
Lx	400mm	2400
Ly	90mm	570
H	6.7mm	40
δ	1$\sim$1.67mm	6$\sim$10
R	1.33$\sim$2mm	8$\sim$12
u	0.05$\sim$0.2m/s	0.005$\sim$0.02

The simulation condition in this study is under deep ocean environment about 1000m depth with lower temperature (T=10°C) and high pressure (P=10MPa). The density change of carbon dioxide seawater solution is described by $\rho_{cs}(\rho, T, S, \chi) = \rho_{sw}(P, T, S) + 0.273\chi$ [80]. ρ_{cs} and ρ_{sw} are the density of CO_2 solution and seawater, respectively. χ is the mass fraction of carbon dioxide and is assigned to 0.05 in this study. The density difference between CO_2 solution and seawater is 0.01365 kg/m^3.

The parameters used in the numerical simulations are described in Table.A.2 named as LB space. Velocity boundary conditions are applied to the left and right boundaries for both of the CO_2 solution and seawater. The pressure boundary conditions are adopted to

the top boundary of CO_2 solution and bottom boundary of the seawater. The inlet velocity profile on the left hand side is according to the result discussed in Sec.A.2, which is used to simulate the submarine velocity field in the stable state and reduce the computation time. The initial depth of the top CO_2 solution layer is constant and equal to 40 lattices in this study. A number of sphere particles with bounceback boundary condition are used to construct the porous media layer. These particles are triangular distributed in the porous media layer as shown in Figure A.3.

Four factors are considered in this study, they are ocean seafloor current, the grains, the pores and the burrows. In Section A.4.1, the effect of ocean seafloor current on the CO_2 penentration is investigated by changing seafloor current from 0.005 to 0.02. Secondly, due to the porosity is related with both of the grains and the pores, in order to analyze the effect of the pores on CO_2 solution penetration, the size of the grain is fitted to 10 and the pore (δ) varies from 6 to 10. The simulation results are obtained in Section A.4.2. Thirdly, due to the marine sediments can be classified by the grains, such as clay(1/4096 to 1/256mm), silt(1/256 to 1/16 mm), sand(1/16 to 2 mm) and so on, the effect of the grains on the CO_2 solution penetration process is implemented by varying the radius of the grain(R) from 8 to 12, as shown in Section A.4.3. Finally, the effect of the burrows is discussed in Section A.4.4.

A.4 Results and Discussion

A.4.1 Effect of ocean seafloor current

To investigate the effect of ocean seafloor current on CO_2 solution penetration in the marine sediment, a series of simulations are conducted by changing the inlet maximum velocity from 0.005 to 0.02. For each simulation, the radius of the grains and the pores are constant, both of them are 10. The porosity is the same and equal to 58%.

The PH changes in the porous media under three different seafloor currents on t=40000 are shown in Figure A.4. It demonstrates that after CO_2 solution penetrates in the marine sediment, the maximum PH varies in the domain is 2.23 units, which is occurred on the top of the porous media. The PH changes decline with the the increase of the
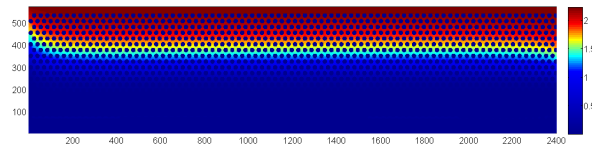
(a)
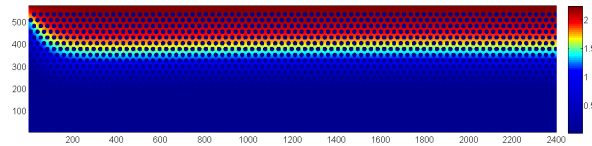
(b)
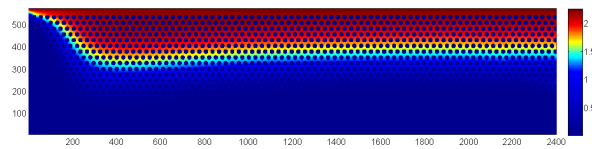
(c)

Figure A.4: PH change in the whole simulation domain on t=40000 for (a)u=0.005; (b)u=0.01, (c)u=0.02.

depth. This is consistent with our prediction. In addition, it was found that the boundary layers between acidified and non-acidified area under three currents are quite different, especially in the area near to the inlet. This is due to the combined effects of the seafloor current and vertical penetration velocity controlled by the buoyancy. Due to the increase of the horizontal seafloor current, the acidified area in the near inlet region is smaller. On the other hand, since seawater in the sediment flows along the horizontal direction, it yields the downward sub-velocity after hitting the sediment particles. The downward sub-velocity increases with the increase of the seafloor current. Therefore, there is a significant drooping on the left hand side in the simulation result of u=0.02.

In Figure A.5 and Figure A.6, the simulation results represent the normalized penetration volume and depth varies with a range of ocean seafloor current. In Figure A.5, the penetration volume (V) is normalized by the total space of the porous media (Vo). It can be seen that the penetration volume increases as the seafloor current increases. Furthermore, the increasing rate of the normalized penetration volume changes with the simulation time. It

A.4. Results and Discussion
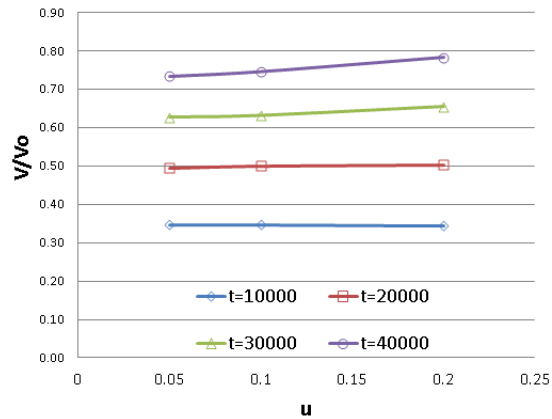
Figure A.5: The varies of normalized penetration volume with the ocean seafloor current. V/Vo is the percentage of the penetration volume in the space of the marine sediment; Vo is the total space of the marine sediment; t is the simulation time step.

can be seen that the normalized penetration volumes with different seafloor currents are nearly the same, for expample, on t=10000, they are 0.347, 0.347 and 0.345, respectively. However, the difference apparently increases on t=40000, the normalized penetration volumes are 0.733, 0.746 and 0.782, respectively. The results of penetration depth are presented in Figure A.6. For the sake of avoiding the boundary impact, the results are from the points in the middle of simulation domain on x=1195. The results show that the penetration depth is dependent on the ocean seafloor current. In Figure A.6, it can be seen that, in the beginning of the simulation time, the penetration depth is slight dependent on the ocean seafloor current. After a period of simulation time step (t>30000), the penetration depth is strong dependent on seafloor current. The average penetration rates are 0.063m/s, 0.064m/s and 0.068m/s for the seafloor current are 0.05m/s, 0.1m/s and 0.2m/s, respectively.

It is summarized that the seafloor current affects the CO_2 solution penetration in marine sediment, not only the map of PH changes, but also the penetration volume and depth. A higher seafloor current accelerates the CO_2 solution penetration rate.

A.4. Results and Discussion
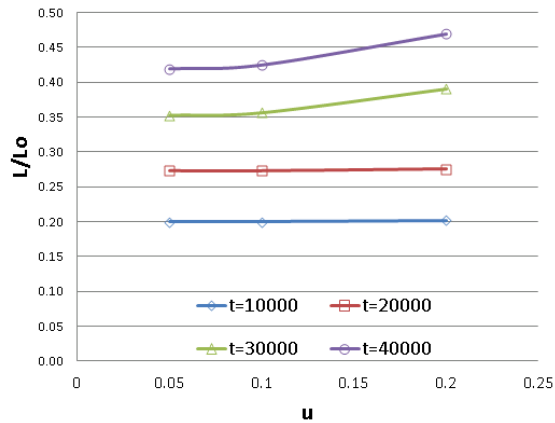
Figure A.6: The varies of normalized penetration depth with the ocean seafloor current. L/Lo is the percentage of the penetration depth in the total depth of the marine sediment; Lo is the depth of the marine sediment; t is the simulation time step.
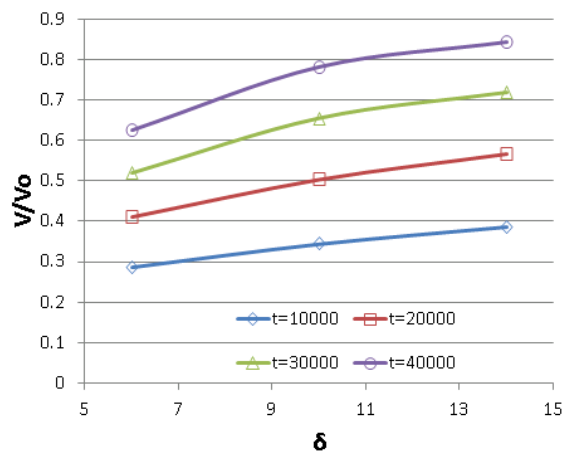
Figure A.7: Normalized penetration volume varies with the sediment pores on each time step. δ is the the sediment pores; Vo is total space of porous media; t is simulation time step.

A.4.2 Effect of sediment pores

Porosity is an important consideration when evaluating the fluid flow in porous media. It depends on both of the pores and the grains. In this section, the impact of the pores is investigated. This study is special for the condition that marine sediment is constructed with the same grains, but with the different pores due to the different burying condition, such as the rate of burial and the depth of burial.

The sediment pores compared in this section are $\delta =6$, $\delta =10$ and $\delta =14$, respectively, which are correspond to the porosity of 0.46, 0.58 and 0.67, respectively. The radius of the

A.4. Results and Discussion
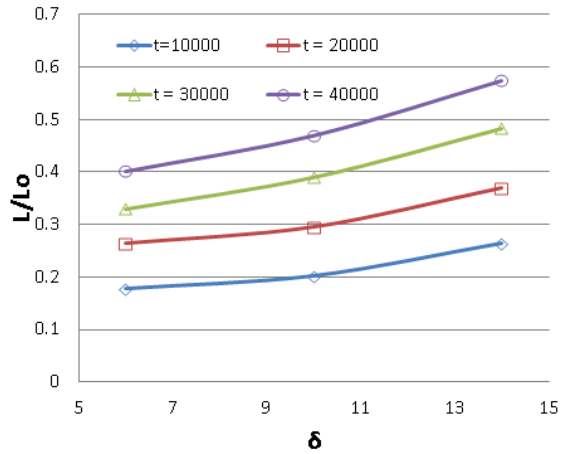
Figure A.8: Normalized penetration depth varies with the sediment pores on each time step. δ is the the sediment pores; Lo is the depth of marine sediment; t is simulation time step.

particles in each simulation is constant to 10 and inlet maximum velocity is set to be 0.02. The simulation results are shown in Figure A.7 and Figure A.8. The results represent that (1) both of the penetration volume and penetration depth of CO_2 solution increase with the increase of the sediment pores; (2) at the same time step, the relationship between penetration volume and the sediment pores is not linear. For example, on time step 20000, the normalized penetration volumes are 41.1%, 50.3% and 56.6% with the pores of 6, 10 and 14, respectively. The increasing rate of penetration volume decreases with the increase of the pores; (3) the increasing rate of penetration depth increases with the increase of the pores; (4) the penetration increasing rate on each time step slightly decreases with the time. These simulation results support that marine sediment with small sediment pore is helpful to reduce the penetration speed. The penetration rate decreases with time.

Figure A.9 presents the PH change results in the whole domain by changing the sediment pores from 6 to 14. The results show that the PH changes in the range of 0 to 2.23 units. It can be seen in Figure A.9 that PH change parallelly reduces in y-direction when far from the inlet, however, the map of PH change near to the inlet is different. It presents that the smaller of the pores the smaller of the area affected by the PH change in the near to inlet region. This is due to the balance between the seafloor current and the penetration rate. Small sediment pores reduce the vertical penetration rate and weaken PH changes in the inlet area. The simulation results presented in this section show that small pores (δ) not
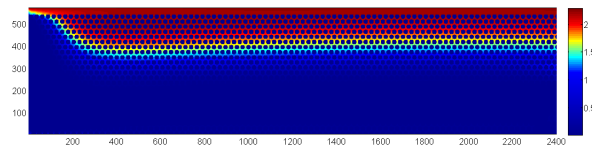
(a)
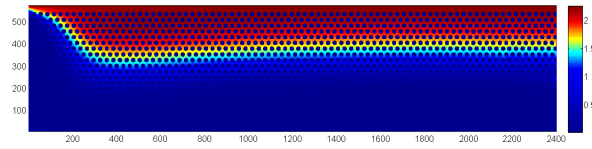
(b)
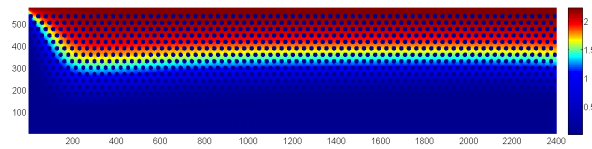
(c)

Figure A.9: PH change in the whole simulation domain on t=40000 for (a)δ =6 (ϕ =0.46), (b)δ =10 (ϕ =0.58),(c)δ =14 (ϕ =0.67)

.

only restrict the penetration rate but also decrease the acidification area in the near to inlet region.

A.4.3 Effect of the grains

Since the marine sediments are composed by the different sizes of grains, the grains is determined in this section by changing the particle radius in the range of 8 to 12. In order to analyze the sediment size, the pores and inlet velocity are constant, which are 10 and 0.02, respectively. The porosities are 0.66, 0.58 and 0.54 respectively.

In Figure A.10a, it can be seen that the normalized penetration volume is almost independent on the particles' radius. That means if the pores and the seafloor current are the same, the effect of the grains on the penetration volume is not obvious. In contrast, as shown in Figure A.10b, the penetration length is dependent on the particle's size and the relation is near to linear. On the time step 40000, the depth of CO_2 solution penetrating into the seawater reaches 53.9%, 47.0% and 34.0% of total depth in the porous medium.

A.4. Results and Discussion

(a)

(b)
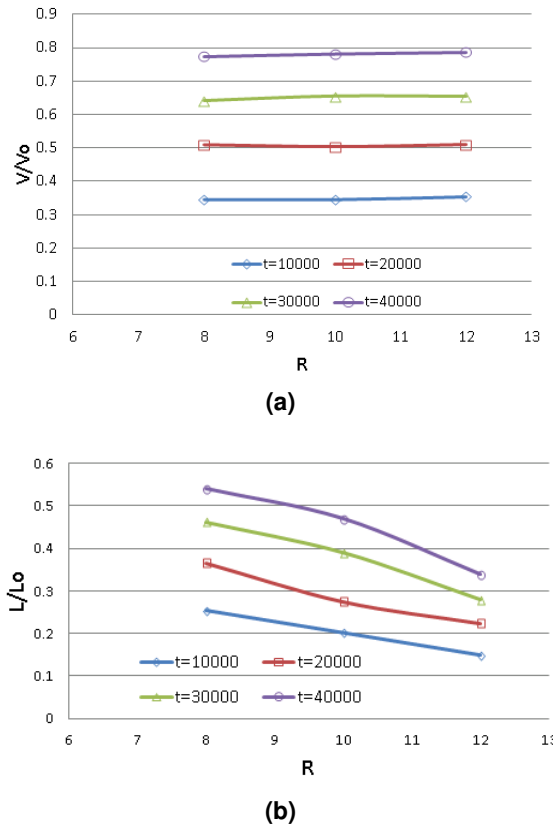
Figure A.10: The effect of the particles' radius on (a) CO_2 solution penetration volume and (b) CO_2 solution penetration depth. Vo is the total space of the porous meida; Lo is the depth of sediment layer

The average vertical penetration velocities are 0.05 m/s, 0.047 m/s and 0.034m/s for the conditions with the radius of 8, 10 and 12, respectively. It concludes that large size of the grains reduces the CO_2 penentration depth, however, penentration volume is rarely affected.

A.4.4 Effect of the burrow

Since marine sediments is not neat distribution and contains diverse structure, such as the burrow structure which inhabited by the benthic macrofauna and bacterial communities [234]. In this section, the effect of the burrow on the CO_2 penetration is investigated. A semi-circular channel is designed to simulate the burrow with the width of 5mm (30 lattices). The simulation condition is described in Section A.3. The simulation domain is 570 lattices (95mm) in y-direction and 960 lattices (160mm) in x-direction. The particle radius, the pores and seafloor current are 10, 10 and 0.02, respectively.
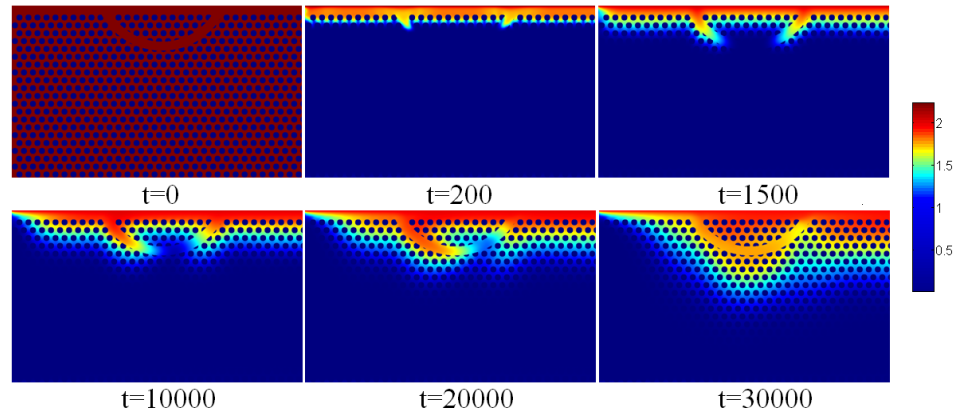
Figure A.11: The simulation results of the PH change in the marine sediment with the burrow at some time step

The PH change results are shown in Figure A.11. The results reveal that (1) the burrow affects the distribution of the PH changes in the marine sediment; (2) the vertical penetration rate in the burrow is larger than the surrounding non-burrow area; (3) in the beginning, the penetration depth in the left and right inlets of the burrow is near the same. After some time steps, for example on t=10000 the difference is apparent. It is due to the effect of the direction of the seafloor current. The penetration rate in the left inlet is larger than the one in the right inlet. As the CO_2 solution reaches the bottom of the burrow, one part of CO_2 solution continues penetrating downward, the other part flows to the right inlet along the channel of burrow, as shown on t=20000. It was found that on t=30000 the minimum PH change in the burrow is located on the right hand side near to the right inlet; (4)The distribution of PH change on t=30000 shows that the area below the burrow is acidified by the CO_2 solution earlier than the non-burrow region in the same depth. The simulation results reveal that the burrow accelerates the ocean acidification in the marine sediment.

A.5 Conclusion

LBM is capable to simulate the fluid flow in the porous media. Based on the simulation results, it was found that the penetration of CO_2 solution into the ocean sediment is dependent on the ocean seafloor current, the pores, the size of the grains and the burrow, respectively. It concludes that a higher seafloor current accelerates the CO_2 solution penetration rate and affects the map of PH changes in the marine sediment. The pores and

A.5. Conclusion
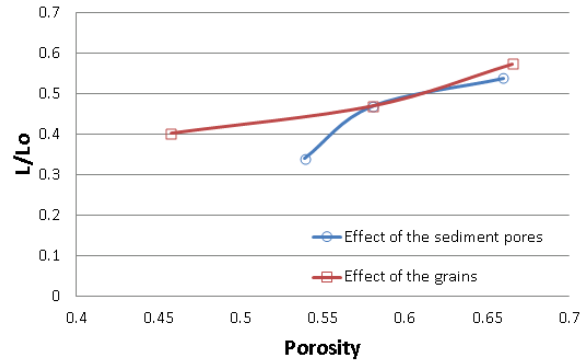
Figure A.12: The normalized penetration depth varies with porosity at t=40000

the size of the grains are another two important factors on the CO_2 solution penetration. It was found that the small pores and large grains restrain the penetration depth and penetration volume. Furthermore, the porosity is not linear with the penetration length. It is supported by the results in Figure A.12. As shown in Figure A.12, the blue curve presents the relationship between the penetration depth and porosity by varying the pores, as described in Section A.4.2. The red line is the results from Section A.4.3 by changing the sizes of the grains. It presents that if the pore and grain size are different, although the porosity is the same, the penetration depth is different. Thus the porosity can not be as a a single variable to evaluate the penetration depth of CO_2 solution. The burrow in the marine sediment changes the CO_2 penetration rate and

In conclusion, the simulation results in this study are useful to understand the mechanism of CO_2 solution penetration in the marine sediment in the microscale. The model can be used to investigate the site of CO_2 geological storage and determine the PH varies in the marine sediment. In this study the marine sediment is simplified as the porous media with the same size sphere particles. But actually, the topology of the structure in the marine sediment can be used into the model in the future, the model will be helpful to investigate the CO_2 geological storage site and the impact of CO_2 solution on the marine ecosystem.

Bibliography

[1] R.R. Nourgaliev, T.N. Dinh, and B.R. Sehgal. On lattice Boltzmann modeling of phase transition in an isothermal non-ideal fluid. *Nuclear Engineering and Design*, 211(2-3):153–171, February 2002.

[2] J. Hansen, M. Sato, R. Ruedy, K. Lo, D.W. Lea, and M. Medina-elizade. Global temperature change. *Proc. Natl. Acad. Sci.*, 103:14288–14293, 2006.

[3] H. Ahlenius. Historical trends in carbon dioxide concentrations and temperature, on a geological and recent time scale. *http://www.grida.no/publications/geo-ice-snow*, 2007.

[4] B. Metz, O. Davidson, H. Coninck, M. Loos, and L. Meyer. *IPCC special report on Carbon Dioxide Capture And Storage*. Intergovernmental Panel on Climate Change, 2005.

[5] H.S. Kheshgi. A nonlinear convolution model for the evasion of CO2 injected into the deep ocean. *Journal of Geophysical Research*, 109(C2):C02007, 2004.

[6] S. Bachu. Screening and ranking of sedimentary basins for sequestration of CO2 in geological media in response to climate change. *Environmental Geology*, 44(3):277–289, June 2003.

[7] R.A. Chadwick, D. Noy, R. Arts, and O. Eiken. Latest time-lapse seismic data from Sleipner yield new insights into CO2 plume development. *Energy Procedia*, 1(1):2103–2110, February 2009.

[8] E. Perkin, I. Czernichowski-Lauriol, M. Azaroual, and P. Durst. Long term predictions of CO2 storage by mineral and solubility trapping in the Weyburn Midale Reservoir. In *Proceedings of the 7th International Conference on Greenhouse Gas Control Technologies (GHGT-7), September 5-9*, pages v.II, 2093–2096, Vancouver, Canada, 2004.

[9] S.C.M. Krevor, R. Pini, B. Li, and S.M. Benson. Capillary heterogeneity trapping of CO2 in a sandstone rock at reservoir conditions. *Geophysical Research Letters*, 38(15):L15401, August 2011.

[10] S.M. Benson, B. Li, M. Krause, S. Krevor, C. Kuo, R. Pini, and L. Zuo. Investigations in Geologic Carbon Sequestration : Multiphase Flow of CO2 and Water in Reservoir Rocks Annual Report 2012. Technical report, 2012.

[11] X. Jiang. A review of physical modelling and numerical simulation of long-term geological storage of CO2. *Applied Energy*, 88(11):3557–3566, November 2011.

[12] F.M. Orr and Jr. CO2 capture and storage: are we ready? *Energy & Environmental Science*, 2(5):449, 2009.

[13] R.S. Middleton, G.N. Keating, P.H. Stauffer, A.B. Jordan, H.S. Viswanathan, Q.J. Kang, J.W. Carey, M.L. Mulkey, E.J. Sullivan, S.P. Chu, R. Esposito, and T.A. Meckel. The cross-scale science of CO2 capture and storage: from pore scale to regional scale. *Energy & Environmental Science*, 5(6):7328–7345, 2012.

[14] B. Dong, Y.Y. Yan, W. Li, and Y. Song. Lattice Boltzmann simulation of viscous fingering phenomenon of immiscible fluids displacement in a channel. *Computers & Fluids*, 39(5):768–779, May 2010.

[15] A. Parmigiani, C. Huber, O. Bachmann, and B. Chopard. Pore-scale mass and reactant transport in multiphase porous media flows. *Journal of Fluid Mechanics*, 686:40–76, September 2011.

[16] M. Ferer and D.H. Smith. Pore-Level Modeling of Carbon Dioxide Sequestration in Brine Fields. In *In: Proceedings of 1st National Conference on*, volume 0, pages 1–13, 2001.

[17] N. Böttcher, J. Taron, O. Kolditz, C. Park, and R. Liedl. Evaluation of thermal equations of state for CO2 in numerical simulations. *Environmental Earth Sciences*, 67(2):481–495, May 2012.

[18] S. Bando and F. Takemura. Rise speed of supercritical carbon dioxide spheres in aqueous surfactant solutions. *Journal of Fluid Mechanics*, 548(-1):133–140, February 2006.

[19] H.W. Stockman, R.J. Glass, C. Cooper, and H. Rajaram. Accuracy and computational efficiency in 3d dispersion via lattice-boltzmann: models for dispersion in rough fractures and double-diffusive fingering. *International Journal of Modern Physics C*, 9(8):1–13, 1998.

[20] C. Chen and D. Zhang. Lattice Boltzmann simulation of the rise and dissolution of

two-dimensional immiscible droplets. *Physics of Fluids*, 21(10):103301, 2009.

[21] S. Someya, S. Bando, Y. Song, B. Chen, and M. Nishio. DeLIF measurement of pH distribution around dissolving CO2 droplet in high pressure vessel. *International Journal of Heat and Mass Transfer*, 48(12):2508–2515, June 2005.

[22] Y. Song, B. Chen, M. Nishio, and M. Akai. Experimental study of dissolution rate of a CO2 droplet and CO2 solubility in high pressure and low temperature seawater with hydrate free. In *Proceedings of OMAE04 23rd International Conference on Offshore Mechanics and Arctic Engineering*, pages 1–7, 2004.

[23] R. Clift, J. R. Grace, and M.E. Weber. *Bubbles, Drops and Particles*. Academic Press, 1978.

[24] J. Lu, G.A. Vecchi, and T. Reichler. Expansion of the Hadley cell under global warming. *Geophysical Research Letters*, 34, 2007.

[25] R.B. Alley, T. Berntsen, and N.L. Bindoff. A report of Working Group I of the Intergovernment Panel on Climate Change, Summary for Policymakers. Technical report, 2007.

[26] J.T. Kiehl and K.E. Trenberth. Earth's Annual Global Mean Energy Budget. *Bulletin of the American Meteorological Society*, 78(2):197–208, February 1997.

[27] R.A. Feely, C.L. Sabine, K. Lee, W. Berelson, J. Kleypas, V.J. Fabry, and F.J. Millero. Impact of anthropogenic CO2 on the CaCO3 system in the oceans. *Science (New York, N.Y.)*, 305(5682):362–6, July 2004.

[28] C.A. Aggelopoulos and C.D. Tsakiroglou. Effects of micro-heterogeneity and hydrodynamic dispersion on the dissolution rate of carbon dioxide in water-saturated porous media. *International Journal of Greenhouse Gas Control*, 10:341–350, September 2012.

[29] T.M.L. Wigley, R. Richels, and J.A. Edmonds. Economic and environmental choices in the stabilization of atmospheric CO2 concentrations. *Nature*, 379(6562):240–243, January 1996.

[30] B. Metz, O. Davidson, R. Swart, and J. Pan. *Climate Change 2001-Mitigation. The Third Assessment Report of the Intergovernment Panel on Climate Change*. Cambridge University Press, Cambridge, UK, 2001.

[31] O. Edenhofer, R.P. Madruga, and Y. Sokona. *Renewable energy sources and*

climate change mitigation: special report of the Intergovernmental Panel on Climate Change, volume 49. Cambridge University Press, Cambridge, UK, July 2012.

[32] *50 years of Nuclear Energy*. International Atomic Energy Agency, 2006.

[33] Key World Energy Statistics 2012. *International Energy Agency*, 2012.

[34] R. Hagan. The future of nuclear power in Asia. *Pacific and Asian Journal of Energy*, 8(1):9–22, 1998.

[35] S. Mori. Effects of carbon emission mitigation options under carbon concentration stabilization scenarios. *Environmental Economics and Policy Studies*, 3:125–142, 2000.

[36] R.T. Watson, I.R. Noble, B. Bolin, N.H. Ravindranath, D.J. Verardo, and D.J. Dokken. *Land Use, Land-Use Change and Forestry*. Cambridge University Press, Cambridge, UK, 2000.

[37] C. Prentice, G. Farquhar, M. Fasham, M. Goulden, M. Heimann, V. Jaramillo, H.S. Kheshgi, C.L. Quere, R. Scholes, and D. Wallace. *The carbon cycle and atmospheric CO2. Climate change 2001: The scientific Basis: Contribution of WGI to the Third Assessment Report of the IPCC*. Cambridge University Press, Cambridge, UK, 2001.

[38] M.I. Hoffert, Y.C. Wey, A.J. Callegari, and W.S. Broecker. Atmospheric response to deep sea injections of fossil fuel carbon dioxide. *Climatic Change*, 2:53–68, 1978.

[39] Global CCS Institute. The global status of CCS. Technical Report January, Global CCS Institute, 2013.

[40] K. Schroeder, E. Ozdemir, and B.I. Morsi. Sequestration of Carbon Dioxide in Coal Seams. In *In proceedings of the First National conference on Carbon Sequestration*, volume 1996, pages 1–10, 2001.

[41] K.A.M. Gasem, R.L. Robinson, and S.R. Reeves. Adsorption of pure methane, nitrogen and carbon dioxide and their mixtures on San Juan Basin coal. *U.S. Department of Energy Topical Report, Contract No.DE-FC26-OONT40924*, page 83, 2002.

[42] C. Doughty. Investigation of CO2 Plume Behavior for a Large-Scale Pilot Test

of Geologic Carbon Storage in a Saline Formation. *Transport in Porous Media*, 82(1):49–76, May 2009.

[43] J. Gale. Barriers to the implementation of CCS. IEA Greenhouse Gas R&D Programme. *Public Power Corporation Seminar on CCS, Athens, Greece.*, 24th June, 2008.

[44] S.M. Benson and D.R. Cole. CO2 Sequestration in Deep Sedimentary Formations. *Elements*, 4(5):325–331, October 2008.

[45] M.A. Hesse, F.M. Orr, and H.A. Tchelepi. Gravity currents with residual trapping. *Journal of Fluid Mechanics*, 611:35–60, August 2008.

[46] S. Taku Ide, K. Jessen, and F.M. Orr. Storage of CO2 in saline aquifers: Effects of gravity, viscous, and capillary forces on amount and timing of trapping. *International Journal of Greenhouse Gas Control*, 1(4):481–491, October 2007.

[47] S.M. Benson. *Lessons Learned from Industrial and Natural Analogs for Health, Safety and Environmental Risk Assessment for Geologic Storage of Carbon Dioxide, Carbon Dioxide Capture for Storage in Deep Geologic Formations - Results from the CO2 Capture Project, v. 2: G.* Elsevier, London, 2005.

[48] W.D. Gunter, E.H. Perkin, and T.J. McCann. Aquifer disposal of CO2 -rich gases: reaction design for added capacity. *Energy Conversion and Management*, 34:941–948, 1993.

[49] IEA Greenhouse Gas R&D Programme. Natural Releases of CO2. Technical report.

[50] T.M. Gerlach, M.P. Doukas, K.A. McGee, and R. Kessler. Soil efflux and total emission rates of magmatic CO2 at the Horseshoe Lake tree kill Mammoth Mountain California 1995-1999. *Chemical Geology*, 177:101–116, 1999.

[51] A.C. Cook, L.J. Hainsworth, M.L. Sorey, W.C. Evans, and J.R. Southon. Radiocarbon studies of plant leaves and tree rings from Mammoth Mountain, CA: a long-term record of magmatic CO2 release. *Chemical Geology*, 177(1-2):117–131, July 2001.

[52] C. Marchetti. On geoengineering and the CO2 problem. *Climatic Change*, 1(March):59–68, 1977.

[53] C.F. Baes Jr., S.E. Beall, D.W. Lee, and G. Marland. *The collection, disposal, and storage of Carbon Dioxide.* 1980.

[54] L.G.H. Van der Meer. Investigation regarding the storage of carbon dioxide in aquifers in the Netherlands. *Energy Conversion and Management*, 33(5-8):611–618, 1992.

[55] O. Kaarstad. Geological storage, including costs and risks, in saline aquifers. *Proceedings of workshop on Carbon Dioxide Capture and Storage, Regina Canada,*, pages 53–60, 2002.

[56] Sam Houoway and British Geological Survey. The potential for aquider disposal of carbon dioxide in the UK. *Energy Conversion and Management*, 34(9-11):925–932, 1993.

[57] R. Korbol and A. Kaddour. Sleipner West CO2 disposal: injection of removed CO2 into the Utsira formation. *Energy Conversion and Management*, 36(6-9):509–512, 1994.

[58] L. Berkeley. Numerical Modeling Studies of The Dissolution-Diffusion-Convection Process During CO2 Storage in Saline Aquifers. 2008.

[59] K. Pruess and J. García. Multiphase flow dynamics during CO 2 disposal into saline aquifers. *Environmental Geology*, 42(2-3):282–295, June 2002.

[60] G.S. Bromhal, W.N. Sams, S. Jikich, T. Ertekin, and D.H. Smith. Simulation of CO2 sequestration in coal beds: The effects of sorption isotherms. *Chemical Geology*, 217(3-4):201–211, 2005.

[61] J.J. Buckles, R.D. Hazlett, S. Chen, K.G. Eggert, D.W. Grunau, and W.E. Soll. Toward Improved Prediction of Reservoir Flow Performance at the pore scale. *Los Alamos Science*, (22), 1994.

[62] S. Bachu. CO2 storage in geological media: Role, means, status and barriers to deployment. *Progress in Energy and Combustion Science*, 34(2):254–273, April 2008.

[63] F.A. Riddiford, A. Tourqui, C.D. Bishop, B. Taylor, and M. Smith. A cleaner development: The In Salah Gas Project, Algeria. In *The 6th International Conference on Greenhouse Gas Control Technologies (GHGT-6), Kyoto, Japan*, pages 601–606, 2003.

[64] C. Preston, M. Monea, W. Jazrawi, K. Brown, S. Whittaker, D. White, D. Law, R. Chalaturnyk, and B. Rostron. IEA GHG Weyburn CO2 monitoring and storage project. *Fuel Processing Technology*, 86(14-15):1547–1568, October 2005.

[65] R.A. Chadwick, D. Noy, E. Lindeberg, R. Arts, O. Eiken, and G. Williams. Calibrating reservoir performance with time-lapse seismic monitoring and flow simulations of the Sleipner CO2 plume. In *Proceedings of the 8th International Conference on Greenhouse Gas Control Technologies, Trondheim, Norway, 19-22June.* Elsevier, 2006.

[66] E. Lindeberg and P. Bergmo. The long-term fate of CO2 injected into an aquifer. Proceedings of the 6th International Conference on Greenhouse Gas Control Technologies (GHGT-6). pages 489–494, 2003.

[67] I. Gaus, M. Azaroual, and I. Czernichowski-Lauriol. Reactive transport modelling of the impact of CO2 injection on the clayey cap rock at Sleipner (North Sea). *Chemical Geology*, 217(3-4):319–337, April 2005.

[68] M. Bickle, A. Chadwick, H.E. Huppert, M. Hallworth, and S. Lyle. Modelling carbon dioxide accumulation at Sleipner: Implications for underground carbon storage. *Earth and Planetary Science Letters*, 255(1-2):164–176, March 2007.

[69] B. Rostron and S. Whittaker. 10+ years of the IEA-GHG Weyburn-Midale CO2 monitoring and storage project: Successes and lessons learned from multiple hydrogeological investigations. *Energy Procedia*, 4(July 2000):3636–3643, January 2011.

[70] M. Wilson and M. Monea. IEA GHG Weyburn Monitoring and Storage Project, Summary Report, 2000-2004. In *Proceedings of the 7th International Conference on Greenhouse Gas Control Technologies (GHGT-7), September 5-9*, 2005.

[71] P.S. Ringrose, a.S. Mathieson, I.W. Wright, F. Selama, O. Hansen, R. Bissell, N. Saoula, and J. Midgley. The In Salah CO2 Storage Project: Lessons Learned and Knowledge Transfer. *Energy Procedia*, 37:6226–6236, 2013.

[72] A. Cavanagh and P. Ringrose. Simulation of CO2 distribution at the In Salah storage site using high-resolution field-scale models. *Energy Procedia*, 4:3730–3737, January 2011.

[73] S. Bachu and B. Bennion. Effects of in-situ conditions on relative permeability

characteristics of CO2-brine systems. *Environmental Geology*, 54(8):1707–1722, July 2007.

[74] L. Zuo, S. Krevor, R.W. Falta, and S.M. Benson. An Experimental Study of CO2 Exsolution and Relative Permeability Measurements During CO2 Saturated Water Depressurization. *Transport in Porous Media*, 91(2):459–478, September 2011.

[75] C.H. Pentland, R. El-Maghraby, S. Iglauer, and M.J. Blunt. Measurements of the capillary trapping of super-critical carbon dioxide in Berea sandstone. *Geophysical Research Letters*, 38(6):L06401, March 2011.

[76] R. Pini, S.C.M. Krevor, and S.M. Benson. Capillary pressure and heterogeneity for the CO2/water system in sandstone rocks at reservoir conditions. *Advances in Water Resources*, 38:48–59, March 2012.

[77] J.C. Perrin and S. Benson. An Experimental Study on the Influence of Sub-Core Scale Heterogeneities on CO2 Distribution in Reservoir Rocks. *Transport in Porous Media*, 82(1):93–109, June 2009.

[78] S. Someya, S. Bando, Y. Song, B. Chen, and M. Nishio. Laser-Dye Imaging of the pH Field in a Laboratory Experiment. *Journal of Oceanography*, 60:789–795, 2004.

[79] S. Someya, S. Bando, B. Chen, Y. Song, and M. Nishio. Measurement of CO2 solubility in pure water and the pressure effect on it in the presence of clathrate hydrate. *International Journal of Heat and Mass Transfer*, 48(12):2503–2507, June 2005.

[80] Y. Song, B. Chen, M. Nishio, and M. Akai. The study on density change of carbon dioxide seawater solution at high pressure and low temperature. *Energy*, 30(11-12):2298–2307, August 2005.

[81] D.N. Espinoza and J.C. Santamarina. Water-CO2 mineral system: Interfacial tension, contact angle and diffusion-Implication to CO2 geological storage. *Water Resources Research*, 46(W07537):1–10, 2010.

[82] C. Chalbaud, M. Robin, J-M Lombard, F. Martin, P. Egermann, and H. Bertin. Interfacial tension measurements and wettability evaluation for geological CO2 storage. *Advances in Water Resources*, 32(1):98–109, January 2009.

[83] S.C.M. Krevor, R. Pini, L. Zuo, and S.M. Benson. Relative permeability and

trapping of CO2 and water in sandstone rocks at reservoir conditions. *Water Resources Research*, 48(2):1–16, February 2012.

[84] C. Doughty and K. Pruess. Modeling supercritical CO2 injection in heterogeneous porous media. In *Proceeding TOUGH symposium*, 2003.

[85] M. Flett, R. Gurton, and I. Taggart. The function of gas-water relative permeability hysteresis in the sequestration of carbon dioxide in saline formation. In *in SPE Asia Pacific Oil and Gas Conference, SPE 88485*, pages 1–11, 2004.

[86] Wikipedia. Capillary pressure, 2013.

[87] Wikipedia. Relative Permeability, 2013.

[88] C.P. Green and J. Ennis-King. Effect of Vertical Heterogeneity on Long-Term Migration of CO2 in Saline Formations. *Transport in Porous Media*, 82(1):31–47, November 2009.

[89] U.C. Bandara, A.M. Tartakovsky, and B.J. Palmer. Pore-scale study of capillary trapping mechanism during CO2 injection in geological formations. *International Journal of Greenhouse Gas Control*, 5(6):1566–1577, November 2011.

[90] R.S. Middleton and J.M. Bielicki. A scalable infrastructure model for carbon capture and storage: SimCCS. *Energy Policy*, 37(3):1052–1060, March 2009.

[91] D.J. Roddy. Development of a CO2 network for industrial emission. *Applied energy*, 91(1):459–465, 2012.

[92] R.A. Esposito, L.S. Monroe, and J.S. Friedman. Deployment models for commercialized carbon capture and storage. *Environmental science & technology*, 45:139–146, 2011.

[93] D. Savage, P.R. Maul, S. Benbow, and R.C. Walke. A generic FEP database for the assessment of long-term performance and safety of the geological storage of CO2. *Quintessa Report QRS-1060A-1*, page 73, 2004.

[94] W.R. Rish. A probabilistic risk assessment of Class 1 hazardous waste injection sites. *Underground Injection Science and Technology*, 52:93–125, 2005.

[95] P.H. Stauffer, H.S. Viswanathan, G.D. Guthrie, R.J. Pawar, J.P. Kaszuba, W. Carey, P.C. Lichtner, H.J. Ziock, M.K. Dubey, S.C. Olsen, and S.J. Chipera. CO2-PENS:A CO2 sequestration systems model supporting risk-based decision. In

Proceedings of the 16th International Conference on Computational Methods in Water Resources, Copenhagen, Denmark, June 19-22, 2006.

[96] C.M. Oldenburg, S.L. Bryant, and J.-P. Nicot. Certification framework based on effective trapping for geologic carbon sequestration. *International Journal of Greenhouse Gas Control*, 3(4):444–457, July 2009.

[97] H.S. Viswanathan, R.J. Pawar, P.H. Stauffer, J.P. Kaszuba, J.W. Carey, S.C. Olsen, G.N. Keating, D. Kavetski, and G.D. Guthrie. Development of a Hybrid Process and System Model for the Assessment of Wellbore Leakage at a Geologic CO 2 Sequestration Site. *Environmental Science & Technology*, 42(19):7280–7286, October 2008.

[98] J.M. Nordbotten, M.A. Celia, and S. Bachu. Injection and storage of CO2 in deep saline aquifers: Analytical solution for CO2 plume evolution during injection. *Transport Porous Med.*, 58:339–360, 2005.

[99] N. Kumar, S. Bryant, and J.-P. Nicot. Simplified CO2 plume dynamics for a Certification Framework for geologic sequestration projects. *Energy Procedia*, 1(1):2549–2556, February 2009.

[100] UPC. CODE-BRIGHT, a 3D program for thermo-hydro-mechanical analysis in geological media, user's guide. Technical report, 2002.

[101] M.G. Trefry and C. Muffels. FEFLOW: a finite-element ground water flow and transport modelling tool. *Ground water*, 45(5):525–528, 2007.

[102] B.A. Robinson, H.S. Viswanathan, and A.J. Valocchi. Efficient numerical techniques for modeling multicomponent ground-water transport based upon simultaneous solution of strongly coupled subsets of chemical components. *Advances in Water Resources*, 23:307–324, 2000.

[103] J. Wheeler. IPARS User's Manual. *The University of Texas at Austin, Texas*, 1995.

[104] H. Class, A. Ebigbo, R. Helmig, H.K. Dahle, J.M. Nordbotten, M.A. Celia, Pascal. Audigane, M. Darcis, J. Ennis-King, Y. Fan, B. Flemisch, S.E. Gasda, M. Jin, S. Krug, D. Labregere, A. Naderi Beni, R.J. Pawar, A. Sbai, S.G. Thomas, L. Trenty, and L. Wei. A benchmark study on problems related to CO2 storage in geologic formations. *Computational Geosciences*, 13(4):409–434, July 2009.

[105] C.I. Voss. A finite-element simulation model for saturated-unsaturated, fluid-

density-dependent ground water flow with energy transport or chemically-reactive single-species solute transport. *US Geological Survey Water Resources Investigations Report WRI-84-4369*, 1984.

[106] Schlumberger. ECLIPSE 2012 Reservoir Engineering Software. Technical report, 2012.

[107] M.G. McDonald and A.W. Harbaugh. The history of MODFLOW. *Ground water*, 41(2):280–283, 2003.

[108] D.L. Parkhurst, K.L. Kipp, and S.R. Charlton. PHAST Version 2-a program for simulating groundwater flow, solute tranport, and multicomponent geochemical reaction. *US Geological Survey Techniques and Methods 6-A35*, 2010.

[109] C.I. Voss. A finite-element simulation model for saturated-unsaturated, fluid-density-dependent ground water flow with energy transport or chemically reactive single-species solute transport. *US Geological Survey Water Resources Investigations Report WRI-84-4369*, 1984.

[110] K. Pruess, C. Oldenburg, and G. Moridis. Tough2 user's guide, version2.0. (November), 1999.

[111] B. Flemisch, J. Fritz, R. Helmig, J. Niessner, and B. Wohlmuth. DuMux: a multi-scale multi-physics toolbox for flow and transport processes in porous media. In *ECCOMAS thematic conference on multi-scale computational methods for solid and fluids, Cachan, France*, 2007.

[112] K.U. Mayer and K.T.B. MacQuarrie. Solution of the MoMas reactive transport benchmark with MIN3P-model formulation and simulation results. *Comput Geosci*, 14:405–419, 2010.

[113] C. Zheng, J. Weaver, and M. Tonkin. MT3DMS, A modular three-dimensional multispecies transport model-user guide to the hydrocarbon spill source Package. *US Environmental Protection Agency, Athens, Georgia*, 2010.

[114] H. Class, R. Helmig, and P. Bastian. Numerical simulation of non-isothermal multiphase multicomponent processes in porous media, An efficient solution technique. *Advances in Water Resources*, 25(5):533–550, 2002.

[115] A.L. Edwards. TRUMP: A computer program for transient and steady state tem-

perature distribution in multidimensional systems. *National Bureau of Standards, Springfield, VA*, 1972.

[116] T. N. Narasimhan and P. A. Witherspoon. An integrated finite difference method for analyzing fluid flow in porous media. *Water Resources Research*, 12(1):57–64, 1976.

[117] T.J. Kneafsey and K. Pruess. Laboratory Flow Experiments for Visualizing Carbon Dioxide-Induced, Density-Driven Brine Convection. *Transport in Porous Media*, 82(1):123–139, October 2009.

[118] J. Oh, K.-Y. Kim, W.S. Han, T. Kim, J.-C. Kim, and E. Park. Experimental and numerical study on supercritical CO2/brine transport in a fractured rock: Implications of mass transfer, capillary pressure and storage capacity. *Advances in Water Resources*, pages 1–12, April 2013.

[119] J. Birkholzer, Q. Zhou, and C. Tsang. Large-scale impact of CO2 storage in deep saline aquifers: A sensitivity study on pressure response in stratified systems. *International Journal of Greenhouse Gas Control*, 3(2):181–194, March 2009.

[120] R.P. Batycky, M.J. Blunt, and M.R. Thiele. A 3D field-scale streamline-based reservoir simulator. *SPE Reservoir Engineering*, 12(4):246–254, 1997.

[121] R. Qi, T.C. LaForce, and M.J. Blunt. A three-phase four-component streamline-based simulator to study carbon dioxide storage. *Computational Geosciences*, 13(4):493–509, May 2009.

[122] D.W. Pollock. Semi-analytical computation of pathlines for finite-difference models. *Groundwater*, 26(b):743–750, 1998.

[123] G.S. Bromhal. Pore-Level Modeling of Carbon Dioxide Sequestration in Oil Fields : A study of viscous and buoyancy forces. In *In: Proceedings of 1st National Conference on*, pages 1–7, 2001.

[124] Q. Kang, P.C. Lichtner, and D. Zhang. An improved lattice Boltzmann model for multicomponent reactive transport in porous media at the pore scale. *Water Resources Research*, 43(12):1–12, November 2007.

[125] Q. Kang, D. Zhang, S. Chen, and X. He. Lattice Boltzmann simulation of chemical dissolution in porous media. *Physical Review E*, 65(3), March 2002.

[126] O. Lopez, N. Idowu, Al. Mock, H. Rueslatten, and T. Boassen. Pore-scale

modelling of CO2-brine flow properties at In Salah, Algeria. *Energy Procedia*, 2010.

[127] C. Chen and D. Zhang. Pore-scale simulation of density-driven convection in fractured porous media during geological CO 2 sequestration. *Water Resources Research*, pages 1–24, 2010.

[128] A. Raoof and S.M. Hassanizadeh. Saturation-dependent solute dispersivity in porous media: Pore-scale processes. *Water Resources Research*, 49(4):1943–1951, April 2013.

[129] L. Chen, Qi. Kang, B.A. Robinson, Y.L. He, and W.Q. Tao. Pore-scale modeling of multiphase reactive transport with phase transitions and dissolution-precipitation processes in closed systems. *Physical Review E*, 87(4):043306, April 2013.

[130] M. Blunt and P. King. Relative Permeabilities from Two- and Three-Dimensional Pore-Scale Network Modelling. *Transport in Porous Media*, 6:407–433, 1991.

[131] Q. Kang, D. Zhang, and S. Chen. Immiscible displacement in a channel: simulations of fingering in two dimensions. *Advances in Water Resources*, 27(1):13–22, January 2004.

[132] Q. Kang and D. Zhang. Simulation of dissolution and precipitation in porous media. *Journal of geophysical research*, 108:1–10, 2003.

[133] C. Huber, B. Shafei, and A. Parmigiani. A new pore-scale model for linear and non-linear heterogeneous dissolution, precipitation and sorption reactions. *Geochimica et Cosmochimica Acta*, September 2013.

[134] H. Ovdat and B. Berkowitz. Pore-scale study of drainage displacement under combined capillary and gravity effects in index-matched porous media. *Water Resources Research*, 42(6):W06411, 2006.

[135] S.E. Gasda, J.M. Nordbotten, and M.A. Celia. The impact of local-scale processes on large-scale CO2 migration and immobilization. In *XVIII International Conference on Water Resources*, pages 1–8, 2010.

[136] M. Al-Gharbi and M. Blunt. Dynamic network modeling of two-phase drainage in porous media. *Physical Review E*, 71(1):016308, January 2005.

[137] S.C. Borjia. *Lattice Boltzmann Modeling for mass transport equations in porous media.* PhD thesis, 2008.

[138] J. Tölke, M. Krafczyk, M. Schulz, and E. Rank. Lattice Boltzmann simulations of binary fluid flow through porous media. *Philosophical transactions. Series A, Mathematical, physical, and engineering sciences*, 360(1792):535–45, March 2002.

[139] A.K. Gunstensen. *Lattice-Boltzmann studies of multiphase flow through porous media*. PhD thesis, MIT, 1992.

[140] A.M. Tartakovsky and P. Meakin. Pore scale modeling of immiscible and miscible fluid flows using smoothed particle hydrodynamics. *Advances in Water Resources*, 29(10):1464–1478, October 2006.

[141] A.Q. Raeini, M.J. Blunt, and B. Bijeljic. Modelling two-phase flow in porous media at the pore scale using the volume-of-fluid method. *Journal of Computational Physics*, 231(17):5653–5668, July 2012.

[142] P. Meakin and A.M. Tartakovsky. Modeling and simulation of pore-scale multiphase fluid flow and reactive transport in fractured and porous media. *Review of Geophysics*, 47:2008RG000263(1–47), 2009.

[143] Y. H. Qian, D. D'Humières, and P. Lallemand. Lattice BGK Models for Navier-Stokes Equation. *Europhysics Letters (EPL)*, 17(6):479–484, February 1992.

[144] S. Chen and G. D. Doolen. Lattice Boltzmann method for fluid flows. *Annu. Rev. Fluid Mech*, 30:329–64, July 1998.

[145] B. He, W. Feng, W. Zhang, and Y. Cheng. Parallel Simulation of Compressible Fluid Dynamics Using Lattice Boltzmann Method. *The first International Symposium on Optimization and Systems Biology*, pages 451–458, 2007.

[146] X. He, S. Chen, and R. Zhang. A Lattice Boltzmann Scheme for Incompressible Multiphase Flow and Its Application in Simulation of Rayleigh-Taylor Instability. *Journal of Computational Physics*, 152:642–663, 1999.

[147] X. Shan and H. Chen. Lattice Boltzmann model for simulating flows with multiple phases and components. *Physical Review E*, 47(3):1815–1819, 1993.

[148] A. Joshi and Y. Sun. Wetting dynamics and particle deposition for an evaporating colloidal drop: A lattice Boltzmann study. *Physical Review E*, 82(4):1–17, October 2010.

[149] M. Yoshino and T. Inamuro. Lattice Boltzmann simulations for flow and heat/mass

transfer problems in a three-dimensional porous structure. *International Journal for Numerical Methods in Fluids*, 198(May):183–198, 2003.

[150] K. Langaas and P. Papatzacos. Numerical Investigations of the Steady State Relative Permeability of a Simplified Porous Medium. *Transport in Porous Media*, 45:241–266, 2001.

[151] F. J. Higuera and J. Jimenez. Boltzmann Approach to Lattice Gas Simulations. *Europhysics Letters (EPL)*, 9(7):663–668, August 1989.

[152] J. Hardy, O. de Pazzis, and Y. Pomeau. Molecular dynamics of a classical lattice gas: Transport properties and time correlation functions. *Physical Review A*, 13:1949–1960, 1976.

[153] D.H. Rothman. Modeling seismic P-waves with cellular automatia. *Geophysical Research Letters*, 14:17–20, 1987.

[154] D.A. Wolf-Gladrow. *Lattice-Gas Cellular Automata and Lattice Boltzmann Models - An Introduction.* Springer, 2005.

[155] U. Frisch, B. Hasslacher, and Y. Pomeau. Lattice-Gas Automata for the Navier-Stokes Equation. *Physical Review Letters*, 56(14):1505–1508, 1986.

[156] U. Frisch, D. D'Humieres, B. Hasslacher, P. Lallemand, Y. Pomeau, and J.P. Rivet. Lattice gas hydrodynamics in two and three dimensions. *Complex Systems*, 1:648, 1987.

[157] D. D'Humieres, P. Lallemand, and G. Searby. Numerical experiments on lattice gases: Mixtures and galilean invariance. *Complex Systems*, 1:633–647, 1987.

[158] C. Burges and S. Zaleski. Buoyant mixtures of cellular automaton gases. *Complex Systems*, 1:31, 1987.

[159] D. Dab, A. Lawniczak, J. Boon, and R. Kapral. Cellular automation model for reactive systems. *Phys. Rev. Lett.*, 64:2462–2465, 1990.

[160] D.H. Rothman and J.M. Keller. Immiscible Cellular-Automaton Fluids. *Journal of Statistical Physics*, 52(3/4):1119–1127, 1988.

[161] J. Zhang. Lattice Boltzmann method for microfluidics: models and applications. *Microfluidics and Nanofluidics*, 10(1):1–28, April 2010.

[162] G.R. McNamara and G. Zanetti. Use of the Boltzmann equation to simulate lattice-gas automata. *Phys. Rev. Lett.*, 61:2332–2335, 1988.

[163] X. He and L. Luo. Theory of the lattice Boltzmann method: From the Boltzmann equation to the lattice Boltzmann equation. *Physical Review E*, 56(6):6811–6817, December 1997.

[164] P. L. Bhatnagar, E. P. Gross, and M. Krook. A Model for Processes in Gases. I. Small Amplitude Processes in Charged and Neutral One-Component System. *Physical Review*, 94(3):511–525, 1954.

[165] L. Jonas. *Hydrodynamic Limit of Lattice Boltzmann Equations.* PhD thesis, 2007.

[166] A.K. Gunstensen and D.H. Rothman. Lattice Boltzmann model of immiscible fluids. *Physical Review A*, 43(8):4320–4327, 1991.

[167] N.S. Martys and H. Chen. Simulation of multicomponent fluids in complex three-dimensional geometries by the lattice Boltzmann method. *Physical Review E*, 53(1):743–750, 1996.

[168] N. Martys, J. Hagedorn, D. Goujon, and J. Devaney. Large Scale simulations of Single and Multi-Component Flow in Porous Media. *Pro. SPIE*, 3772:205–213, 1999.

[169] M.M. Dupin, I. Halliday, and C.M. Care. A multi-component lattice Boltzmann scheme: towards the mesoscale simulation of blood flow. *Medical engineering & physics*, 28(1):13–8, January 2006.

[170] M.R. Swift, W.R. Osborn, and J.M. Yeomans. Lattice Boltzmann simulation of nonideal fluids. *Physical Review Letters*, 75(5):830–833, 1995.

[171] M.R. Swift, E. Orlandini, W.R. Osborn, and J.M. Yeomans. Lattice Boltzmann simulations of liquid-gas and binary fluid systems. *Physical Review E*, 54(5):5041–5052, 1996.

[172] X. He and G.D. Doolen. Thermodynamic Foundations of Kinetic Theory and Lattice Boltzmann Models for Multiphase Flows. *Journal of Statistical Physics*, 107(April):309–328, 2002.

[173] R.R. Nourgaliev, T.N. Dinh, T.G. Theofanous, and D. Joseph. The lattice Boltzmann equation method: theoretical interpretation, numerics and implications. *International Journal of Multiphase Flow*, 29(1):117–169, January 2003.

[174] N. Takada, M. Misawa, A. Tomiyama, and S. Hosokawa. Simulation of Bubble

Motion under Gravity by Lattice Boltzmann Method. *Journal of Nuclear Science and Technoliogy*, 38(5):330–341, 2001.

[175] X. He, X. Shan, and G. Doolen. Discrete Boltzmann equation model for nonideal gases. *Physical Review E*, 57(1):R13–R16, January 1998.

[176] Y.H. Qian, S. Succi, and S.A. Orszag. Recent advances in Lattice Boltzmann computing. In *Ann. Rev. Comp. Phys.*, pages 195–242. 1995.

[177] D.J. van der Waales. *On the continuity of the gaseous and liquid states.* Universiteit Leiden, 1873.

[178] O. Redlich and J.N.S. Kwong. On the thermodynamics of solution. V An equastion of state. Fugacities of gaseous solution. *Chemical Reviews*, 44(1):233–244, 1949.

[179] D.M. Kerrick and G.K. Jacobs. A modified Redlich-Kwong equation for H2O, CO2 and H2O-CO2 mixtures at elevated pressures and temperatures. *American Journal of Science*, 281:735–767, 1981.

[180] F.H. Huang, M.H. Li, L.L. Lee, K.E. Starling, and F.T.H. Chung. An accurate equation of state for carbon dioxide. *Journal of Chemical Engineering of Japan*, 18(6):490–495, 1985.

[181] Z. Duan, N. Moller, and J.H. Weare. An equation of state for the CH4-CO2-H2O system: I. Pure systems from 0 to 1000C and 0 to 8000 bar. *Geochimica et Cosmochimica Acta*, 56:2605–2617, 1992.

[182] Z. Duan and Z. Zhang. Equation of state of the H2O, CO2, and H2O-CO2 systems up to 10 GPa and 2573.15K: Molecular dynamics simulations with ab initio potential surface. *Geochimica et Cosmochimica Acta*, 70(9):2311–2324, May 2006.

[183] D. Peng and D.B. Robinson. A New Two-Constant Equation of State. *Industrial & Engineering Chemistry Fundamentals*, 15(1):59–64, February 1976.

[184] R. Span and W. Wagner. A new Equation of State for Carbon Dioxide Covering the Fluid Region from the Triple-Point Temperature to 1100K at PRessure up to 800MPa. *Journal Phys. Chem.*, 25(6):1509–1596, 1996.

[185] P. Yuan and L. Schaefer. Equations of state in a lattice Boltzmann model. *Physics of Fluids*, 18(4):042101, 2006.

[186] A. Gupta and R. Kumar. Lattice Boltzmann simulation to study multiple bubble

dynamics. *International Journal of Heat and Mass Transfer*, 51(21-22):5192–5203, October 2008.

[187] D.P. Ziegler. Boundary condition for Lattice Boltzmann simulations. *Journal of Statistical Physics*, 71(5/6):1171–1177, 1993.

[188] P.A. Skordos. Initial and boundary conditions for the lattice Boltzmann method. *Physical Review E*, 48(6):4823–4842, 1993.

[189] T. Inamuro, M. Yoshino, and F. Ogino. A non-slip boundary condition for lattice Boltzmann simulations. *Physcis of Fluids*, 7:2928, 1995.

[190] I. Ginzbourg and D. D'Humieres. Local second-order boundary methods for lattice Boltzmann models. *Journal of Statistical Physics*, 84(5-6):927–971, 1996.

[191] R.S. Maier, R.S. Bernard, and D.W. Grunau. Boundary conditions for the lattice Boltzmann method. *Physcis of Fluids*, 8(7):1788–1801, December 1996.

[192] Q. Zou and X. He. On pressure and velocity boundary conditions for the lattice Boltzmann BGK model. *Physics of Fluids*, 9(6):1591, 1997.

[193] X. Zhang, J.W. Crawford, A.G. Bengough, and I.M. Young. On boundary conditions in the lattice Boltzmann model for advection and anisotropic dispersion equation. *Advances in Water Resources*, 25(6):601–609, June 2002.

[194] J. Latt and B. Chopard. Straight velocity boundaries in the lattice Boltzmann method. 2008.

[195] X. He, Q. Zou, L.S. Luo, and M. Dembo. Analytic Solutions of Simple Flows and Analysis of Nonslip Boundary Conditions for the Lattice Boltzmann BGK Model. *Journal of Statistical Physics*, 87:115–136, 1997.

[196] M.C. Sukop and D. Or. Lattice Boltzmann method for modeling liquid-vapor interface configurations in porous media. *Water Resources Research*, 40(1):W01509, January 2004.

[197] S. Hou, Q. Zou, S. Chen, G.D. Doolen, and A.C. Cogley. Simulation of Cavity Flow by the lattice Boltzmann method. pages 1–46, 1994.

[198] D.R. Noble, J.G. Georgiadis, and R. Buckius. A consistent hydrodynamic boundary condition for the latticeBoltzmann method. *Physcis of Fluids*, 7(1):203–209, 1995.

[199] I. Ginzbourg and P.M. Adler. Boundary flow condition analysis for the three-

dimensional lattice Boltzmann model. *Journal Phys. II France*, 4(2):191–214, 1994.

[200] Q. Zou and X. He. On pressure and velocity flow boundary conditions and bounceback for the lattice Boltzmann BGK model. pages 1–19, 1996.

[201] A.S. Joshi, A.A. Peracchio, K.N. Grew, and W.K.S. Chiu. Lattice Boltzmann method for continuum, multi-component mass diffusion in complex 2D geometries. *Journal of Physics D: Applied Physics*, 40(9):2961–2971, May 2007.

[202] H. Yu and K. Zhao. Lattice boltzmann method for compressible flows with high mach numbers. *Physical review. E, Statistical physics, plasmas, fluids, and related interdisciplinary topics*, 61(4 Pt A):3867–70, April 2000.

[203] M. Mehravaran and S.K. Hannani. Simulation of incompressible two-phase flows with large density differences employing lattice Boltzmann and level set methods. *Computer Methods in Applied Mechanics and Engineering*, 198(2):223–233, December 2008.

[204] F. Chen, A. Xu, G. Zhang, Y. Li, and S. Succi. Multiple-Relaxation-Time Lattice Boltzmann Approach to Compressible Flows with Flexible Specific-Heat Ratio and Prandtl Number. *Applied Physics*, pages 1–7, 2010.

[205] J.D. Sterling and S. Chen. Stability Analysis of Lattice Boltzmann Methods. *Journal of Computational Physics*, (123):196–206, 1996.

[206] K. Sankaranarayanan, X. Shan, I. G. Kevrekidis, and S. Sundaresan. Analysis of drag and virtual mass forces in bubbly suspensions using an implicit formulation of the lattice Boltzmann method. *Journal of Fluid Mechanics*, 452:61–96, February 2002.

[207] X. Shan. Analysis and reduction of the spurious current in a class of multiphase lattice Boltzmann models. *Physical Review E*, 73(4):6–9, April 2006.

[208] M. Sbragaglia, R. Benzi, L. Biferale, S. Succi, K. Sugiyama, and F. Toschi. Generalized lattice Boltzmann method with multirange pseudopotential. *Physical Review E*, 75(2):1–13, February 2007.

[209] E.S. Oran and J.P. Boris. *Numerical Simulation of Reactive Flow. Second Edition*, volume 12. The press syndicate of the University of Cambridge, November 1987.

[210] K. Sankaranarayanan, X. Shan, I. G. Kevrekidis, and S. Sundaresan. Analysis of

drag and virtual mass forces in bubbly suspensions using an implicit formulation of the lattice Boltzmann method. *Journal of Fluid Mechanics*, 452:61–96, February 2002.

[211] J. Latt. Choice of units in lattice Boltzmann simulations. *LBMthod.org*, pages 1–6, 2008.

[212] R. Holme and D.H. Rothman. Lattice-Gas and Lattice Botlzmann Models of Miscible Fluids. *Journal of Statistical Physics*, 68(3/4):409–430, 1992.

[213] E.G. Flekkoy. Lattice Bhatnagar-Gross-Krook models for miscible fluids. *Physical Review E*, 47(6):4247–4257, 1993.

[214] D.R. Noble. *Lattice Boltzmann study of the interstitial hydrodynamics and dispersion in steady inertial flows in large randomly packed beds.* PhD thesis, 1997.

[215] C.E. Knutson, C.J. Werth, and A.J. Valocchi. Pore-scale modeling of dissolution from variably distributed nonaqueous phase liquid blobs. *Water Resources Research*, 37(12):2951–2963, 2001.

[216] T. Inamuro, M. Yoshino, H. Inoue, R. Mizuno, and F. Ogino. A Lattice Boltzmann Method for a Binary Miscible Fluid Mixture and Its Application to a Heat-Transfer Problem. *Journal of Computational Physics*, 179(1):201–215, June 2002.

[217] R.M.H. Merks, A.G. Hoekstra, and P.M.A. Sloot. The Moment Propagation Method for Advection-Diffusion in the Lattice Boltzmann Method: Validation and Péclet Number Limits. *Journal of Computational Physics*, 183(2):563–576, December 2002.

[218] X. Zhang, A.G. Bengough, J.W. Crawford, and I.M. Young. A lattice BGK model for advection and anisotropic dispersion equation. *Advances in Water Resources*, 25(1):1–8, January 2002.

[219] Q. Kang, D. Zhang, and S. Chen. Displacement of a two-dimensional immiscible droplet in a channel. *Physics of Fluids*, 14(9):3203, 2002.

[220] R.D. Kingdon and P. Schofield. A reaction-flow lattice Boltzmann model. *J. Phys. A: Math. Gen.*, 25:907–910, 1992.

[221] J.R. Weimar and J.P. Boon. Nonlinear reactions advected by a flow. *Physica A: Statistical Mechanics and its Applications*, 224(1-2):207–215, 1996.

[222] S.P. Dawson, S. Chen, and G.D. Doolen. Lattice Boltzmann computations for reaction-diffusion equations. *J. Chem. Phys.*, 98(2):1514–1523, 1993.

[223] Y.H. Qian and S.A. Orszag. Scalings in diffusion-driven reaction A+B C: Numerical simulations by lattice BGK models. *Journal of Statistical Physics*, 81(1-2):237–253, 1995.

[224] J.T. Wellsa, D.R. Janeckyb, and B.J. Travisc. A lattice gas automata model for heterogeneous chemical reactions at mineral surfaces and in pore networks. *Physica D: Nonlinear Phenomena*, 41(1-2):115–123, 1991.

[225] X. He, N. Li, and B. Goldstein. Lattice Boltzmann Simulation of Diffusion-Convection Systems with Surface Chemical Reaction. *Molecular Simulation*, 25(3-4):145–156, August 2000.

[226] Q. Kang, P.C. Lichtner, and D. Zhang. Lattice Boltzmann pore-scale model for multicomponent reactive transport in porous media. *Journal of Geophysical Research*, 111(B5):B05203, 2006.

[227] S.P. Sullivan, F.M. Sani, M.L. Johns, and L.F. Gladden. Simulation of packed bed reactors using lattice Boltzmann methods. *Chemical Engineering Science*, 60(12):3405–3418, June 2005.

[228] X. Shan and G. Doolen. Diffusion in a multicomponent lattice Boltzmann equation model. *Physical review. E, Statistical physics, plasmas, fluids, and related interdisciplinary topics*, 54(4):3614–3620, October 1996.

[229] J. Crank. *The mathematics of diffusion Second Edition.* 1975.

[230] B.E. Poling and J.M. Prausnitz. *THE properties of gases and liquids Fifth Edition.* The MacGraw-Hill Companies, Inc., 2001.

[231] D.F. McGinnis, M. Schmidt, T. DelSontro, S. Themann, L. Rovelli, A. Reitz, and P. Linke. Discovery of a natural CO 2 seep in the German North Sea: Implications for shallow dissolved gas and seep detection. *Journal of Geophysical Research*, 116(C3):1–12, March 2011.

[232] J.C. Blackford, N. Jones, R. Proctor, and J. Holt. Regional scale impacts of distinct CO2 additions in the North Sea. *Marine pollution bulletin*, 56(8):1461–8, August 2008.

[233] K.J. Kroeker, F. Micheli, M.C. Gambi, and T.R. Martz. Divergent ecosystem

responses within a benthic marine community to ocean acidification. *Proceedings of the National Academy of Sciences of the United States of America*, 108(35):14515–20, August 2011.

[234] B. Laverock, C.J. Smith, K. Tait, A.M. Osborn, S. Widdicombe, and J.A. Gilbert. Bioturbating shrimp alter the structure and diversity of bacterial communities in coastal marine sediments. *The ISME journal*, 4(12):1531–1544, December 2010.

[235] R. Rodolfo-Metalpa, F. Houlbrèque, É. Tambutté, F. Boisson, C. Baggini, F. P. Patti, R. Jeffree, M. Fine, A. Foggo, J-P. Gattuso, and J. M. Hall-Spencer. Coral and mollusc resistance to ocean acidification adversely affected by warming. *Nature Climate Change*, 1(6):308–312, August 2011.

[236] S. Widdicombe and J. Spicer. Predicting the impact of ocean acidification on benthic biodiversity: What can animal physiology tell us? *Journal of Experimental Marine Biology and Ecology*, 366(1-2):187–197, November 2008.

[237] C. Manes, D. Pokrajac, I. McEwan, and V. Nikora. Turbulence structure of open channel flows over permeable and impermeable beds: A comparative study. *Physics of Fluids*, 21(12):125109, 2009.